

DISS. ETH NO. 19116

# **Hybrid PDF Algorithm and PDF Modeling of Partially Premixed Turbulent Combustion**

A dissertation submitted to

ETH ZURICH

for the degree of

Doctor of Sciences

presented by

MICHAEL JAKOB HEGETSCHWEILER

Dipl. Masch.-Ing. ETH

Date of birth

May 25, 1974

citizen of

Ottenbach (ZH)

accepted on the recommendation of

Prof. Dr. Patrick Jenny

PD. Dr. Ioannis Mantzaras

2010



## Abstract

Turbulent combustion has been for a long time and is until nowadays a very active and interesting field of research. It can be subdivided into three major parts, the discovery and investigation of physical combustion and turbulent flow phenomena and their interactions, the search for mathematical descriptions of those effects and finally, the development of computer algorithms to simulate turbulent reactive flows. Discovering and understanding of new physical combustion phenomena is mainly achieved by experiments, but also more and more by direct numerical simulation (DNS). Since such real and numerical experiments are expensive and time consuming, it is crucial to derive physical models, which then are applied in so called lower closure level computer codes in order to compute real world configurations. There exist different modeling approaches based on the Reynolds averaged Navier Stokes (RANS) equation. Common representatives of such approaches are two equation turbulent viscosity models, e.g.  $k$ - $\epsilon$ - or  $k$ - $\omega$ -models, or Reynolds stress models. Most of them are based on second moment evolution equations and therefore only limited flow information is available. A more sophisticated approach are the joint probability density function (PDF) methods, where a transport equation for the joint PDF of different flow and thermodynamic quantities is solved; consequently the whole statistical information of those quantities is available. Furthermore, turbulent convection and chemical source terms appear in closed form in the joint PDF framework.

In a first part of this work algorithmic issues of a so called hybrid finite volume-particle PDF solution method are addressed. A second part introduces and explains a new modeling approach for partially premixed combustion. In the hybrid approach, different consistency conditions between the finite volume and the particle part of the overall algorithm must be fulfilled. Here, a modified solution algorithm is presented, which ensures energy consistency by solving the energy equation only once.

The time integration of stochastic differential equations (SDE) is a central topic when solving PDF transport equations numerically with particle Monte Carlo methods. Therefore an adapted numerical integration scheme is presented based on Itô calculus, which honors the exact single and joint statistics of the particle position and velocities for arbitrary large time steps.

The newly developed model for partially premixed combustion is a combination and an extension of the flamelet approach, a molecular mixing model and a progress variable approach. The flamelet idea and a mixing model are combined to become a reactive mixing model, where particles evolve in mixture fraction-enthalpy space on representative, physically motivated profiles. The shape of the profiles is determined by the thermodynamic state of the particles and their environment. This thermodynamic state is triggered by a progress variable, similar to the Bray, Moss and Libby (BML) approach for premixed combustion.

Such a modeling framework can only be constructed in the context of PDF methods, since joint statistical information of mixture fraction, scalar dissipation rate and progress variable is required.

The model performance is analyzed by means of flames E and F of the Sandia National

## II

Laboratory. These flames exhibit all the important features found in partially premixed combustion and therefore are challenging test cases.



## Zusammenfassung

Die turbulente Verbrennung ist seit langer Zeit und bis heute ein sehr aktives und interessantes Forschungsgebiet. Es kann in drei Hauptgebiete unterteilt werden, der Entdeckung und Untersuchung von physikalischen Verbrennungs und turbulenten Strömungsphänomenen und deren Wechselwirkungen untereinander, das mathematische Beschreiben dieser Effekte und letztlich der Entwicklung von Computeralgorithmen um turbulente reaktive Strömungen zu simulieren. Das Entdecken und Verstehen von neuen physikalischen Vorgängen wird hauptsächlich durch Experimente aber auch mehr und mehr durch Direkte Numerische Simulation (DNS) erreicht. Diese realen und numerischen Experimente sind teuer und zeitintensiv, daher ist es wichtig für gewisse physikalische Effekte mathematische Modelle herzuleiten, die dann in Computercodes mit sogenanntem niedrigeren Schliessungsgrad eingesetzt werden können. Es existieren verschiedene Modellansätze die auf einer statistischen Beschreibung des Strömungsfeldes durch die Reynolds gemittelten Navier Stokes (RANS) Gleichungen basieren. Solche allgemein benutzte Ansätze sind Zweigleichungsmodelle wie zum Beispiel  $k-\epsilon$ - oder  $k-\omega$ -Modelle oder Reynoldsspannungsmodelle. Die Meisten von ihnen basieren auf Entwicklungsgleichungen für die zweiten statistischen Momente von Strömungsgrössen und deshalb ist nur eine limitierte Menge von Strömungsinformationen verfügbar. Eine raffinierterer Ansatz ist die Verbundwahrscheinlichkeitsdichtefunktion (Verbunds-WDF, engl. PDF) Methode bei der eine Transportgleichung für die Verbundwahrscheinlichkeit von verschiedenen strömungs- und thermodynamischen Grössen gelöst wird und somit die ganze statistische Information zur Verfügung steht. Ausserdem erscheinen im Rahmen der WDF Formulierung die turbulente Konvektion und der chemische Quellterm in geschlossener Form.

In dieser Arbeit wird in einem ersten Teil auf algorithmische Probleme eines sogenannten hybriden Finite Volumen - Partikel Lösungsverfahren eingegangen und in einem zweiten Teil wird ein neuer Modellansatz für partiell vorgemischte Verbrennung präsentiert.

In dem hybriden Lösungsverfahren müssen verschiedene Konsistenzbedingungen zwischen dem Finite Volumen- und dem Partikelteil des Codes erfüllt sein. Hier wird ein alternativer Lösungsalgorithmus entwickelt und beschrieben, der die Energiekonsistenz durch das Lösen nur einer Energiegleichung sicherstellt.

Die zeitliche Integration von stochastischen Differentialgleichungen (SDG) ist ein zentrales Thema beim numerischen Lösen von WDF Transportgleichungen mit Monte Carlo Partikel Methoden. Ein adaptiertes numerisches Integrationsschema basierend auf der Integralrechnung von Itô wird hergeleitet, welches die exakte Einzel- und Verbundsstatistik von Partikel Position und Geschwindigkeit für beliebig grosse Zeitschritte wiedergibt.

Das neue Modell für partiell vorgemischte Verbrennung ist eine Kombination und Erweiterung des Flamelet Ansatzes, eines molekularen Mischungsmodells und eines Fortschrittsvariablen Ansatzes. Die Flamelet Idee und ein Mischungsmodell werden zu einem reaktiven Mischungsmodell kombiniert, bei dem sich Partikel auf repräsentativen, physikalisch motivierten Profilen im Mischungsbruch - Enthalpy Raum entwickeln. Die Form der Profile wird durch den thermodynamischen Zustand der Partikel und ihrer Umgebung bestimmt. Getriggert wird dieser thermodynamische Zustand durch eine Fortschrittsvariable, ähnlich

dem Ansatz von Bray, Moss und Libby (BML) für vorgemischte Verbrennung.

Ein solches Verbrennungsmodell ist nur möglich im Kontext von WDF Methoden weil die Verbundstatistik von Mischungsbruch, skalarer Dissipationsrate und der Fortschrittsvariablen verfügbar sein muss.

Das Verhalten des Modells wird anhand von den Flammen E und F des Sandia National Laboratory analysiert. Diese Flammen weisen alle wichtigen Eigenschaften von partiell vorgemischter Verbrennung auf und sind daher anspruchsvolle Testfälle.

## Acknowledgments

I am especially grateful to Prof. Dr. Patrick Jenny, under whom this work was conducted. The lively discussions, the valuable advises and his encouragement and dedication for science were always a very important support and motivation for me. Our common passion for sports brings many good moments to my mind.

I would like to thank Dr. Ioannis Mantzaras for co-advising this thesis on rather short notice. Nevertheless he gave me a very valuable feedback.

Thanks goes to all my colleagues at the Institute of Fluid Dynamics at the ETH Zurich and especially to the members (or former members) of Prof. Jenny's group Dr. Daniel W. Meyer, Dr. Manav Tyagi, Dr. Benjamin Rembold, Michael Wild, Mathias Hack and Benjamin Zoller. There was always a good spirit and an inspiring atmosphere at the institute but also beyond the working place as for instance at the famous group hiking tours. Without the help of our secretaries Ms. Bianca Maspero and Ms. Sonia Atkinson and of the IT-support Mr. Hanspeter Caprez I would have been lost many times, thus best thanks to all of them for their kind support.

A very special thanks goes to my mother and my siblings. During rough and stressful times they provided a place of peace and recreation and were listening to all kind of problems.

This work was financially supported by the Swiss National Science Foundation (SNF) and the ETH Zurich.



for my mother and my late father



# Contents

<b>List of Figures</b>	<b>XII</b>
<b>Nomenclature</b>	<b>XV</b>
<b>1 Preface</b>	<b>1</b>
<b>I PDF Algorithm</b>	<b>5</b>
<b>2 Governing Equations of Fluid Motion and Thermo-Chemistry</b>	<b>7</b>
2.1 Fluid Motion Equations . . . . .	7
2.2 Thermo-Chemistry . . . . .	8
<b>3 Solution Strategies for the Flow Equations</b>	<b>10</b>
3.1 Reynolds Averaged Navier Stokes Equation . . . . .	10
3.2 PDF Methods . . . . .	12
3.3 Large Eddy Simulation . . . . .	14
3.4 Direct Numerical Simulation . . . . .	15
<b>4 Transported Joint PDF Methods</b>	<b>16</b>
4.1 Theory of Stochastic Processes . . . . .	16
4.1.1 Markov Processes . . . . .	16
4.1.2 Diffusion Processes . . . . .	18
4.2 Solution Strategy for PDF Transport Equations . . . . .	20
4.2.1 Eulerian and Lagrangian Systems . . . . .	21
4.2.2 From Modeled SDEs to PDF Transport Equations . . . . .	25
4.3 Numerical Solution Methods . . . . .	28
4.3.1 Hybrid Algorithm . . . . .	29

<b>5</b>	<b>Efficient Energy Consistency Scheme</b>	<b>34</b>
5.1	Idea, Assumptions and Constraints . . . . .	34
5.2	Modified Euler System . . . . .	35
5.3	Boundary Conditions . . . . .	38
5.4	Discussion . . . . .	41
<b>6</b>	<b>Accurate Time Integration Scheme of SDEs for Joint Statistics</b>	<b>42</b>
6.1	Numerical Integration Scheme . . . . .	43
6.1.1	Itô Calculus: Important Result . . . . .	43
6.1.2	Derivations . . . . .	44
6.2	Results . . . . .	48
6.3	Discussion and Conclusion . . . . .	53
<b>II</b>	<b>Modeling of Partially Premixed Turbulent Combustion</b>	<b>55</b>
<b>7</b>	<b>Review of Combustion Regimes and Modeling Approaches</b>	<b>57</b>
7.1	Premixed Combustion . . . . .	57
7.1.1	Phenomenological Observations . . . . .	57
7.1.2	Modeling Approaches . . . . .	59
7.2	Non-Premixed and Partially Premixed Combustion . . . . .	60
7.2.1	Phenomenological Observations . . . . .	60
7.2.2	Modeling Approaches . . . . .	61



	XI
<b>8 New Model for Partially Premixed Combustion</b>	<b>64</b>
8.1 Motivation . . . . .	64
8.2 Model Development . . . . .	66
8.2.1 Reactive IEM Mixing Model . . . . .	66
8.2.2 Progress Variable . . . . .	68
8.2.3 Scalar Dissipation Rate . . . . .	70
8.3 Validation and Results . . . . .	70
8.4 Conclusions . . . . .	93
8.5 Extension: 2D Laminar Flame Tables . . . . .	94
<b>9 Conclusions and Outlook</b>	<b>98</b>
<b>III Appendices</b>	<b>101</b>
<b>A Itô Calculus for Stochastic Differential Equations</b>	<b>103</b>
<b>B Local Particle Time Stepping Algorithm</b>	<b>105</b>
<b>References</b>	<b>109</b>
<b>Curriculum Vitae</b>	<b>115</b>
<b>Publication List</b>	<b>116</b>

## List of Figures

1	Hybrid FV - particle algorithm . . . . .	30
2	Characteristic boundaries of modified Euler system . . . . .	39
3	Reference boundary values for the modified Euler system . . . . .	40
4	Sample paths of the Langevin equation . . . . .	44
5	SDE integration: kinetic energy evolution . . . . .	50
6	SDE integration: evolution of mean particle position . . . . .	50
7	SDE integration: evolution of particle position variance . . . . .	51
8	SDE integration: evolution of mean particle velocity . . . . .	51
9	SDE integration: evolution of particle velocity variance . . . . .	52
10	SDE integration: evolution of particle position-velocity covariance . . . . .	52
11	SDE integration: velocity autocorrelation function . . . . .	53
12	Sketch of laminar premixed flame . . . . .	58
13	Contour plot of attached and lifted jet flame . . . . .	61
14	Sketch of Lifted jet flame . . . . .	65
15	Accessed regions in $Z$ - $h_s$ -space . . . . .	65
16	Notation for reactive IEM model . . . . .	67
17	Reactive IEM mixing model: different profiles . . . . .	69
18	Sketch of setup of Sandia flames . . . . .	71
19	Grid for Sandia flame simulations . . . . .	72
20	Sandia flame E: Favre mean downstream velocity . . . . .	72
21	Sandia flame E: downstream Reynolds stresses . . . . .	73
22	Sandia flame E: cross axial-radial Reynolds stresses . . . . .	73

23	Sandia flame E: Favre mean mixture fraction . . . . .	73
24	Sandia flame E: mixture fraction rms . . . . .	74
25	Sandia flame E: Favre mean temperature . . . . .	74
26	Sandia flame E: temperature rms . . . . .	74
27	Sandia flame E: scatter plots . . . . .	75
28	Sandia flame F: Favre mean downstream velocity . . . . .	76
29	Sandia flame F: downstream Reynolds stresses . . . . .	76
30	Sandia flame F: cross axial-radial Reynolds stresses . . . . .	77
31	Sandia flame F: Favre mean mixture fraction . . . . .	77
32	Sandia flame F: mixture fraction rms . . . . .	77
33	Sandia flame F: Favre mean temperature . . . . .	78
34	Sandia flame F: temperature rms . . . . .	78
35	Sandia flame F: scatter plots . . . . .	79
36	Location of PDF extraction in flame F . . . . .	80
37	Sandia flame F: joint $Z$ - $T$ -PDF at $x = 7.5 \times D_j$ . . . . .	81
38	Sandia flame F: joint $Z$ - $T$ -PDF at $x = 30 \times D_j$ . . . . .	82
39	Sandia flame F: joint $Z$ - $T$ -PDF at $x = 45 \times D_j$ . . . . .	83
40	Sandia flame F: joint $Z$ - $T$ -PDF at $x = 60 \times D_j$ . . . . .	84
41	Sandia flame F: marginal mixture fraction PDF at $x = 7.5 \times D_j$ . . . . .	85
42	Sandia flame F: marginal mixture fraction PDF at $x = 30 \times D_j$ . . . . .	86
43	Sandia flame F: marginal mixture fraction PDF at $x = 45 \times D_j$ . . . . .	87
44	Sandia flame F: marginal mixture fraction PDF at $x = 60 \times D_j$ . . . . .	88
45	Sandia flame F: marginal temperature PDF at $x = 7.5 \times D_j$ . . . . .	89
46	Sandia flame F: marginal temperature PDF at $x = 30 \times D_j$ . . . . .	90
47	Sandia flame F: marginal temperature PDF at $x = 45 \times D_j$ . . . . .	91
48	Sandia flame F: marginal temperature PDF at $x = 60 \times D_j$ . . . . .	92
49	Sketch of laminar flame sheet (flamelet solution) . . . . .	95
50	Sketch of igniting turbulent mixture field . . . . .	96
51	Laminar 2D triple flame setup . . . . .	97



## Nomenclature

Generally, Reynolds averaged quantities are denoted by angle brackets  $\langle \cdot \rangle$  and Favre averages by a tilde  $\tilde{\cdot}$ . For repeated indices the Einstein summation rule applies, if not mentioned otherwise. Bold printed variables are vector valued.

### Roman

<b>A</b>	drift vector in the Fokker-Planck equation (Eq. (4.4))
$a_i$	drift coefficients in the SDE's (Eq. (4.11))
<b><u>B</u></b>	diffusion matrix in the Fokker-Planck equation (Eq. (4.4))
$\bar{b}_{ij}$	diffusion coefficients in the SDE's (Eq. (4.11))
$C_\mu$	turbulent viscosity constant in the $k$ - $\epsilon$ model (Eq. (3.7))
$C_0$	model constant in the SLM (Eq. (4.35))
$C_3$	model constant in the Jayesh-Pope model (Eq. (4.38))
$C_{\omega 1}$	model constant in the Jayesh-Pope model
$C_{\omega 2}$	model constant in the Jayesh-Pope model
$C_\Omega$	model constant (conditional turb. frequency Eq. (4.36))
$C_\phi$	model constant in the IEM mixing model (Eq. (4.37))
$C_\chi$	scalar dissipation rate model constant
$C_u$	velocity CFL no. local particle time step alg. (app. B)
$C_\omega$	frequency CFL no. local particle time step alg. (app. B)
$c$	reaction progress variable
$c''$	Favre fluctuation of reaction progress variable
$c^*$	reaction progress variable of a particle
$\hat{c}$	speed of sound modified Euler system
$c_p$	specific heat at constant pressure
$\bar{c}_{p,\alpha}$	integrated spec. heat (const. press., species $\alpha$ , Eq. (2.10))
$\bar{c}_p$	specific heat at const. pressure of a mixture (Eq. (2.12))
$c_v$	specific heat at constant volume
$\bar{c}_{v,\alpha}$	integrated spec. heat (const. vol., species $\alpha$ , Eq. (2.11))
$\bar{c}_v$	specific heat at const. vol. of a mixture (Eq. (2.12))
$D_a$	Damköhler number ( $\tau_t/\tau_c$ ) (Eq. (7.1))
$D_P$	pilot burner diameter
$D_j$	jet diameter
$E_s$	total sensible energy (Eq. (2.14))
$e_s$	sensible energy (Eq. (2.13))
<b>F</b>	vector of arbitrary volume force (Eq. (2.3))
<b><math>F_x(\mathbf{w})</math></b>	$x$ -flux vector (Eq. (5.4))
<b><math>F_y(\mathbf{w})</math></b>	$y$ -flux vector (Eq. (5.5))
<b><math>\hat{F}_x(\hat{\mathbf{w}})</math></b>	$x$ -flux vector modified Euler system (Eq. (5.11))
<b><math>\hat{F}_y(\hat{\mathbf{w}})</math></b>	$y$ -flux vector modified Euler system (Eq. (5.11))

$\mathcal{F}(\mathbf{V}, \Psi, \mathbf{x}; t)$	mass density function (MDF) (Eq. (4.29))
$\mathcal{F}^*(\mathbf{V}, \Psi, \mathbf{x}; t)$	MDF of modeled random variables $\mathbf{U}^*$ , $\Phi^*$ and $\mathbf{X}^*$
$f(\mathbf{x}; t)$	position joint PDF
$f(\mathbf{x}_2; t_2   \mathbf{x}_0)$	joint PDF of $\mathbf{x}_2$ conditioned on $\mathbf{X}_0 = \mathbf{x}_0$ (Eq. (4.1))
$f(V; t)$	PDF of $U(t)$
$f(\mathbf{V}, \Psi   \mathbf{x}_0, t_0)$	conditional velocity-composition joint PDF (Eq. (4.25))
$f(\mathbf{V}, \Psi; \mathbf{x}, t)$	Eulerian velocity-compositions joint PDF
$f_L(\mathbf{V}, \Psi, \mathbf{x}; t   \mathbf{V}_0, \Psi_0, \mathbf{x}_0)$	Lagrangian joint PDF of $\mathbf{U}$ , $\Phi$ and $\mathbf{X}$
$f_L^*(\mathbf{V}, \Psi, \mathbf{x}; t   \mathbf{V}_0, \Psi_0, \mathbf{x}_0)$	modeled Lagr. joint PDF of $\mathbf{U}^*$ , $\Phi^*$ and $\mathbf{X}^*$
$f^*(\mathbf{V}, \Psi; \mathbf{x}, t)$	modeled Eulerian joint PDF of $\mathbf{U}^*$ and $\Phi^*$
$f'(\mathbf{V}, \Psi; \mathbf{x}, t)$	fine grained joint PDF of vel. and comp. (Eq. (4.23))
$f(\mathbf{V}, \Psi, \theta; \mathbf{x}, t)$	Eulerian joint PDF of $\mathbf{U}$ , $\Phi$ and $\omega$
$\hat{f}(\Psi; \mathbf{x}, t)$	composition joint FDF (Eq. (3.20))
$G(t)$	function of a stochastic process (appendix A)
$G(\mathbf{x}, t)$	level set function ( $G$ -equation)
$G(\mathbf{r}, \mathbf{x})$	low pass filter function in LES
$\hat{g}_{l,k}(\mathbf{x})$	top hat basis function for data extraction
$\hat{g}_{l,k}(\mathbf{x})$	bi- or tri-linear basis function for data extraction
$h_s$	sensible enthalpy (Eq. (2.13))
$h_s''$	Favre fluctuating enthalpy
$h_s^*$	modeled sensible particle enthalpy
$h_{f,\alpha}^0$	formation enthalpy of species $\alpha$
$\hat{h}(Z, \chi)$	mixing line function (Fig. 16)
$h_f(Z, \chi)$	enthalpy function of the steady flamelet solution (Fig. 16)
$h_{f1}(\chi)$	enthalpy on the left edge of the flame zone (Fig. 16)
$h_{f2}(\chi)$	enthalpy on the right edge of the flame zone (Fig. 16)
$J_i^\alpha$	diffusive flux of scalar $\alpha$ in $i$ th-direction
$K_a$	Karlovitz number ( $\tau_c/\tau_K$ ) (Eq. (7.2))
$\mathcal{Kn}$	Knudsen number ( $\lambda/l$ )
$k$	turbulent kinetic energy ( $1/2\widetilde{u_i u_i}$ )
$Le$	Lewis number ( $\Gamma_h/\Gamma_\alpha$ )
$L_r$	normalization length ( $U_r\tau$ )
$L_x$	length of computational domain
$L_y$	width of computational domain
$l$	length scale
$M$	total mass in a domain
Ma	Mach number
$m$	absolute mass
$m_\alpha$	absolute mass of species $\alpha$
$N_p$	number of particles in a computational cell
$N_s$	number of species
$\mathcal{P}$	turbulence production term ( $-\widetilde{u_i u_j} \partial \tilde{U}_i / \partial x_j$ )
$P$	ignition probability of a particle (Eq. (8.5))
$p$	pressure (Eq. (2.13))
$p_{\text{ref}}$	reference or ambient pressure

$\bar{p}$	filtered pressure
$p'$	fluctuating pressure
$q^*$	arbitrary particle property
$R$	specific gas constant (Eq. (2.8))
$\mathcal{R}_u$	universal gas constant (8.314472 J/(K mol))
$\mathbf{R}$	right hand side of Euler equation (Eq. (5.2))
$S$	entropy
$\tilde{S}_c$	Favre averaged progress var. source term (Eq. (8.6))
$S_{E_s}$	chemical reaction energy source term (Eq. (2.15))
$S_h$	chemical reaction enthalpy source term
$S_\phi, S_\alpha$	chemical reaction scalar source term (Eq. (2.16))
$S_\omega$	turbulence frequency source term (Eq. (4.39))
$\tilde{S}_{ij}$	Favre averaged rate of strain tensor (Eq. (3.11))
$s_L$	laminar flame speed
$T$	temperature
$T$	time scale of a random process
$\mathbb{T}$	deviatoric stress tensor
$T_{ij}$	residual stress tensor (Eq. (3.19))
$T_{st}$	flame temperature at the stoichiometric point
$t$	time coordinate
$t_0$	initial time
$\Delta t$	time interval, time step
$U(t)$	stochastic process
$\mathbf{U}(t)$	stochastic process for particle velocity (Eq. (6.5))
$U_d$	inlet velocity (2D flame tables)
$\mathbf{U}(\mathbf{X}, t)$	Eulerian fluid velocity
$\mathbf{U}^*(t)$	modeled fluid particle velocity
$\mathbf{U}^*(\mathbf{X}, t)$	modeled Eulerian fluid velocity
$\mathbf{U}^+(\mathbf{X}_0, t)$	velocity of a real Lagrangian fluid particle (Eq. (4.17))
$\bar{\mathbf{U}}$	filtered velocity vector (Eq. (3.16))
$\mathbf{U}''$	Favre fluctuation of filtered velocity (Eq. (3.17))
$U_r$	normalization velocity ( $\sqrt{2k_0/3}$ )
$\mathbf{u}$	Favre fluctuating velocity vector (Eq. (3.3))
$\mathbf{u}'$	residual velocity vector (Eq. (3.15))
$V$	spatial volume
$\mathbf{V}$	sample space variable of the velocity vector $\mathbf{U}$
$\mathbf{v}$	sample space variable of Favre fluctuating velocity $\mathbf{u}$
$\mathcal{W}(\mathbf{x} \mathbf{z}, t)$	jump probability (sec. 4.1.1)
$W_\alpha$	molecular weight of species $\alpha$
$W(t)$	Wiener process
$\mathbf{W}(t)$	vector-valued Wiener process (Eq. (4.14))
$\mathbf{w}$	vector of conserved variables (Eq. (5.3))
$\hat{\mathbf{w}}$	conserved variables modified Euler eq. (Eq. (5.11))
$X(t)$	random variable evolving in time
$\mathbf{X}(t)$	vector-valued random variable

$\mathbf{X}(t)$	evolution of particle position (Eq. (6.4))
$\mathbf{X}^*(t)$	modeled particle position
$\mathbf{X}^+(\mathbf{X}_0, t)$	position of a Lagrangian fluid particle
$\mathbf{X}_0$	random initial position at $t = t_0$
$\mathbf{x}$	spatial coordinate vector
$\mathbf{x}$	sample space var. of vector valued random process $\mathbf{X}(t)$
$\mathbf{x}_0$	initial spatial coordinates
$\mathbf{Y}$	vector of species mass fractions
$Y_\alpha$	species mass fraction of species $\alpha$ (Eq. (2.9))
$Z(\mathbf{x}, t)$	mixture fraction
$Z_{f1}$	left bound of the flammable range (Fig. 16)
$Z_{f2}$	right bound of the flammable range (Fig. 16)
$Z_j$	jet mixture fraction
$Z_{co}$	coflow mixture fraction



## Greek

$\alpha$	model parameter ignition probability (Eq. (8.5))
$\Gamma_T$	heat diffusion coefficient
$\Gamma_h$	heat diffusion coefficient
$\Gamma$	general diffusion coefficient
$\gamma'$	ratio of specific heat capacities (Eq. (2.12))
$\delta(\mathbf{X} - \mathbf{x})$	Dirac delta function
$\delta_{ij}$	Kronecker delta
$\epsilon$	very small number
$\varepsilon$	dissipation of turbulent kinetic energy
$\eta(\mathbf{x}, t)$	field of local particle time steps (appendix B)
$\eta^*$	local particle time step (appendix B)
$\theta$	sample space variable of turbulence frequency $\omega$
$\lambda$	mean free path length
$\hat{\lambda}$	Eigenvalues of modified Euler system (Eq. (5.16))
$\mu$	dynamic viscosity
$\nu$	kinematic viscosity
$\nu_t$	turbulent or eddy viscosity
$\xi$	random number (normal Gaussian distributed)
$\xi(t)$	general random term
$\rho$	fluid density
$\rho^+(\mathbf{X}_0, t)$	density of a real Lagrangian fluid particle (Eq. (4.17))
$\sigma$	variance parameter Ornstein-Uhlenbeck proc. (Eq. (4.8))
$\tau$	flow time scale
$\tau_b$	burning time
$\tau_c$	chemical time scale
$\tau_K$	Kolmogorov time scale
$\tau_t$	integral turbulent flow time scale
$\Phi$	composition vector
$\Phi^*(t)$	modeled particle composition
$\Phi^+(\mathbf{X}_0, t)$	comp. of a real Lagrangian fluid particle (Eq. (4.17))
$\phi$	scalar components
$\phi''_\alpha$	Favre fluctuation of scalar component $\alpha$
$\chi$	scalar dissipation rate (Eq. (7.5))
$\Psi$	sample space vector of compositions $\Psi$
$\Omega$	conditioned turbulence frequency
$\Omega$	computational domain
$\omega$	turbulence frequency ( $\varepsilon/k$ )
$\omega^*(t)$	modeled particle turbulence frequency

## Subscripts

$Y_\alpha$	species or scalar $\alpha$ in a mixture
$U_b$	boundary value
$q_{\text{ref}}$	some reference value
$q_0$	initial value

### Superscripts

$q^{FV}$	from finite volume algorithm calculated quantity
$q^P$	from particle algorithm calculated quantity
$q^n, q^{n+1}$	time stamp, old and new time level
$X^*$	modeled particle quantity
$X^+$	real fluid particle quantity

### Symbols

$D/Dt$	substantial or material derivative $(\partial/\partial t + \mathbf{U} \cdot \nabla)$
$\tilde{D}/\tilde{D}t$	change along mean fluid particle paths $(\partial/\partial t + \tilde{\mathbf{U}} \cdot \nabla)$
$\mathbf{U} \otimes \mathbf{U}$	outer (dyadic) vector or tensor product
$\mathbf{U} \cdot \mathbf{U}$	inner vector or tensor product
$\nabla$	gradient operator
$\max(m, n)$	the greater out of $m$ and $n$
$\min(m, n)$	the smaller out of $m$ and $n$
$\forall i$	for all $i$

### Abbreviations

DNS	direct numerical simulation
FDF	filtered density function
FV	finite volume
IEM	interaction by exchange with the mean mixing model
ISAT	in situ adaptive tabulation
LES	large eddy simulation
MC	mapping closure
MDF	mass density function
PDF	probability density function
OU	Ornstein-Uhlenbeck process
PSP	parametrized scalar profile
RANS	reynolds averaged Navier Stokes
REDIM	reduced intrinsic manifold
rms	root mean square
SDE	stochastic differential equation
SLM	simplified Langevin model

# 1 Preface

It is a fact that the knowledge of the physics in turbulent reactive flows is far from being complete. Since more than a century scientists try to understand and control combustion events in order to develop better and particularly more efficient combustion devices. After the availability of appropriate mathematical tools, engineers and scientists started to describe and calculate simple reactive flows. A lot of basic theoretical findings and modeling ideas had been developed during this early times, but only later, when computers became available, more complicated flames could be simulated.

There may be distinguished between three stages which are responsible for good simulation results. First, one has to know and understand the underlying physical and chemical processes of the considered scenario. That can be obtained for instant by experimental investigations. Examples of such processes in turbulent combustion are general mutual interactions of turbulent flow structures with chemical processes, flow laminarization, flame front propagation, mixing dynamics of chemical components or extinction and re-ignition events. Afterwards, the correct mathematical formulation (governing equations), which accurately describe the involved physics and the chemistry, must be developed. In the case here, the governing equations for the flow are mass conservation, the Navier Stokes equation, the energy equation, the equation of state and the reaction balance equations for the chemistry. Usually, it is not feasible to solve the governing equations for a practical problem directly (so called "direct numerical simulation" (DNS)). Instead, the fastest and smallest processes, which impose the most severe time step and grid resolution restrictions on the numerical scheme, are omitted. The effect of these neglected processes must then be modeled appropriately. A common way of achieving this is by splitting the dependent variables (i.e. velocity, pressure, energy, scalars) into a mean and a fluctuating part and then deriving moment equations. In simple methods one solves for mean and variance quantities and models the influence of the higher moments. More general are the joint probability density function (PDF) methods. From stochastic theory a general joint PDF transport equation can be derived. This equation becomes the governing equation for turbulent reactive flows by including the physical conservation laws. Pope [63] developed the foundations of this approach.

Next, two algorithmic issues are shortly outlined, which are presented in detail in part I of this work.

The governing joint PDF transport equation has to be advanced in a high dimensional space, since it contains at least three velocity and  $N_s + 1$  scalar components (i.e.  $N_s$

species mass fractions and enthalpy) plus time. Hence typically a particle Monte Carlo solution algorithm is employed, where the PDF at each location is represented by stochastic particles. A problem of Monte Carlo methods is that a large number of particles must be applied to keep the statistical and the deterministic bias errors small. Therefore, Jenny et al. [36] and Muradoglu et al. [49] successfully developed a more efficient algorithm, called hybrid finite volume-particle method. The idea behind this approach is to compute mean fields with a common finite volume method and to obtain all the unclosed terms ("fluctuating" quantities) by a particle method. This has the major advantage that mean quantities used in the particle evolution equations must not be extracted from the particle field itself and instead, are calculated by the finite volume scheme. A drawback of the hybrid approach is that some fields are computed twice, i.e. in the finite volume and in the particle part of the algorithm, which gives rise to consistency requirements. The consistency is fulfilled by the governing equations, but due to computational imprecisions it is not automatically achieved on the algorithmic level. Hence, correction schemes have to be applied to enforce a consistent overall algorithm. The focus in this lies on the energy consistency. An alternative way, other than a correction scheme, is presented to achieve energy consistency by determining the mean energy field from the particles alone and using it directly in the finite volume scheme for computing the mean velocity and pressure fields. This approach is related to the method of Muradoglu [51], but here, it is rather a change of concept than a correction scheme.

From stochastic theory it is known that a PDF  $f(x;t)$ , which evolves in time according to a Fokker-Planck or more general a Kolmogorov-Chapman equation can consistently be represented by a process in  $x$ -space governed by a stochastic differential equation (SDE). Here, the modeled PDF transport equation for turbulent reactive flows is a Fokker-Planck equation and the model fluid particles used in the Monte Carlo solution algorithm follow laws, which are typically in the form of Langevin equations. This class of SDE's has a deterministic drift and a stochastic diffusion term, usually represented by a Brownian motion or a Wiener process. Such Langevin equations can involve very small timescales and hence impose severe time step restrictions on the time integration schemes. Here, a integration scheme based on the approach by Minier et al. [47] for the position and the velocity of a particle is developed, which is exact in time for arbitrary large time steps and also honors the single and joint statistics of the involved quantities. This is achieved through the analytical integration of the stochastic terms in the particle evolution equations by means of Itô calculus and splitting up the stochastic term of the integrated velocity equation. The fact that the Wiener increments are all independent and Gaussian distributed is used to obtain the final scheme. A homogeneous, isotropic turbulent flow test case proves the accuracy of the new scheme compared to an ordinary second order finite differencing integration scheme.

In part II of the thesis, the focus lies on the modeling of turbulent partially premixed combustion. As the name implies, such flames feature properties of both diffusion and premixed combustion. Usually the basic physical setup is the one of a non-premixed flame, but due to high scalar dissipation rates in some regions, local extinction occurs and the mixture becomes partially premixed. Farther downstream the mixture can re-ignite and

processes as for instance flame propagation occur, similar as in premixed flames.

Hence, existing model approaches in the context of RANS turbulence modeling are often a combination of the flamelet approach [56] and a level set (e.g.  $G$ -equation [80]) or a progress variable approach. Numerous researchers followed this track with some success; e.g.: Bradley et al. [10], [7], [8] and [9], Sanders and Lamers [69], Müller et al. [48], Kronenburg [38], Vervisch [75], Ihme [33].

Two main advantages of transported PDF methods and the Monte Carlo solution algorithm are that the modeling can be done in quite a natural manner by considering the evolution of Lagrangian model fluid particles and the availability of joint statistics of different quantities. The combustion model presented in this work combines a flamelet with a progress variable approach. Based on the joint statistics of mixture fraction, scalar dissipation rate and progress variable, physically motivated particle paths in mixture fraction-enthalpy space are constructed, on which the model fluid particles advance in time. A conventional molecular mixing model is applied to evolve the mixture fraction, whereas a so called reactive mixing model describes the evolution of reactive scalars (here the enthalpy). Additionally, an ignition probability for the progress variable of a model fluid particle has to be modeled.

A short outline of the thesis structure is given in the following. In chapter 2, the governing equations of fluid motion and thermo-chemistry are presented, followed in chapter 3 by an overview of broadly used numerical solution and modeling strategies. Chapter 4 explains the basic foundation of transported PDF methods and some aspects of their numerical solution. The energy consistency issue is addressed in chapter 5 and in chapter 6 a time accurate scheme to integrate stochastic differential equation is explained.

The first chapter of the modeling part (chapter 7) reviews and explains the various physical processes in different combustion regimes and their modeling approaches. The development of a new model for partially premixed combustion and its validation is the topic of chapter 8. Finally, in chapter 9 the work is shortly summarized, conclusions are drawn and an outlook is given.



Part I

# PDF Algorithm





## 2 Governing Equations of Fluid Motion and Thermo-Chemistry

In this chapter the physical and mathematical basics for the understanding of turbulent reactive flows are introduced. The governing equations for the fluid flows considered in this work are the Navier Stokes equation, which include mass-, momentum- and energy conservation laws. The thermodynamical state of the fluid is governed by chemical reactions, heat diffusion, convection and an equation of state. At low Mach numbers, the influence of the chemical reactions on the hydrodynamics is only through the fluid density.

### 2.1 Fluid Motion Equations

The mathematical and physical description of the fluid flow is based on the continuum hypotheses. This means that the scales we are interested in are much larger than the scales of molecular motions. Usually, the Knudsen number is used to determine the validity of this assumption. It is specified as

$$\mathcal{Kn} \equiv \lambda/l, \quad (2.1)$$

where  $\lambda$  is the mean free path length of molecules in the gas and  $l$  denotes a representative physical length scale. If  $\mathcal{Kn} \ll 1$  the continuum assumption is valid. In typical flows considered in this work the Knudsen number is of the order  $10^{-3}$  or even smaller. After accepting the continuum hypotheses, macroscopic fluid properties at different locations in space and in time can be defined. Most important are the fluid density  $\rho(\mathbf{x}, t)$ , the velocity  $\mathbf{U}(\mathbf{x}, t)$  and the pressure  $p(\mathbf{x}, t)$ . The three components of the physical space coordinate  $\mathbf{x}$  are  $[x_1, x_2, x_3]^T$  and  $t$  is the time.

First we introduce the mass conservation equation, which states that the rate of change of fluid mass in a fixed control volume equals the sum of the fluxes over the control volume boundaries (if the control volume is free of a sink or source). The continuity equation in differential form reads

$$\frac{\partial \rho}{\partial t} + \nabla \cdot (\rho \mathbf{U}) = 0. \quad (2.2)$$

The second fundamental law is the momentum balance or more specific in fluid dynamics the vectorial Navier-Stokes equation. It describes the momentum balance (Newton's second

law) of a fluid control volume and relates the change of momentum to the body and surface forces. In the general case of a compressible and viscous fluid the Navier-Stokes equation takes the form

$$\frac{\partial \rho \mathbf{U}}{\partial t} + \nabla \cdot (\rho \mathbf{U} \otimes \mathbf{U}) = -\nabla p + \nabla \cdot \mathbb{T} + \mathbf{F}. \quad (2.3)$$

On the left side of the equal sign are the momentum accumulation and the convective transport terms and on the right side are the influences of the pressure gradient, the divergence of the deviatoric stress tensor and arbitrary external volume forces. Since no external forces are considered here (for instance gravity is neglected in our case) the simplified equation reads

$$\frac{\partial \rho \mathbf{U}}{\partial t} + \nabla \cdot (\rho \mathbf{U} \otimes \mathbf{U}) = -\nabla p + \nabla \cdot \mathbb{T}. \quad (2.4)$$

Eqs. (2.2) and (2.4) provide four relations (note that Eq. (2.4) is a vector equation) for five unknowns. These unknowns are the three velocity components  $\mathbf{U} = [U_1, U_2, U_3]^T$ , the density  $\rho$  and the pressure  $p$ . So we do need a fifth equation to fully determine the system and for our purpose the following energy equation for the total sensible energy is an appropriate choice

$$\frac{\partial \rho E_s}{\partial t} + \nabla \cdot (\mathbf{U} (\rho E_s + p)) = S_{E_s} + \nabla \cdot (\Gamma_T \nabla T) - \nabla \cdot \left( \rho \sum_{k=1}^{N_s} h_{s,k} Y_k V_k \right). \quad (2.5)$$

$S_{E_s}$  is the energy source term, e.g. due to chemical reactions and the last two terms are heat fluxes. The heat fluxes consist of two contributions, heat diffusion described by the Fourier's law (second last term) with the heat diffusion coefficient  $\Gamma_T$  and heat flux due to relative species motion of species with different sensible enthalpies. This term includes the sensible enthalpy  $h_{s,k}$  of species  $k$ , the species mass fraction  $Y_k$ , the species diffusion velocity  $V_k$  and  $N_s$  is the number of species. In this work we will disregard the heat flux due to species motion since it is much smaller than the chemical source term. Furthermore, viscous heating of the fluid and effects arising from volume forces are neglected in Eq. (2.5). The exact definition of  $E_s$  and its relation to the pressure  $p$  is given in the next section.

Additionally, the evolution equation of a scalar  $\phi(\mathbf{X}, t)$  in a reactive, turbulent flow field is given by

$$\frac{\partial \rho \phi}{\partial t} + \nabla \cdot (\rho \mathbf{U} \phi) = \nabla \cdot (\Gamma \nabla \phi) + \rho S_\phi, \quad (2.6)$$

where  $\Gamma$  is the species diffusion coefficient and  $S_\phi$  is the change of the scalar due to chemical reactions.

## 2.2 Thermo-Chemistry

Since this work is about reactive flows, an overview of the thermodynamic fluid properties and their relations is given here.

The fluid is treated as ideal gas mixture with  $N_s$  species and the ideal gas law reads

$$p = \rho R T, \quad (2.7)$$

where

$$R = \mathcal{R}_u \sum_{\alpha=1}^{N_s} \frac{Y_\alpha}{W_\alpha} \quad (2.8)$$

is the specific gas constant (for the mixture),  $p$  the thermodynamic pressure,  $T$  the temperature and  $\mathbf{Y} = [Y_1, Y_2, \dots, Y_{N_s}]^T$  are the species mass fractions. The molecular weight of species  $\alpha$  is denoted by  $W_\alpha$  and  $\mathcal{R}_u$  is the universal gas constant. In Eq. (2.7) all parameters are bulk properties of the mixture. The mass fractions  $Y_\alpha$  are defined by

$$Y_\alpha = \frac{m_\alpha}{m}, \quad (2.9)$$

where  $m_\alpha$  is the mass of species  $\alpha$  in a fluid volume and  $m$  is the total mass in this volume. Using the specific heats at constant pressure and constant volume for each species  $\alpha$ ,  $c_{p,\alpha}$  and  $c_{v,\alpha}$ , respectively, the quantities

$$\bar{c}_{p,\alpha}(T) = \frac{1}{T} \int_{T_0}^T c_{p,\alpha}(T') dT' \quad \text{and} \quad (2.10)$$

$$\bar{c}_{v,\alpha}(T) = \frac{1}{T} \int_{T_0}^T c_{v,\alpha}(T') dT', \quad (2.11)$$

are introduced. Together with the definitions

$$\bar{c}_p = \sum_{\alpha=1}^{N_s} Y_\alpha \bar{c}_{p,\alpha}, \quad \bar{c}_v = \sum_{\alpha=1}^{N_s} Y_\alpha \bar{c}_{v,\alpha}, \quad \gamma' = \frac{\bar{c}_p}{\bar{c}_v}, \quad \text{and} \quad \bar{c}_p - \bar{c}_v = R, \quad (2.12)$$

the sensible energy, the sensible enthalpy and the pressure can be expressed as

$$e_s = \bar{c}_v T, \quad h_s = \bar{c}_p T \quad \text{and} \quad p = \rho e_s (\gamma' - 1). \quad (2.13)$$

Eq. (2.5) is the transport equation for the total sensible energy. The definition of  $E_s$  is given by

$$E_s(\mathbf{Y}, T) = e_s(\mathbf{Y}, T) + \frac{1}{2} \mathbf{U}^2. \quad (2.14)$$

The source term of  $E_s$ ,  $S_{E_s}$ , is the net energy gain or loss due to chemical reactions of the mixture and reads

$$S_{E_s} = - \sum_{\alpha=1}^{N_s} S_\alpha(\mathbf{Y}, p, T) h_{f,\alpha}^0, \quad (2.15)$$

where  $h_{f,\alpha}^0$  is the formation enthalpy of species  $\alpha$  at a reference temperature  $T_0$ . A species  $\alpha$  in a homogeneous mixture evolves due to chemical reactions by

$$\frac{dY_\alpha}{dt} = S_\alpha(\mathbf{Y}, p, T). \quad (2.16)$$

The transport equation for species mass fraction  $Y_\alpha$  is defined by Eq. (2.6), if we set  $\phi = Y_\alpha$  and  $S_\phi = S_\alpha$ . In this case  $\Gamma$  is the diffusion coefficient of species  $\alpha$  in the mixture. Though, one has to be careful in applying Fick's law for multi species reacting flows. See chapter 1.1.4 in the textbook of Poinso and Veynante [60] for a more detailed discussion.

### 3 Solution Strategies for the Flow Equations

Eqs. (2.2), (2.4), (2.5) and (2.6) of section 2.1 form a complete set of rules for the description of compressible, low Mach number, turbulent and reactive flows. This section here gives an overview of simulation approaches for solving the set of governing equations numerically. The most common approaches are based on a statistical description of the flow and Reynolds averaging of the basic equations (RANS modeling). More high fidelity methods like large eddy simulation (LES) and direct numerical simulations (DNS) involve less or no modeling, but require an enormous amount of computational power.

#### 3.1 Reynolds Averaged Navier Stokes Equation

The basic idea of the RANS approaches is to derive transport equations for statistical moments of the flow properties. Reynolds (1894) applied this method the first time to the flow field velocity  $\mathbf{U}(\mathbf{x}, t)$ . He split up the velocity in its mean and fluctuating parts, inserted the decomposed velocity into the Navier-Stokes equation and took subsequently the average of the resulting equation. In reactive flow formulations it is usual to apply Favre instead of the Reynolds decomposition to avoid terms containing the fluctuating density. The Favre decomposition of the velocity is performed in the following way,

$$\mathbf{U}(\mathbf{x}, t) = \tilde{\mathbf{U}}(\mathbf{x}, t) + \mathbf{u}(\mathbf{x}, t), \quad (3.1)$$

where  $\tilde{\cdot}$  denotes a Favre averaged quantity. Favre averages are density weighted averages:

$$\tilde{\mathbf{U}} = \frac{\langle \rho \mathbf{U} \rangle}{\langle \rho \rangle} \quad \text{and} \quad (3.2)$$

$$\langle \rho \mathbf{u} \rangle = \langle \rho \rangle \tilde{\mathbf{u}} = 0. \quad (3.3)$$

If the Favre decomposed velocity (3.1) is substituted into the continuity equation (2.2) and subsequently the Reynolds average of the whole equation is taken, the Reynolds averaged continuity equation becomes

$$\frac{\partial \langle \rho \rangle}{\partial t} + \frac{\partial \langle \rho \rangle \tilde{U}_i}{\partial x_i} = 0. \quad (3.4)$$

Note that Einstein index summation convention for repeated indexes is applied if not mentioned otherwise. Doing the same thing with the Navier-Stokes equation (2.4), the RANS equation is recovered and reads

$$\frac{\partial \langle \rho \rangle \tilde{U}_j}{\partial t} + \frac{\partial \langle \rho \rangle \tilde{U}_j \tilde{U}_i}{\partial x_i} = \frac{\partial}{\partial x_i} \left[ \mu \left( \frac{\partial \tilde{U}_j}{\partial x_i} + \frac{\partial \tilde{U}_i}{\partial x_j} + \frac{\partial \langle u_j \rangle}{\partial x_i} + \frac{\partial \langle u_i \rangle}{\partial x_j} \right) \right] - \frac{\partial \langle \rho \rangle \widetilde{u_i u_j}}{\partial x_i} - \frac{\partial \langle p \rangle}{\partial x_j}. \quad (3.5)$$

Note that the bulk viscosity is not considered in our case. In the first term on the right hand side quantities as  $\partial \langle u_j \rangle / \partial x_i$  can be neglected since in virtually all flows  $\partial \tilde{U}_j / \partial x_i \gg \partial \langle u_j \rangle / \partial x_i$  applies. The crucial difference between the Navier-Stokes equation (2.4) and the RANS equation (3.5) is the second term on the right hand side, which stems from the nonlinear convection. Terms like  $\widetilde{u_i u_j}$  are called Reynolds stresses. The denotation as stresses arises from the fact that they have a similar effect on the flow as the viscous stresses. It is a momentum transfer caused by the fluctuating velocity components. The specification of the Reynolds stresses constitutes the closure problem in RANS modeling. One approach is to lump the effect of the Reynolds stresses into one variable, the so called eddy viscosity  $\nu_t$ . This approach is called the turbulent-viscosity hypotheses (Boussinesq, 1877) and states that the deviatoric Reynolds stress tensor is proportional to the mean rate of strain tensor, i.e.

$$-\widetilde{u_i u_j} + \frac{2}{3} \tilde{k} \delta_{ij} = \nu_t \left( \frac{\partial \tilde{U}_i}{\partial x_j} + \frac{\partial \tilde{U}_j}{\partial x_i} \right) - \nu_t \frac{2}{3} \frac{\partial \tilde{U}_k}{\partial x_k} \delta_{ij}. \quad (3.6)$$

To determine the eddy viscosity, a length and a time scale of the turbulent flow is required. The most common approaches are two equation models, where modeled transport equations for the averaged kinetic energy  $\tilde{k}$  and the dissipation  $\tilde{\varepsilon}$  (Jones and Launder [37]) or the turbulence frequency  $\tilde{\omega}$  [78] are solved. With these quantities, the eddy viscosity can be evaluated as

$$\nu_t = C_\mu \frac{\tilde{k}^2}{\tilde{\varepsilon}} \quad \text{or} \quad \nu_t = C_\mu \frac{\tilde{k}}{\tilde{\omega}}, \quad (3.7)$$

where  $C_\mu$  is a model constant. The definitions of  $\tilde{k}$ ,  $\tilde{\varepsilon}$  and  $\tilde{\omega}$  are

$$\tilde{k} \equiv \frac{1}{2} \widetilde{u_i u_i}, \quad (3.8)$$

$$\tilde{\varepsilon} \equiv 2\nu \tilde{S}_{ij} \tilde{S}_{ij} \quad \text{and} \quad (3.9)$$

$$\tilde{\omega} \equiv \frac{\tilde{\varepsilon}}{\tilde{k}}, \quad (3.10)$$

respectively, with the Favre averaged rate of strain tensor

$$\tilde{S}_{ij} \equiv \frac{1}{2} \left( \frac{\partial \tilde{U}_i}{\partial x_j} + \frac{\partial \tilde{U}_j}{\partial x_i} \right). \quad (3.11)$$

The class of two equation models together with the conservation laws form a closed set of equations and no other flow dependent information is needed (unlike zero or most one equation models). See for instance Pope's book [66] for usability and limitations of such models.

A higher closure level is attained by the class of Reynolds stress models. In this approach, transport equations for the different Reynolds stresses are solved and further models are needed to describe the effects of the emerging unclosed terms, e.g. triple correlations. The most important and also most difficult term to be modeled is the pressure rate of strain tensor, which is responsible for the redistribution of kinetic energy among the different coordinate directions. For more insight it is referred to some original works Rotta [68], Launder et al. [40], Lumley and Newman [43], Sarkar and Speziale [70], Chung and Kim [17].

The Reynolds averaged scalar conservation equation

$$\frac{\partial \langle \rho \rangle \tilde{\phi}_\alpha}{\partial t} + \frac{\partial \langle \rho \rangle \tilde{U}_j \tilde{\phi}_\alpha}{\partial x_j} = \frac{\partial}{\partial x_j} \left[ \Gamma_\alpha \frac{\partial \tilde{\phi}_\alpha}{\partial x_j} \right] - \frac{\partial \langle \rho \rangle \widetilde{u_j \phi''_\alpha}}{\partial x_j} + \tilde{S}_\phi(\phi) \quad (3.12)$$

has a similar structure as the RANS equation. Note that quantities like  $\phi''_\alpha$  are Favre fluctuations. In the context of two-equation models, the scalar flux term (second term on the right hand side) is usually modeled by a gradient-diffusion assumption, which is known to be problematic in combustion modeling due to counter gradient diffusion effects (see Peters [58] sec. 2.4). The mean chemical source term  $\tilde{S}_\phi$  depends on the scalar distribution and the assumption that  $\tilde{S}_\phi(\phi) = S_\phi(\tilde{\phi})$  is a very bad approximation due to the non-linearity of the source term.

In the next subsection a method which overcomes some major drawbacks of two equation RANS models is presented, and which is very attractive especially for turbulent reactive flows.

## 3.2 PDF Methods

In PDF methods, different levels of closure can be achieved. The simplest approaches are the presumed PDF methods, where the statistical distribution of a certain quantity is parameterized (e.g. as a function of its mean and variance). This requires a good a priori knowledge of the quantity's behavior in the turbulent flow. Usually one assumes the PDF of the scalars (or compositions) in order to close the chemical source term. If for example a Beta-PDF is assumed for the scalar distribution, only the two transport equations for the scalar mean and variance have to be solved in order to determine the whole PDF. This approach has to be combined with closure models for the turbulent quantities, e.g. two equation models as described in the previous subsection.

More involved approaches are transported PDF methods, where an evolution equation for a one-time, one-point Eulerian PDF is solved. This approach can be further subdivided into different levels of completeness by the amount of information that is packed into the PDF. Initially, only the scalar joint PDF was considered, then also the velocity and later the turbulence frequency were included in the probability density function. Note that in all these approaches the chemical source term  $\tilde{S}_\phi(\phi)$  appears in closed form. Incorporating all turbulent and scalar quantities in the PDF is the most rigorous approach in the PDF modeling framework and was developed by Pope [63].

Here the Eulerian joint PDF  $f(\mathbf{V}, \Psi, \theta; \mathbf{x}, t)$  at time  $t$  and at location  $\mathbf{x}$  of velocity  $\mathbf{U}(\mathbf{x}, t)$ , compositions  $\Phi(\mathbf{x}, t)$  and turbulence frequency  $\omega(\mathbf{x}, t)$  is considered. The sample space variables corresponding to  $\mathbf{U}$ ,  $\Phi$  and  $\omega$  are  $\mathbf{V}$ ,  $\Psi$  and  $\theta$ , respectively. Here and from now on it is assumed that the density is always a function of  $\Phi$  only, i.e. independent of pressure (given a constant reference pressure). Thus, with standard techniques (see textbooks e.g. Fox [27] or Pope [66]), the following exact transport equation for  $f(\mathbf{V}, \Psi, \theta; \mathbf{x}, t)$  can be derived

$$\begin{aligned} \rho(\Psi) \frac{\partial f}{\partial t} + \rho(\Psi) V_j \frac{\partial f}{\partial x_j} = & - \frac{\partial}{\partial V_j} \left[ \rho(\Psi) \left\langle \frac{DU_j}{Dt} \mid \mathbf{V}, \Psi, \theta \right\rangle f \right] \\ & - \frac{\partial}{\partial \Psi_\alpha} \left[ \rho(\Psi) \left\langle \frac{D\Phi_\alpha}{Dt} \mid \mathbf{V}, \Psi, \theta \right\rangle f \right] \\ & - \frac{\partial}{\partial \theta} \left[ \rho(\Psi) \left\langle \frac{D\omega}{Dt} \mid \mathbf{V}, \Psi, \theta \right\rangle f \right]. \end{aligned} \quad (3.13)$$

This equation is exact, since no physical assumptions are made yet. The three conditional expectation terms on the right hand side describe the evolution of the PDF in velocity, composition and frequency space, respectively. If we insert the known physical relations for the substantial derivatives  $DU_j/Dt$  (Navier-Stokes equation) and  $D\phi_\alpha/Dt$  (scalar conservation), then Eq. (3.13) reads

$$\begin{aligned} \rho(\Psi) \frac{\partial f}{\partial t} + \rho(\Psi) V_j \frac{\partial f}{\partial x_j} & - \frac{\partial \langle p \rangle}{\partial x_j} \frac{\partial f}{\partial V_j} + \frac{\partial \langle \tau_{ij} \rangle}{\partial x_i} \frac{\partial f}{\partial V_j} \\ & - \frac{\partial \langle J_i^\alpha \rangle}{\partial x_i} \frac{\partial f}{\partial \Psi_\alpha} + \frac{\partial}{\partial \Psi_\alpha} [\rho(\Psi) S_\alpha(\Psi) f] = \\ & - \frac{\partial}{\partial V_j} \left[ \left\langle \left( \frac{\partial \tau'_{ij}}{\partial x_i} - \frac{\partial p'}{\partial x_j} \right) \mid \mathbf{V}, \Psi, \theta \right\rangle f \right] \\ & - \frac{\partial}{\partial \Psi_\alpha} \left[ \left\langle -\frac{\partial J_i'^\alpha}{\partial x_i} \mid \mathbf{V}, \Psi, \theta \right\rangle f \right] \\ & - \frac{\partial}{\partial \theta} \left[ \rho(\Psi) \left\langle \frac{D\omega}{Dt} \mid \mathbf{V}, \Psi, \theta \right\rangle f \right]. \end{aligned} \quad (3.14)$$

Effects of the mean pressure and the chemical source term are closed (third and sixth terms on the left hand side, respectively) and all the conditional expectations on the right hand side have to be modeled. Note that the fourth and fifth left hand side terms are very small at high Reynolds numbers and therefore are ignored from now on. The first

conditional moment in Eq. (3.14) describes the influence of the gradients of the fluctuating viscous stresses  $\tau'_{ij}$  and the fluctuating pressure  $p'$ . The influence of the molecular diffusion is contained in the second term, where  $J_i'^\alpha$  is the molecular diffusion flux of scalar  $\alpha$  in the  $i$ th-direction. Finally, the third term accounts for the evolution in frequency space. Note that a physical model for the conditional mean of the substantial derivative of the turbulence frequency is considered later in this work. The modeling of all those terms is closely connected to the numerical solution strategy of the PDF transport equation and is covered in more detail in secs. 4.2.2 and 4.3.

### 3.3 Large Eddy Simulation

Large-eddy simulation (LES) is an approach to overcome the high computational cost of the direct numerical simulation (DNS, see next subsection) and to eliminate some of the limitations in RANS modeling. The main idea is to resolve the large, energy containing scales and to model the effect of the small unresolved or subgrid scales. A major shortcoming of RANS methods is the problem in calculating flows with dominant unsteady effects like for example vortex shedding or separation and also the model parameter dependency on the flow geometry. In the LES approach these large scale motions are resolved and should be calculated accurately. On the other hand, the smallest scales are more universal (Kolmogorov hypotheses) and it should be easier to model their effect in a general way.

Mathematically, a low pass filter  $G(\mathbf{r}, \mathbf{x})$  is applied to the governing equations to cut off the high frequency part of the energy spectrum. The velocity field is split up in a filtered  $\bar{\mathbf{U}}$  and a residual velocity  $\mathbf{u}'$ , i.e.

$$\mathbf{U}(\mathbf{x}, t) = \bar{\mathbf{U}}(\mathbf{x}, t) + \mathbf{u}'(\mathbf{x}, t). \quad (3.15)$$

The filtered velocity is obtained as

$$\bar{\mathbf{U}}(\mathbf{x}, t) = \int_{\mathbb{R}^3} G(\mathbf{r}, \mathbf{x}) \mathbf{U}(\mathbf{x} - \mathbf{r}, t) d\mathbf{r}, \quad (3.16)$$

which invokes the integration over the whole computational domain. There are various options for the filtering function; common examples are box-, Gaussian-, sharp spectral- or Cauchy filters. Similar as in the RANS context, it is common in compressible flow formulations to work with Favre decomposed quantities. Here, Favre averages and Favre fluctuations, e.g.

$$\tilde{\mathbf{U}} = \frac{\overline{\rho \mathbf{U}}}{\bar{\rho}} \quad \text{and} \quad \mathbf{U}'' = \mathbf{U} - \tilde{\mathbf{U}}, \quad (3.17)$$

are employed. The Favre filtered momentum equation reads

$$\frac{\partial \bar{\rho} \tilde{U}_j}{\partial t} + \frac{\partial \bar{\rho} \tilde{U}_i \tilde{U}_j}{\partial x_i} = -\frac{\partial \bar{p}}{\partial x_j} + \frac{\partial \tau_{ij}}{\partial x_i} + \frac{\partial T_{ij}}{\partial x_i}, \quad (3.18)$$



where

$$\tau_{ij} = \mu \left( \frac{\partial \tilde{U}_i}{\partial x_j} + \frac{\partial \tilde{U}_j}{\partial x_i} - \frac{2}{3} \frac{\partial \tilde{U}_k}{\partial x_k} \delta_{ij} \right) \quad \text{and} \quad T_{ij} = \bar{\rho} \tilde{U}_i \tilde{U}_j - \widetilde{\bar{\rho} U_i'' U_j''} \quad (3.19)$$

are the viscous stress and the residual stress tensors, respectively. An approach to tackle combustion problems are filtered density function (FDF) methods. There, a transport equation of the composition joint FDF defined by

$$\bar{f}(\Psi; \mathbf{x}, t) = \int_{\mathbb{R}^3} G(\mathbf{r}) \delta(\phi(\mathbf{x} - \mathbf{r}, t) - \Psi) d\mathbf{r}, \quad (3.20)$$

is solved. For reactive flow calculations, the advantage is that the filtered chemical source term can be closed with the information provided by the composition FDF. Molecular mixing is taking place at the subgrid level and must be modeled anyway.

### 3.4 Direct Numerical Simulation

Solving the governing equations numerically with all scales resolved is called direct numerical simulation (DNS). No modeling assumptions have to be made and the accuracy of the solution is determined by the numerical scheme. The limitation is the high computational cost of this method. It scales with  $Re^{11/3}$ . Nevertheless, nowadays DNS simulations provide very valuable insight to different flow phenomena, since data can be extracted from the DNS results, which were or are still not accessible to experimentalists.

## 4 Transported Joint PDF Methods

From now on we focus on transported joint PDF methods for solving the governing equations of turbulent reactive flows. A first introduction and the basic transport equation were already given in section 3.2. There is a close connection between the theoretical solution strategy, the numerical algorithm and the modeling approaches in PDF methods. Therefore, in the first section of this chapter, the strategy to solve PDF transport equations is outlined, in a second step, some important theoretical background is given, which involves the relation between Eulerian and Lagrangian PDF's and the connection of PDF transport equations to stochastic differential equations. Algorithmic approaches like particle stand alone and hybrid methods for solving the governing system are described and the latter approach is elaborated in section 4.3.

### 4.1 Theory of Stochastic Processes

The early initiation of stochastic processes goes back to the discovery of the random motion of suspended particles by R. Brown in 1827, known as Brownian motion. Only at the beginning of the 20th century, Einstein came up with a mathematical description of this phenomenon. From then on, numerous scientists contributed to the development of the stochastic theory. Some of the most famous were Langevin, Chapman, Kolmogorov, Fokker and Planck.

#### 4.1.1 Markov Processes

We start with the consideration of a particle which undergoes a stochastic motion. It is located at  $\mathbf{x}_i$  ( $i = 0, 1, \dots$ ) at time  $t_i$ . If we consider a Markov type process, meaning that  $\mathbf{x}_i$  depends only on the previous position  $\mathbf{x}_{i-1}$  at time  $t_{i-1}$  and is independent of all former time steps  $t_{i-k}$  with  $k > 2$ , then the probability of a particle being at position  $\mathbf{x}_2$  conditioned on its position  $\mathbf{x}_0$  at time  $t_0$  is

$$f(\mathbf{x}_2; t_2 | \mathbf{x}_0, t_0) = \int f(\mathbf{x}_2; t_2 | \mathbf{x}_1, t_1) f(\mathbf{x}_1; t_1 | \mathbf{x}_0, t_0) d\mathbf{x}_1. \quad (4.1)$$

This equation goes back to Chapman and Kolmogorov and is therefore named Chapman - Kolmogorov equation. Gardiner (see [29], sec. 3.4.1) derived a differential form of Eq. (4.1), which is a time evolution equation for conditional PDFs. Different assumptions on the quality of the underlying stochastic process have to be made in order to obtain that

differential equation. They have mainly to do with continuity considerations of the sample paths. This leads to the following conditions, which must hold for any  $\epsilon > 0$ :

- a) 
$$\lim_{\Delta t \rightarrow 0} \frac{f(\mathbf{x}; t + \Delta t | \mathbf{z}, t)}{\Delta t} \Big|_{|\mathbf{x} - \mathbf{z}| \geq \epsilon} = \mathcal{W}(\mathbf{x} | \mathbf{z}, t),$$
- b) 
$$\lim_{\Delta t \rightarrow 0} \frac{1}{\Delta t} \int_{|\mathbf{x} - \mathbf{z}| < \epsilon} (x_i - z_i) f(\mathbf{x}; t + \Delta t | \mathbf{z}, t) d\mathbf{x} = A_i(\mathbf{z}, t) + \mathcal{O}(\epsilon),$$
- c) 
$$\lim_{\Delta t \rightarrow 0} \frac{1}{\Delta t} \int_{|\mathbf{x} - \mathbf{z}| < \epsilon} (x_i - z_i)(x_j - z_j) f(\mathbf{x}; t + \Delta t | \mathbf{z}, t) d\mathbf{x} = B_{ij}(\mathbf{z}, t) + \mathcal{O}(\epsilon),$$
- d) all higher order terms similar as in b) and c) must vanish (see Gardiner [29] sec. 3.4).

In a), b) and c), the conditions for the jump probability  $\mathcal{W}$ , the drift coefficients  $A_i$  and the diffusion coefficients  $B_{ij}$  are given, respectively. Whereas condition d) is implied by the assumption of continuous sample paths. The time evolution equation for the conditional PDF  $f(\mathbf{x}; t | \mathbf{x}_0, t_0)$  is then obtained as

$$\begin{aligned} \frac{\partial f(\mathbf{x}; t | \mathbf{x}_0, t_0)}{\partial t} = & - \frac{\partial}{\partial x_i} [A_i(\mathbf{x}, t) f(\mathbf{x}; t | \mathbf{x}_0, t_0)] \\ & + \frac{1}{2} \frac{\partial^2}{\partial x_i \partial x_j} [B_{ij}(\mathbf{x}, t) f(\mathbf{x}; t | \mathbf{x}_0, t_0)] \\ & + \int [\mathcal{W}(\mathbf{x} | \mathbf{z}, t) f(\mathbf{z}; t | \mathbf{x}_0, t_0) \\ & - \mathcal{W}(\mathbf{z} | \mathbf{x}, t) f(\mathbf{x}; t | \mathbf{x}_0, t_0)] d\mathbf{z}. \end{aligned} \quad (4.2)$$

Two fundamentally different processes can be identified in this equation. The first and second term on the right hand side describe diffusion processes, whereas the third term is a jump process.

First some words about the jump process, which is less important in our case.  $\mathcal{W}(\mathbf{x} | \mathbf{z}, t) dt$  is the transition (or jump) probability of changing the position from  $\mathbf{z}$  to  $\mathbf{x}$  within an infinitesimal time interval  $dt$ . If one would consider a pure jump process then  $A_i$  and  $B_{ij}$  of Eq. (4.2) would be equal to zero and the resulting simplified equation is then called Master equation. Clearly, the sample paths of such a process are not continuous and generally nowhere differentiable.

In the other case of a pure diffusion processes, the following condition must hold

$$\lim_{\Delta t \rightarrow 0} \frac{f(\mathbf{x}; t + \Delta t | \mathbf{z}, t)}{\Delta t} \Big|_{|\mathbf{x} - \mathbf{z}| > \epsilon} = 0. \quad (4.3)$$

Comparing with condition a) (see above), one realizes that all jump probabilities  $\mathcal{W}$  must be zero. The resulting differential equation is the Fokker-Planck or forward Kolmogorov equation

$$\begin{aligned} \frac{\partial f(\mathbf{x}; t | \mathbf{x}_0, t_0)}{\partial t} = & - \frac{\partial}{\partial x_i} [A_i(\mathbf{x}, t) f(\mathbf{x}; t | \mathbf{x}_0, t_0)] \\ & + \frac{1}{2} \frac{\partial^2}{\partial x_i \partial x_j} [B_{ij}(\mathbf{x}, t) f(\mathbf{x}; t | \mathbf{x}_0, t_0)], \end{aligned} \quad (4.4)$$

where  $\mathbf{A}$  denotes the drift vector and  $\underline{\mathbf{B}}$  the diffusion matrix. In the case of a single valued process, these are just scalar valued coefficients. Note that a continuous sample path  $\mathbf{X}(t)$  does not imply that it is everywhere differentiable. Furthermore, if the diffusion matrix (or coefficient) is zero, the Fokker-Planck equation reduces to the so called Liouville equation and describes a deterministic process with a well defined time derivative.

*Remark:* Another insightful derivation of the Fokker-Planck equation is given by Heinz [32]. He starts with a Taylor expansion of the Dirac function representation of the PDF, which results in the Kramers-Moyal equation and finally leads to the Fokker-Planck equation by continuity assumptions.

#### 4.1.2 Diffusion Processes

The most fundamental diffusion process is the Wiener process  $W(t)$ , where the drift coefficient is zero and the diffusion coefficient is unity. In this case the Fokker-Planck equation for a single valued process  $X(t)$  becomes

$$\frac{\partial f(x; t | x_0, t_0)}{\partial t} = \frac{1}{2} \frac{\partial^2 f(x; t | x_0, t_0)}{\partial x^2}. \quad (4.5)$$

It is interesting to look at the stationary distribution, which is found by setting  $\partial f / \partial t = 0$  and solving the remaining homogeneous ordinary differential equation for  $f$ . It results in a Gaussian distribution with mean  $x_0$  and variance  $(t - t_0)$ :

$$f(x; t | x_0, t_0) = \frac{1}{\sqrt{2\pi(t - t_0)}} \exp\left(-\frac{1/2(x - x_0)^2}{t - t_0}\right). \quad (4.6)$$

There are several other interesting properties of the Wiener process, particularly about its increment  $dW(t)$ , which we will meet later in this work.

Until now we investigated stochastic processes in terms of the evolution of their PDFs. Another way is to look at individual realizations of the respective stochastic process. This

is usually done by describing sample paths with the help of stochastic differential equations (SDE). The general form of an SDE is

$$dX(t) = a(X, t)dt + b(X, t)\xi(t)dt \quad (4.7)$$

with  $a(X, t)$  and  $b(X, t)$  being given deterministic functions and  $\xi(t)$  a random term, e.g. a white noise. Such an equation describes the change of a random variable  $X(t)$  in time with a deterministic drift term (first right hand side term in Eq. (4.7)) and a stochastic diffusion term (second term on the right hand side).

In a turbulent flow we are interested in describing the random movement of fluid particles, which intuitively means that the fluid particle paths are continuous. Therefore, as we have seen above, the underlying process must be a diffusion process. A basic and simple diffusion process is the Ornstein-Uhlenbeck (OU) process and is described by the so called Langevin equation

$$dX(t) = -\frac{1}{T}X(t)dt + \left(\frac{2\sigma^2}{T}\right)^{1/2} dW(t). \quad (4.8)$$

The OU process consists of a linear drift coefficient  $a(X, t) = -X/T$  and a constant diffusion coefficient  $b(X, t) = 2\sigma^2/T$ , where  $T$  and  $\sigma$  are a timescale and a variance parameter, respectively.

This equation has been developed by Langevin as a model for Brownian motion and was one of the first SDEs. Later, it was found that it can also be applied for modeling other physical phenomena as for instance turbulent motions.

Since the OU process is a diffusion process, there must exist a corresponding Fokker-Planck equation. Indeed, the OU increment (Eq. (4.8)) can be inserted in conditions b) and c) (see above) to determine drift and diffusion coefficients  $A(x, t)$  and  $B(x, t)$ , which are just scalars for a single valued process and one obtains

$$\frac{\partial}{\partial t}f(x; t|x_0, t_0) = \frac{1}{T}\frac{\partial}{\partial x}(xf(x; t|x_0, t_0)) + \frac{\sigma^2}{T}\frac{\partial^2}{\partial x^2}f(x; t|x_0, t_0). \quad (4.9)$$

Comparing the Langevin Eq. (4.8) and the Fokker-Planck Eq. (4.9), it can be noticed that the drift coefficient is the same, whereas the diffusion coefficient in the Langevin equation appears squared in the Fokker-Planck equation. This observation is generally valid and one has

$$A(x, t) = a(x, t) \quad \text{and} \quad B(x, t) = \frac{b^2(x, t)}{2}. \quad (4.10)$$

Analogous, for a generic vector valued diffusion process with the SDE

$$dX_i(t) = a_i(\mathbf{x}, t)dt + b_{ij}(\mathbf{x}, t)dW_j(t), \quad (4.11)$$

the corresponding Fokker-Planck equation for the conditional PDF  $f(\mathbf{x}; t|\mathbf{x}_0, t_0)$  reads

$$\frac{\partial f}{\partial t} = -\frac{\partial}{\partial x_i}(A_i(\mathbf{x}, t)f) + \frac{1}{2}\frac{\partial^2}{\partial x_i\partial x_j}[B_{ij}(\mathbf{x}, t)f], \quad (4.12)$$

with

$$A_i(\mathbf{x}, t) = a_i(\mathbf{x}, t) \quad \text{and} \quad B_{ij}(\mathbf{x}, t) = b_{ik}(\mathbf{x}, t)b_{jk}(\mathbf{x}, t). \quad (4.13)$$

Note that here  $\mathbf{W}(t)$  is a vector valued Wiener process defined as

$$\mathbf{W}(t) = [W_1(t), W_2(t), \dots, W_n(t)]^T. \quad (4.14)$$

A special field in calculus is the treatment of stochastic differential equations. Due to the non-differentiability of the stochastic noise term (e.g. the Wiener process has inherently non-differentiable sample paths), terms like  $dW(t)/dt$  are not defined in normal calculus. Itô and Stratonovich developed two different theories for stochastic calculus. In section 6 we will learn in more detail how SDEs can be treated.

## 4.2 Solution Strategy for PDF Transport Equations

After the short excursion into the basics of stochastic processes, we return to the scenario of turbulent flows. As already introduced in section 3.2, the goal is to find a solution method for the governing Navier-Stokes equations with a fully statistical approach. In such methods, the real flow field is represented in a statistical way, meaning, if the Eulerian one-point velocity-composition joint PDF of the real flow is denoted as  $f(\mathbf{V}, \Psi; \mathbf{x}, t)$  and the calculated one as  $f^*(\mathbf{V}, \Psi; \mathbf{x}, t)$ , one requires that

$$f^*(\mathbf{V}, \Psi; \mathbf{x}, t) = f(\mathbf{V}, \Psi; \mathbf{x}, t). \quad (4.15)$$

Note that this is a much weaker requirement than to demand for instance that the simulated velocity must be equal to the real velocity at each point in time and space, i.e.

$$\mathbf{U}^*(\mathbf{X}, t) = \mathbf{U}(\mathbf{X}, t). \quad (4.16)$$

Thus, in other words, the calculated fluid system must be statistically equivalent to the real flow (see Pope [63] section 4.1).

The basic idea of the approach here is to derive a transport equation for a joint PDF (e.g. Eq. (3.13)), introducing the physics by replacing the corresponding terms with conservation laws and finding appropriate models for the unclosed terms.

Solving the PDF transport equation numerically with standard methods as for instance finite volume or finite element schemes is infeasible in real world problems due to the high dimensionality of the joint PDF. For instance the velocity-composition joint PDF has a dimensionality of  $(7 + N_s)$ ; three spatial, three velocity and  $N_s$  composition coordinates plus time. The computational cost of the classical methods increases approximately with the power of the number of dimensions. Instead, particle Monte Carlo methods can be applied, where the computational effort increases only linearly with the number of sample space dimensions.

Using such a method means that we have to construct a model particle system which is

stochastically equivalent to the real fluid system. There are different approaches how such a modeled particle system can be devised. One way is to derive a PDF transport equation for the desired joint PDF by standard methods, starting from conservation laws as described by Pope [63] and [66] or Fox [27]. Subsequently, stochastic differential equations for model particles can be obtained, which consistently emulate the real fluid system (references same as above).

Another approach is to start from the stochastic process theory by first stating the modeled stochastic particle evolution equations, from which one can derive the corresponding PDF transport equation, and then making the SDEs consistent with the modeled governing conservation laws.

Note that in subsection 4.2.2 we will follow the latter approach. An important topic in this context is the relation between Eulerian and Lagrangian reference systems. That is because often an Eulerian viewpoint is adopted to describe the flow field but here Lagrangian particles are used to solve the governing equation.

Therefore these two viewpoints are presented and explained in the next subsection, first by means of flow parameters then by means of PDFs.

#### 4.2.1 Eulerian and Lagrangian Systems

As mentioned first the Eulerian and Lagrangian flow variables and their respective representation by PDFs are introduced. Then the basic relationship between Eulerian and Lagrangian PDFs is given and it is explained how the Eulerian PDF can be interpreted as a conditional PDF. Furthermore, the definition of the mass density function (MDF) is derived.

##### Eulerian and Lagrangian Flow Field Description

In the common Eulerian view the density, the velocity and the composition values at a certain point in space and time in the flow field are denoted by  $\rho(\mathbf{X}, t)$ ,  $\mathbf{U}(\mathbf{X}, t)$  and  $\Phi(\mathbf{X}, t)$ , respectively. Their Lagrangian counterparts are defined by

$$\begin{aligned}\rho^+(\mathbf{X}_0, t) &\equiv \rho(\mathbf{X}^+(\mathbf{X}_0, t), t), \\ \mathbf{U}^+(\mathbf{X}_0, t) &\equiv \mathbf{U}(\mathbf{X}^+(\mathbf{X}_0, t), t), \quad \text{and} \\ \Phi^+(\mathbf{X}_0, t) &\equiv \Phi(\mathbf{X}^+(\mathbf{X}_0, t), t),\end{aligned}\tag{4.17}$$

where  $\mathbf{X}_0$  is the particle position at time  $t_0$  and  $\mathbf{X}^+(\mathbf{X}_0, t)$  is the particle position at time  $t$  of a particle, which initially was at position  $\mathbf{X}_0$ . Note that the superscript  $+$  denotes a Lagrangian quantity of the real flow field. Furthermore, it can be shown that the material derivatives of the Eulerian quantities describe the rate of change following a fluid particle:

$$\frac{\partial}{\partial t}\rho^+(\mathbf{X}_0, t) = \frac{D}{Dt}\rho(\mathbf{X}, t) \Big|_{\mathbf{X}=\mathbf{X}^+(\mathbf{X}_0, t)},\tag{4.18}$$

$$\frac{\partial}{\partial t}\mathbf{U}^+(\mathbf{X}_0, t) = \frac{D}{Dt}\mathbf{U}(\mathbf{X}, t) \Big|_{\mathbf{X}=\mathbf{X}^+(\mathbf{X}_0, t)}, \quad \text{and}\tag{4.19}$$

$$\frac{\partial}{\partial t}\Phi^+(\mathbf{X}_0, t) = \frac{D}{Dt}\Phi(\mathbf{X}, t) \Big|_{\mathbf{X}=\mathbf{X}^+(\mathbf{X}_0, t)}.\tag{4.20}$$

In the same way, an Eulerian and a Lagrangian one-point joint PDF of the flow variables can be defined. The PDF  $f(\mathbf{V}, \Psi; \mathbf{x}, t)$  is the statistical representation of the Eulerian field at location  $\mathbf{x}$  and time  $t$  (here  $\mathbf{x}$  denotes the sample space variable of the position  $\mathbf{X}$ ). The Lagrangian counterpart is the conditional PDF  $f_L(\mathbf{V}, \Psi, \mathbf{x}; t | \mathbf{V}_0, \Psi_0, \mathbf{x}_0)$  and can be understood as the PDF of fluid particles at time  $t$ , which originate from the initial state  $\mathbf{V}_0$ ,  $\Psi_0$  and  $\mathbf{x}_0$  at  $t_0$ . Another interpretation of a Lagrangian PDF is as a so called transition PDF, which describes the transition probability from a certain state (here the state at time  $t_0$ ) to another state later in time.



### Relations between Eulerian and Lagrangian PDFs

The Eulerian PDF  $f(\mathbf{V}, \Psi; \mathbf{x}, t)$ , which is a function of space and time, can also be interpreted as a conditional PDF  $f(\mathbf{V}, \Psi | \mathbf{x}, t)$ . Intuitively explained, the conditional PDF is the PDF of  $\mathbf{V}$  and  $\Psi$  generated by all particles which are at  $(\mathbf{x}, t)$ , where a particle can be also understood as one realization of the stochastic process with PDF  $f(\mathbf{V}, \Psi)$ . That the consistency between the Lagrangian particle system and the Eulerian system is ensured, this PDF must coincide with the Eulerian PDF at the same location and time (see also Fox [27], section 6.7.4), i.e.

$$f(\mathbf{V}, \Psi; \mathbf{x}, t) \equiv f(\mathbf{V}, \Psi | \mathbf{x}, t). \quad (4.21)$$

This condition gives the starting point to relate a Lagrangian with an Eulerian PDF, which is shown in the following derivation

$$\begin{aligned} f(\mathbf{V}, \Psi; \mathbf{x}, t) &= \frac{f(\mathbf{V}, \Psi, \mathbf{x}; t)}{f(\mathbf{x}; t)} \\ &= \frac{1}{f(\mathbf{x}; t)} \iiint f(\mathbf{V}, \Psi, \mathbf{x}, \mathbf{V}_0, \Psi_0, \mathbf{x}_0; t) d\mathbf{V}_0 d\Psi_0 d\mathbf{x}_0 \\ &= \frac{1}{f(\mathbf{x}; t)} \iiint f_L(\mathbf{V}, \Psi, \mathbf{x}; t | \mathbf{V}_0, \Psi_0, \mathbf{x}_0) \times \\ &\quad f(\mathbf{V}_0, \Psi_0, \mathbf{x}_0; t_0) d\mathbf{V}_0 d\Psi_0 d\mathbf{x}_0. \end{aligned} \quad (4.22)$$

In the first manipulation step, Eq. (4.21) and Bayes theorem for conditional PDFs is applied. The joint PDF  $f(\mathbf{V}, \Psi, \mathbf{x}; t)$  is in a second step expanded by its initial state and for consistency reasons, integrated over the initial state. Finally, again Bayes theorem is used to obtain the last expression. Thus, the Eulerian PDF at any location  $\mathbf{x}$  and time  $t$  can be calculated by integrating the product of the initial state PDF and the Lagrangian PDF over the initial sample space and dividing by the particle distribution PDF. Note that in this equation the interpretation of  $f_L$  as a transition probability becomes obvious, since with its help one can calculate the PDF of a particle at time  $t$  from the PDF of the initial particle state at  $t_0$ .

Next, the conditional PDF is analyzed and this is done best with the help of the so called fine grained PDF (Pope [66], appendix H). The fine grained PDF  $f'(\mathbf{V}, \Psi; \mathbf{x}, t)$  is defined by

$$\begin{aligned} f'(\mathbf{V}, \Psi; \mathbf{x}, t) &\equiv \delta(\mathbf{U}(\mathbf{x}, t) - \mathbf{V}) \delta(\Phi(\mathbf{x}, t) - \Psi) \\ &= \left( \prod_i \delta(U_i(\mathbf{x}, t) - V_i) \right) \left( \prod_\alpha \delta(\phi_\alpha(\mathbf{x}, t) - \Psi_\alpha) \right) \end{aligned} \quad (4.23)$$

and an important property is that the mean of a fine grained PDF is equal to the continuous PDF, i.e.

$$f(\mathbf{V}, \Psi; \mathbf{x}, t) = \langle \delta(\mathbf{U}(\mathbf{x}, t) - \mathbf{V}) \delta(\Phi(\mathbf{x}, t) - \Psi) \rangle. \quad (4.24)$$

Fine grained PDFs can also be understood as discrete realizations of the flow and consequently, the mean of many single realizations results in the continuous PDF. Using Bayes theorem, we can write the conditional PDF as

$$\begin{aligned} f(\mathbf{V}, \Psi | \mathbf{x}, t) &= \frac{f(\mathbf{V}, \Psi, \mathbf{x}; t)}{f(\mathbf{x}, t)} \\ &= \frac{\langle \delta(\mathbf{U}(\mathbf{x}, t) - \mathbf{V}) \delta(\Phi(\mathbf{x}, t) - \Psi) \delta(\mathbf{X}(t) - \mathbf{x}) \rangle}{\langle \delta(\mathbf{X}(t) - \mathbf{x}) \rangle} \end{aligned} \quad (4.25)$$

and expanding the right hand side term on the second line with the total mass  $M$  contained in the flow domain results in

$$f(\mathbf{V}, \Psi | \mathbf{x}, t) = \frac{\langle \delta(\mathbf{U}(\mathbf{x}, t) - \mathbf{V}) \delta(\Phi(\mathbf{x}, t) - \Psi) M \delta(\mathbf{X}(t) - \mathbf{x}) \rangle}{\langle M \delta(\mathbf{X}(t) - \mathbf{x}) \rangle}. \quad (4.26)$$

The expression  $M \delta(\mathbf{X}(t) - \mathbf{x})$  can be identified as the instantaneous mass density at location  $\mathbf{x}$  and consequently the conditional PDF is a density weighted or Favre averaged quantity. The ensemble mean  $\langle M \delta(\mathbf{X}(t) - \mathbf{x}) \rangle$  is then the mean fluid density  $\langle \rho(\phi(\mathbf{x}, t)) \rangle$  (see Heinz [32], section 4.1.1 and 4.1.2).

The considerations above can be used to derive the definition of the MDF  $\mathcal{F}(\mathbf{V}, \Psi, \mathbf{x}; t)$ . Let us start with the joint PDF  $f(\mathbf{V}, \Psi, \mathbf{x}; t)$  and apply Bayes theorem

$$f(\mathbf{V}, \Psi, \mathbf{x}; t) = f(\mathbf{V}, \Psi | \mathbf{x}, t) f(\mathbf{x}; t). \quad (4.27)$$

Multiplying this equation with the total mass  $M$ , the expression  $M f(\mathbf{x}, t)$  appears, which may be written as

$$\begin{aligned} M f(\mathbf{x}, t) &= M \langle \delta(\mathbf{X}(t) - \mathbf{x}) \rangle \\ &= \langle M \delta(\mathbf{X}(t) - \mathbf{x}) \rangle \\ &= \langle \rho(\phi) \rangle. \end{aligned} \quad (4.28)$$

First the definition of fine grained PDFs is used, then the fact that  $M$  is a constant and the last equality is explained in the paragraph above. Now, we are in the position to define the mass density function as follows

$$\mathcal{F}(\mathbf{V}, \Psi, \mathbf{x}; t) \equiv \langle \rho(\phi) \rangle f(\mathbf{V}, \Psi | \mathbf{x}, t). \quad (4.29)$$

It now can easily be verified that the integration of  $\mathcal{F}(\mathbf{V}, \Psi, \mathbf{x}; t)$  over the sample spaces of  $\mathbf{U}$  and  $\Phi$  results in the mean fluid density, i.e.

$$\iint \mathcal{F}(\mathbf{V}, \Psi, \mathbf{x}; t) d\mathbf{V} d\Psi = \langle \rho(\phi) \rangle. \quad (4.30)$$

To work with MDFs instead of PDFs is beneficial for variable density flows because of property (4.30). In the following chapter, we will see that the originally derived PDF transport equation can be manipulated to become an MDF transport equation.

Further considerations and insight into the topic treated in this section can be found in Pope's seminal work of 1985 [63] and also in the books of Fox [27] and Heinz [32].

### 4.2.2 From Modeled SDEs to PDF Transport Equations

To obtain the modeled particle system we start from a general stochastic particle system and derive the corresponding Fokker-Planck equation and show the consistency with the PDF transport equation obtained from the conservation laws. For clarity reason, we first consider simple particle equations and give a physical interpretation of the terms in the Fokker-Planck equation. Then, in a second part, the modeled particle equations and the MDF transport equation are presented.

#### Example Particle System

We consider the particle properties position  $\mathbf{X}^*(t)$ , velocity  $\mathbf{U}^*(t)$  and composition  $\Phi^*(t)$ . Note that the superscript  $*$  indicates a modeled Lagrangian particle quantity. The following assumed system of SDEs describes a possible and reasonable evolution of these particle properties:

$$dX_j^*(t) = U_j^*(t)dt \quad , \quad (4.31)$$

$$dU_j^*(t) = -\frac{1}{T}U_j^*(t)dt + \left(\frac{2\sigma^2}{T}\right)^{1/2} dW_j(t) \quad \text{and} \quad (4.32)$$

$$d\Phi_\alpha^*(t) = C(\phi^*, \langle \phi^* \rangle, t)dt + S_\alpha(\phi^*)dt. \quad (4.33)$$

The rate of change of the particle position is simply the particle velocity (Eq. (4.31)) and the randomness enters only indirectly through the velocity. An Ornstein-Uhlenbeck process (see also section 4.1 on page 19) describes the velocity evolution with the general drift and diffusion coefficients  $1/T$  and  $2\sigma^2/T$ , respectively. We restrict ourself to an isotropic model, hence the coefficients do not depend on the physical direction, but they are functions of time. Note that the model equation for the velocity evolution is in the form of a Langevin equation. Since the composition evolution equation (4.33) has the form of a Louiville equation, a deterministic micro-mixing model is assumed here. The influence of mixing on the compositions is expressed by the general drift term  $C(\phi^*, \langle \phi^* \rangle, t)$  and  $S_\alpha(\phi^*)$  is a source term due to chemical reactions.

Now conditions b) and c) (see section 4.1 on page 17) are employed to determine the drift vector and the diffusion matrix and to finally obtain the Fokker-Planck equation for the modeled conditional Lagrangian joint PDF  $f_L^*(\mathbf{V}, \Psi, \mathbf{x}; t | \mathbf{V}_0, \Psi_0, \mathbf{x}_0)$ :

$$\begin{aligned} \frac{\partial f_L^*}{\partial t} = & -\frac{\partial}{\partial x_i} [\langle U_i^*(t) | \mathbf{V}, \Psi, \mathbf{x} \rangle f_L^*] \\ & + \frac{1}{T} \frac{\partial}{\partial V_i} [\langle U_i^*(t) | \mathbf{V}, \Psi, \mathbf{x} \rangle f_L^*] \\ & - \frac{\partial}{\partial \Psi_\alpha} [(\langle S_\alpha(\phi^*) | \mathbf{V}, \Psi, \mathbf{x} \rangle + \langle C(\phi^*, \langle \phi^* \rangle, t) | \mathbf{V}, \Psi, \mathbf{x} \rangle) f_L^*] \\ & + \frac{1}{2} \frac{\partial^2}{\partial V_i \partial V_i} \left[ \frac{2\sigma^2}{T} f_L^* \right]. \end{aligned} \quad (4.34)$$

The transport equation for the modeled Eulerian PDF  $f^*(\mathbf{V}, \Psi; \mathbf{x}, t)$  can be derived by multiplying Eq. (4.34) with the PDF of the initial state  $f^*(\mathbf{V}_0, \Psi_0, \mathbf{x}_0; t_0)$  and subsequent integration over all initial states. Note that the resulting equation contains the position PDF  $f^*(\mathbf{x}; t)$ . Furthermore, the MDF transport equation is obtained by multiplying the equation for  $f^*(\mathbf{V}, \Psi; \mathbf{x}, t)$  with  $M$  and using Eq. (4.28) and the MDF definition Eq. (4.29). It turns out that the equation is similar to Eq. (4.34), only with  $f_L^*$  replaced by  $\mathcal{F}^*(\mathbf{V}, \Psi, \mathbf{x}; t)$ .

In a next step, the models for the particle behavior have to be refined and appropriate expressions in the PDF or MDF transport equation must be found. At the end of the process, the PDF transport equation derived from the modeled stochastic particle equations must be consistent with the PDF transport equation obtained directly from the conservation laws (see section 3.2). Therefore we take a more detailed look at the different terms in Eq. (4.34) and compare them with the corresponding physical terms in Eq. (3.14). The first term on the right hand side describes the evolution of the PDF in physical space, i.e. the convective transport. The second and the last terms evolve the PDF in velocity space, which includes the effect of the mean and fluctuating pressure and the viscous stress tensor  $\tau_{ij}$ . Responsible for the change in composition space are the terms on the third line of Eq. (4.34). The reaction source term  $S_\alpha$  evolves the PDF due to chemical reactions and the yet unknown function  $C(\phi^*, \langle \phi \rangle, t)$  accounts for the molecular diffusion fluxes  $J^\alpha$ , also called micro-mixing.

Finding consistent and appropriate modeled particle equations is not an easy task and requires more detailed analysis, which is beyond the scope of this work. For further reading it is referred to the textbooks of Pope [66] chapters 12.3 and 12.7.4, Heinz [32] chapter 5 and Fox [27] chapter 6.7.

### Modeled Particle and PDF Equations

One of the simplest velocity model is the Simplified Langevin Model (SLM) (see Pope [66], section 12.3), i.e.

$$dU_j^*(t) = -\frac{1}{\langle \rho \rangle} \frac{\partial \langle p \rangle}{\partial x_j} dt - \left( \frac{1}{2} + \frac{3}{4} C_0 \right) \frac{\tilde{\varepsilon}}{\tilde{k}} \left( U_j^* - \tilde{U}_j \right) dt + (C_0 \varepsilon)^{1/2} dW_j(t). \quad (4.35)$$

The terms from left to right on the right hand side are responsible for the influence of the mean pressure gradient  $\partial \langle p \rangle / \partial x_i$ , the drift of the particle velocity towards the mean fluid velocity at the particle location with the characteristic frequency  $\tilde{\varepsilon} / \tilde{k}$  and diffusion in velocity space. The factor  $3/4 C_0$  in the coefficient  $(1/2 + 3/4 C_0)$  together with the random term (last right hand side term) is responsible for the effect of the fluctuating pressure (velocity redistribution; return to isotropy) and  $C_0$  is a model constant with standard value 2.1 (see Pope [66] pages 487, 504 and 505 for more details). The factor 1/2 ensures the correct decay of turbulent kinetic energy in homogeneous isotropic turbulence. Here, instead of the frequency  $\tilde{\varepsilon} / \tilde{k}$ , the conditional turbulence frequency

$$\Omega \equiv \frac{C_\Omega \langle \rho^* \omega^* | \omega^* \geq \langle \omega \rangle \rangle}{\langle \rho \rangle} \quad (4.36)$$

with the model constant  $C_\Omega$  is employed. The conditional turbulence frequency was introduced by Jayesh et al. [35] for the turbulence frequency model (see further down Eq. (4.38)) to account for intermittency effects in turbulent flows. Note that Eq. (4.35) has the same structure than the diffusion process, i.e. Eq. (4.32).

The evolution equation for the particle composition reads

$$d\phi_\alpha^*(t) = -\frac{1}{2}C_\phi\frac{\tilde{\varepsilon}}{\tilde{k}}\left(\phi_\alpha^* - \tilde{\phi}_\alpha\right)dt + S_\alpha(\phi)dt, \quad (4.37)$$

where the Interaction by Exchange with the Mean (IEM) mixing model by Villermaux and Devillon [76] is applied to mimic the scalar diffusion. The IEM model consists of a linear drift of the scalar value towards its mean at the particle location with the frequency  $\tilde{\varepsilon}/\tilde{k}$ . The model constant  $C_\phi$  describes the ratio of the mechanical to scalar timescale and its standard value is 2.0. However,  $C_\phi$  is not a universal parameter and must be adjusted to each particular application. Finally, the reaction source term  $S_\phi$  usually is a highly nonlinear function of the scalar distribution. Since this distribution is a part of the solution in PDF methods the chemical source term poses no closure problem.

So far, we considered only the particle properties velocity and compositions, now we additionally introduce the turbulence frequency. In the introductory section 3.2 for PDF methods, it is mentioned that a complete model must also include a time scale information in the PDF. Jayesh et al. [35] developed a stochastic process for the turbulence frequency  $\omega^*$  in the form of the Langevin equation

$$d\omega^*(t) = -(\omega^* - \tilde{\omega})C_3\Omega dt - \Omega\omega^*S_\omega dt + (2C_3\sigma^2\tilde{\omega}\Omega\omega^*)^{1/2}dW, \quad (4.38)$$

where  $C_3$  and  $\sigma^2$  are a model constant and the variance of  $\omega^*$ , respectively. The source term  $S_\omega$  of the turbulence frequency is

$$S_\omega = C_{\omega 2} - C_{\omega 1}\frac{\mathcal{P}}{k\Omega}, \quad (4.39)$$

where  $C_{\omega 1}$  and  $C_{\omega 2}$  are further model constants and the turbulence production term  $\mathcal{P}$  is equal to  $-\widetilde{u_i u_j} \partial \widetilde{U}_i / \partial x_j$ . From experiments it is known that in a generic turbulent flows the frequency is approximately Gamma distributed, therefore the stochastic process of Eq. (4.38) ensures a stationary Gamma shaped PDF.

Eqs. (4.31), (4.35), (4.37) and (4.38) form a stochastic system for particle position, velocity, composition and turbulence frequency, which is used to model the behavior of real turbulent reactive flows. Finally, With the same procedure as above, the MDF transport equation

for  $\mathcal{F}(\mathbf{V}, \theta, \Psi, \mathbf{x}; t)$  can be obtained and reads

$$\begin{aligned}
\frac{\partial \mathcal{F}}{\partial t} + \frac{\partial V_i \mathcal{F}}{\partial x_i} - \frac{1}{\langle \rho \rangle} \frac{\partial \langle p \rangle}{\partial x_i} \frac{\partial \mathcal{F}}{\partial V_i} + \frac{\partial}{\partial \Psi_\alpha} [S_\alpha(\Psi) \mathcal{F}] = \\
\frac{\partial}{\partial V_i} \left[ \left( \frac{1}{2} + \frac{3}{4} C_0 \right) \Omega (V_i - \tilde{U}_i) \mathcal{F} \right] \\
+ \frac{\partial}{\partial \theta} [(\theta - \tilde{\omega}) C_3 \Omega + \Omega \theta S_\omega] \mathcal{F} \\
+ \frac{\partial}{\partial \Psi_\alpha} \left[ \frac{1}{2} C_\phi \frac{\varepsilon}{k} (\Psi_\alpha - \tilde{\Phi}_\alpha) \mathcal{F} \right] \\
+ \frac{1}{2} C_0 \varepsilon \frac{\partial^2 \mathcal{F}}{\partial V_i \partial V_i} \\
+ C_3 \sigma^2 \tilde{\omega} \Omega \frac{\partial^2 \theta \mathcal{F}}{\partial \theta \partial \theta}. \tag{4.40}
\end{aligned}$$

All terms on the left hand side (first line) are exact, whereas the right hand side terms are modeled.

### 4.3 Numerical Solution Methods

As explained at the beginning of section 4.2, the appropriate numerical solution approach is a particle based Monte Carlo method. There are different strategies to implement such a method in practice. In a first approach by Pope [62], the particles can only reside at discrete points in physical space and are moved each time step through the whole state space according to the Lagrangian particle equations.

Later, Pope [63] showed that a continuous particle movement in physical space is advantageous and leads to faster convergence. Many calculations were performed with such so called particle stand-alone codes for non-reacting and reacting flow cases by different researchers, as for instance Anand and Pope [2], Delarue and Pope [20], Dreeben and Pope [24], Saxena and Pope [71], van Slooten and Pope [74]. The major drawback of such stand-alone methods is, however, that statistical and deterministic bias errors remain significant, unless a huge number of particles is employed, which makes such PDF simulations very expensive. This difficulty was the motivation for the development of various hybrid algorithms. There, the basic idea consists in reducing statistical and bias errors by treating some averaged flow quantities with a continuum method. In [18], [15], [67], [52], for example, a finite volume scheme is applied to compute the mean velocity, mean pressure, turbulent kinetic energy and dissipation, while a particle method is employed to obtain the composition joint PDF, i.e. the joint distribution of species mass fractions and enthalpy. Note that these hybrid methods depend on classical two equation or Reynolds stress turbulence models for the velocity statistics. Later, hybrid methods for the velocity-composition joint PDF were developed. Fully consistent hybrid algorithms were devised by Jenny et al. [36] and Muradoglu et al. [49], where additionally a time scale information is contained in the PDF and therefore no additional model equations are needed. In this thesis we follow

those consistent hybrid approaches to solve for the velocity-frequency-composition joint MDF  $\mathcal{F}(\mathbf{V}, \theta, \Psi, \mathbf{x}; t)$ .

The next subsection first explains the hybrid approach and then describes the two main parts of such an algorithm, i.e. on one hand the finite volume (FV) scheme and on the other hand the particle method. Certain consistency conditions between the FV and particle part are essential and have to be fulfilled in order to obtain reliable results.

### 4.3.1 Hybrid Algorithm

As mentioned in the introduction of this chapter, the hybrid methods were developed to reduce statistical and bias errors. In Monte Carlo methods these two errors must be controlled and kept small in order to obtain reliable results. The statistical error can be reduced by time averaging techniques, if statistically stationary scenarios are considered. The main source of the bias error arises from the estimation of means, which are used in the SDEs for the particle evolution. Similarly as the statistical error, it can be diminished by employing time averaged mean quantities in the particle evolution equations, for instance using the time averages of the Favre means  $\tilde{U}_j$ ,  $\tilde{\phi}_\alpha$ ,  $\tilde{\omega}$  and  $\tilde{\Omega}$  in Eqs. (4.35), (4.37), (4.38), respectively. However, in order to reduce these two errors to an acceptable level, a calculation must continue for a long time in the statistically stationary state. For a more detailed analysis about error estimation in PDF algorithms see Xu et al. [81].

The idea of the hybrid approach is to circumvent the calculation of means from particle properties and instead solving the RANS equation with a finite volume scheme. Unclosed terms like the Reynolds stresses, mean energy source term and other turbulence statistics are obtained from a particle method. Vice versa, the particle method, which is used to solve the joint PDF of fluctuating velocity, turbulence frequency and compositions, requires the Favre averaged velocity field from the finite volume scheme. See Fig. 1 for a simplified schematic of a hybrid algorithm. The two main parts of the hybrid code, the finite volume and the particle Monte Carlo part are briefly explained next, and some algorithmic issues and their solutions are addressed.

#### Finite Volume Scheme

A finite volume scheme is applied for solving the RANS equation and the mean energy equation. In reactive flows the mean energy equation is used instead of a Poisson equation for the mean pressure. The mean equations can consistently be derived from the PDF or MDF transport equation, for instance by integrating Eq. (4.40) over the whole sample space, i.e. velocity-frequency-composition space, the mean mass continuity equation is recovered:

$$\frac{\partial \langle \rho \rangle}{\partial t} + \frac{\partial \langle \rho \rangle \tilde{U}_i}{\partial x_i} = 0. \quad (4.41)$$

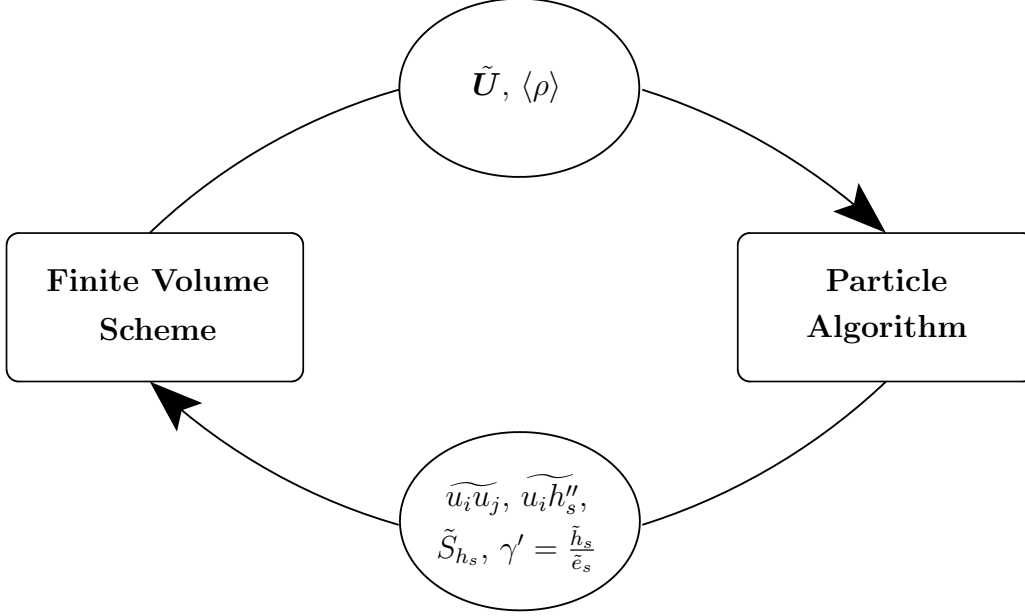


Figure 1: Data exchange in a hybrid finite volume - particle Monte Carlo algorithm for solving the PDF transport equation.

Multiplying Eq. (4.40) with the velocity sample space variable  $V_j$  and subsequently integrating over the state space results in the mean momentum equation, which reads

$$\frac{\partial \langle \rho \rangle \tilde{U}_j}{\partial t} + \frac{\partial \langle \rho \rangle \tilde{U}_j \tilde{U}_i}{\partial x_i} = - \frac{\partial \langle p \rangle}{\partial x_j} - \frac{\partial \langle \rho \rangle \widetilde{u_j u_i}}{\partial x_i}. \quad (4.42)$$

Similarly, the mean energy equation for the total energy  $E_s$  (see Eq. (2.14)) is obtained by multiplying Eq. (4.40) with the sensible enthalpy  $h_s$  (note that the enthalpy is an element of the composition vector) and consecutively integrating over the state space. Different assumptions and simplifications can be made during this derivation since only statistical stationary, high Reynolds-, low Mach number flows are considered. Therefore, the arising term  $D\langle p \rangle/Dt$  is negligible due to the fact that it scales with  $Ma^2$ . Furthermore, dimensional analysis shows that the turbulent energy production is much smaller than the chemical source term and also the turbulent kinetic energy can be neglected, i.e.

$$\widetilde{u_i u_i} \ll \tilde{U}_i \tilde{U}_i. \quad (4.43)$$

Considering these assumptions, the energy equation reads

$$\frac{\partial \langle \rho \rangle \tilde{E}_s}{\partial t} + \frac{\partial}{\partial x_i} \left[ \tilde{U}_i \left( \langle \rho \rangle \tilde{E}_s + \langle p \rangle \right) \right] = \langle \rho \rangle \tilde{S}_{h_s} - \frac{\partial \langle \rho \rangle \widetilde{u_i h_s''}}{\partial x_i} - \frac{\partial}{\partial x_i} \left[ \frac{\langle \rho \rangle}{2} \widetilde{u_i u_j u_j} \right]. \quad (4.44)$$



One additional equation is needed to relate the thermodynamic pressure to the density and the energy. For that we use the ideal gas law, i.e.

$$\langle p \rangle = (\gamma' - 1) (\langle \rho \rangle \tilde{E}_s - \frac{1}{2} \langle \rho \rangle \tilde{U}_i \tilde{U}_i). \quad (4.45)$$

Note that this assumptions, as it will be explained later, allows only for open flame or so called deflagration calculations. Eqs. (4.41), (4.42), (4.44) and (4.45) form the system of mean equations solved by the finite volume scheme. The unclosed turbulent quantities and the chemical source term are provided by the particle Monte Carlo part of the solution algorithm.

### Monte Carlo Particle System

Since the mean hydrodynamic equations are solved by the finite volume scheme, only the fluctuating part of the velocity has to be considered in the particle part. Hence, instead of solving the MDF transport equation of velocity, turbulence frequency and compositions, we employ the MDF  $\mathcal{F}(\mathbf{u}, \theta_j, \Psi, \mathbf{x}; t)$  of fluctuating velocity, turbulence frequency and compositions, where  $\mathbf{v} = \mathbf{V} - \tilde{\mathbf{V}}$  is the sample space variable of the Favre fluctuating velocity  $\mathbf{u}$ . If this modified MDF is used, the modeled particle equation for the velocity evolution has to be modified as well. Therefore, Eq. (4.35) is manipulated to obtain the Simplified Langevin equation for the fluctuating velocity as

$$\begin{aligned} du_j^*(t) = & -\frac{1}{\langle \rho \rangle} \frac{\partial \langle \rho \rangle \widetilde{u_i u_j}}{\partial x_j} dt - u_i^* \frac{\partial \tilde{U}_j}{\partial x_i} dt - \left( \frac{1}{2} + \frac{3}{4} C_0 \right) \Omega u_j^*(t) dt \\ & + (C_0 k \Omega)^{1/2} dW_j(t). \end{aligned} \quad (4.46)$$

The particle evolution equations for position  $\mathbf{X}^*$ , composition  $\phi^*$  (including enthalpy  $h_s^*$ ) and turbulence frequency  $\omega^*$  are specified in section 4.2.2 by Eqs. (4.31), (4.37) and (4.38), respectively.

A further important particle property is the particle mass  $m^*$ . It is assigned at the inflow boundary and remains constant (except if particle number control algorithms are employed). A particle represents a certain amount of fluid mass and therefore the particle number density (PND) or as we have seen earlier the particle position PDF  $f(\mathbf{x}, t)$  determines the so called fluid particle density.

Various statistical moments have to be extracted from the particle ensemble. On one hand to close the RANS and particle evolution equations and on the other hand to compare flow or thermodynamic properties with experiments or other calculations. Reynolds stresses  $\widetilde{u_i u_j}$ , enthalpy fluxes  $u_i h_s''$  and the mean chemical energy source term  $\tilde{S}_{h_s}$  are required in the RANS equations. For the particle equations the Reynolds stresses  $\widetilde{u_i u_j}$ , the conditional mean turbulence frequency  $\Omega$ , the mean turbulent kinetic energy  $\tilde{k}$  and the mean composition vector  $\tilde{\phi}$  are used (see Eqs. (4.37), (4.38) and (4.46)). For the extraction of statistical data, the computational domain is divided into bins in order to sample the particle properties. For that it is natural to use the grid of the finite volume solver. The data can be extracted either cell centered or node based. For a cell center value, a top hat function  $\hat{g}_{l,k}(\mathbf{x})$  is applied, which is 1 for  $\mathbf{x}$  in cell  $(l, k)$  and 0 otherwise. A bi-linear basis function

$\hat{g}_{l,k}(\mathbf{x})$  (in the 2-dimensional case; tri-linear in 3D) is applied for the node based extraction. This function is 1 at the node location and drops down to zero at the edge of the four surrounding cells. Further, the particle mass is used as a weight factor for the statistics. This is intuitively evident, since a heavier particle represents a larger amount of fluid than a lighter one and therefore contributes more to the extracted statistics. The cell centered and node based Favre average of a fictive particle property  $q^*$  is then approximated by

$$\tilde{q}_{l,k}^* \approx \frac{\sum_{n=1}^{N_p} (g_{l,k}(\mathbf{X}^*) m^* q^*)_n}{\sum_{n=1}^{N_p} (g_{l,k}(\mathbf{X}^*) m^*)_n} \quad \text{with} \quad \begin{cases} g_{l,k}(\mathbf{X}^*) = \hat{g}_{l,k}(\mathbf{X}^*) & \text{cell centered} \\ g_{l,k}(\mathbf{X}^*) = \hat{g}_{l,k}(\mathbf{X}^*) & \text{node based,} \end{cases} \quad (4.47)$$

where  $N_p$  is the total number of particles in cell  $(l, k)$ . Note that the sum of all the basis functions  $\hat{g}$  or  $\hat{g}$  must be one at each location. In Pope [66] section 12.6.1 one can find more information about the correspondence between flow quantities of the real and the particle system. Furthermore, gradients of the mean velocity field as used in the particle velocity Eq. (4.46) can be calculated directly from the output of the finite volume scheme.

### Consistency Conditions

On the level of the governing equations, the hybrid algorithm is completely consistent since all equations can be derived from one PDF transport equation. However, due to numerical inaccuracies during computations and the redundant evaluation of certain flow quantities, this consistency may not be fulfilled anymore. Muradoglu et al. [51] showed that three independent conditions have to be satisfied for achieving overall consistency on the numerical level. If the calculated finite volume quantities are denoted by superscript FV, extracted particle data by superscript P and a value in cell  $(l, k)$  by the subscripts  $l, k$ , then the three consistency conditions are

$$\langle \rho \rangle_{l,k}^{\text{FV}} = \langle \rho \rangle_{l,k}^{\text{P}} = \frac{M_{l,k}^{\text{P}}}{V_{l,k}}, \quad (4.48)$$

$$(\tilde{e}_s)_{l,k}^{\text{FV}} = (\tilde{e}_s)_{l,k}^{\text{P}} \quad \text{and} \quad (4.49)$$

$$(\tilde{\mathbf{u}})_{l,k}^{\text{P}} = 0. \quad (4.50)$$

The first condition requires that the mean finite volume density is equal to the particle density, whereas  $M_{l,k}^{\text{P}}$  is the total amount of particle mass in cell  $(l, k)$  and  $V_{l,k}$  the cell volume. Condition (4.49) states the energy consistency between the energy calculated by Eq. (4.44) and the extracted particle energy field  $\tilde{e}_s^{\text{P}}$ . Finally, the last constraint demands that the mean of the fluctuating velocity in each cell becomes zero. The first two conditions concern the consistency between the two basic parts of the algorithm, while the last condition solely is an issue on the particle side. To ensure these consistencies, correction schemes have to be applied. For the density consistency a so called position correction algorithm is normally used, where the particle distribution in physical space is adjusted such that the particle density  $\langle \rho \rangle^{\text{P}}$  matches the FV density  $\langle \rho \rangle^{\text{FV}}$  (see for instance Muradoglu et al. [51] section 4.2). A simple particle velocity correction scheme is suggested by Jenny et al. [36] in order to fulfill Eq. (4.50).

A complete, comprehensive and recent review work which overlooks the subject of chapter 4 with much more details and references to original works can be found in the paper by Haworth [30].

After this explanations on the theory of joint PDF methods and numerical solution algorithm we are going to address some algorithmic issues of hybrid finite volume-particle Monte Carlo methods.

## 5 Efficient Energy Consistency Scheme

As introduced at the end of the previous chapter, the consistency issues arise due to calculation errors and due to the fact that some flow and fluid properties fields are computed redundant in the finite volume and the particle Monte Carlo part of the hybrid algorithm. In the context of turbulent reactive flow calculations the energy consistency issue (condition (4.49)) is obviously very crucial.

The dominating phenomenon altering the sensible energy of the fluid are chemical reactions. In the algorithm, the influence of the chemical reactions acts directly on each particle (as it is apparent in Eq. (4.37)) and updates their energy and compositions. Then, the mean energy source term  $\tilde{S}_{h_s}$  is extracted from the particles and is used for the finite volume solution of the mean energy equation (4.44). Therefore, it is a natural choice to identify the particle energy  $\tilde{e}_s^P$  as the primary energy field.

In order to make the finite volume field consistent with the particle field, Muradoglu et al. [51] proposed a correction scheme, which relaxes the finite volume energy towards the particle energy field by introducing correction terms in the mean energy equation. Here, a new approach is presented, where under certain assumptions the energy consistency issue can be eliminated by neglecting the mean energy equation of the finite volume scheme completely.

### 5.1 Idea, Assumptions and Constraints

The new idea is to use the mean particle energy field, which can be extracted from the particles, directly as the energy information in the finite volume code. Hence, instead of solving the mean energy equation by a finite volume method, the energy equation is solved only by the particle Monte Carlo algorithm. In section 4.3.1 the mean energy equation for the total energy  $\tilde{E}_s$  was derived from the MDF transport equation (4.40). During these manipulations the simplified transport equation for the mean sensible enthalpy  $\tilde{h}_s$

$$\frac{\partial \langle \rho \rangle \tilde{h}_s}{\partial t} + \frac{\partial \langle \rho \rangle \tilde{U}_i \tilde{h}_s}{\partial x_i} = \langle \rho \rangle \tilde{S}_h - \frac{\partial \langle \rho \rangle \widetilde{u_i h_s''}}{\partial x_i} \quad (5.1)$$

was obtained as an intermediate result (not shown). Thus, Eq. (5.1) and Eq. (4.44) are consistent under certain constraints. Therefore a modified Euler system is defined, where Eq. (4.44) can be replaced by Eq. (5.1). The characteristic behavior of this modified system is somewhat different and has to be analyzed in order to show its validity.

The following assumptions and constraints are made in order to obtain a consistent scheme:

- Low Mach number flow ( $Ma < 0.3$ )
- High Reynolds number flow

- Statistical stationary solutions
- Open flames
- Deflagrations, i.e.  $s_F \ll c_{\text{fresh}}$

The first two constraints are flow related. Only low Mach number flows where neither strong shocks nor compressibility effects play a role are considered. The high Reynolds number assumption was already made earlier (viscous effects neglected in the Navier-Stokes equation, which then become the Euler equation). This helps us later to omit some pressure effects. The third constraint is implied by the solution algorithm, where a time averaging technique is employed to reduce the statistical and bias error with a justifiable computational effort. Again, as we will see below, this constraint helps in neglecting certain pressure effects. Open flames (point 4) have the property that the ambient pressure is imposed and therefore the thermodynamic pressure is uniform throughout the flame. Finally, only so called deflagrations are considered. These are combustions where the flame propagation speed is much smaller than the sound speed in the fresh gas.

A very basic and important implication of the above constraints and assumptions can already be drawn; that is that relative pressure changes in our calculations are very small and therefore negligible.

## 5.2 Modified Euler System

First we start with the Euler system, which describes the evolution of a compressible inviscid fluid. The Favre averaged Euler system formed by Eqs. (4.41), (4.42) and (4.44) reads as

$$\frac{\partial \mathbf{w}}{\partial t} + \frac{\partial \mathbf{F}_x(\mathbf{w})}{\partial x} + \frac{\partial \mathbf{F}_y(\mathbf{w})}{\partial y} = \mathbf{R}, \quad (5.2)$$

where  $\mathbf{w}$  is the vector of conserved variables

$$\mathbf{w} = \begin{pmatrix} w_1 \\ w_2 \\ w_3 \\ w_4 \end{pmatrix} = \begin{pmatrix} \langle \rho \rangle \\ \langle \rho \rangle \tilde{U}_1 \\ \langle \rho \rangle \tilde{U}_2 \\ \langle \rho \rangle \tilde{E}_s \end{pmatrix} \quad (5.3)$$

and

$$\mathbf{F}_x(\mathbf{w}) = \begin{pmatrix} w_2 \\ \frac{w_2^2}{w_1} + \langle p \rangle \\ \frac{w_2 w_3}{w_1} \\ \frac{w_2 w_4}{w_1} + \frac{w_2}{w_1} \langle p \rangle \end{pmatrix} = \begin{pmatrix} \langle \rho \rangle \tilde{U}_1 \\ \langle \rho \rangle \tilde{U}_1^2 + \langle p \rangle \\ \langle \rho \rangle \tilde{U}_1 \tilde{U}_2 \\ \langle \rho \rangle \tilde{U}_1 \tilde{E}_s + \tilde{U}_1 \langle p \rangle \end{pmatrix} \quad (5.4)$$

and

$$\mathbf{F}_y(\mathbf{w}) = \begin{pmatrix} w_3 \\ \frac{w_2 w_3}{w_1} \\ \frac{w_3^2}{w_1} + \langle p \rangle \\ \frac{w_3 w_4}{w_1} + \frac{w_3}{w_1} \langle p \rangle \end{pmatrix} = \begin{pmatrix} \langle \rho \rangle \tilde{U}_2 \\ \langle \rho \rangle \tilde{U}_1 \tilde{U}_2 \\ \langle \rho \rangle \tilde{U}_2^2 + \langle p \rangle \\ \langle \rho \rangle \tilde{U}_2 \tilde{E}_s + \tilde{U}_2 \langle p \rangle \end{pmatrix} \quad (5.5)$$

are the flux vectors in  $x$ - and  $y$ -direction, respectively. Vector  $\mathbf{R}$  contains the right hand side terms of the Euler system and is treated as a source term and reads

$$\mathbf{R} = \begin{pmatrix} 0 \\ -\frac{\partial \langle \rho \rangle \widetilde{u_1 u_1}}{\partial x_1} - \frac{\partial \langle \rho \rangle \widetilde{u_1 u_2}}{\partial x_2} \\ -\frac{\partial \langle \rho \rangle \widetilde{u_2 u_1}}{\partial x_1} - \frac{\partial \langle \rho \rangle \widetilde{u_2 u_2}}{\partial x_2} \\ \langle \rho \rangle \tilde{S}_h - \frac{\partial \langle \rho \rangle \widetilde{u_1 h_s''}}{\partial x_1} - \frac{\partial \langle \rho \rangle \widetilde{u_2 h_s''}}{\partial x_2} \end{pmatrix}. \quad (5.6)$$

Additionally a relation between the pressure, density and energy is needed to close the system. Here the ideal gas law (Eq. (4.45)) is employed.

The energy equation of the Euler system is now manipulated to obtain the following conservation equation for the mean sensible enthalpy  $\tilde{h}_s$ :

$$\begin{aligned} \frac{\partial \langle \rho \rangle \tilde{h}_s}{\partial t} + \frac{\partial \langle \rho \rangle \tilde{U}_i \tilde{h}_s}{\partial x_i} - \frac{\tilde{D} \langle p \rangle}{\tilde{D} t} - \langle \rho \rangle \tilde{S}_h + \frac{\partial \langle \rho \rangle \widetilde{u_j h_s''}}{\partial x_j} = \\ - \frac{1}{2} \left( \frac{\partial \langle \rho \rangle \widetilde{u_i u_i}}{\partial t} + \frac{\partial \langle \rho \rangle \tilde{U}_j \widetilde{u_i u_i}}{\partial x_j} \right) - \langle \rho \rangle \widetilde{u_i u_j} \frac{\partial \tilde{U}_i}{\partial x_j} - \frac{1}{2} \frac{\partial \langle \rho \rangle \widetilde{u_j u_i u_i}}{\partial x_j} \end{aligned} \quad (5.7)$$

A dimensional analysis of the term  $\tilde{D} \langle p \rangle / \tilde{D} t$  (Poinsot and Veynant [60] section 1.2.1) reveals that in statistically stationary high Reynolds number flows it scales with  $\text{Ma}^2$ , where  $\text{Ma}$  is the local Mach number in the fresh fluid. The restriction to steady low Mach number flow was made in the previous section 5.1 and therefore the scaling of the substantial pressure derivative allows us to drop this term. Another interpretation is that the mean pressure along mean fluid particle paths does vary only very slightly in deflagrations.

Considering the evolution equation of the turbulent kinetic energy, i.e.

$$\begin{aligned} \frac{1}{2} \left( \frac{\partial \langle \rho \rangle \widetilde{u_i u_i}}{\partial t} + \frac{\partial \langle \rho \rangle \tilde{U}_j \widetilde{u_i u_i}}{\partial x_j} \right) + \langle \rho \rangle \widetilde{u_i u_j} \frac{\partial \tilde{U}_i}{\partial x_j} + \frac{1}{2} \frac{\partial \langle \rho \rangle \widetilde{u_j u_i u_i}}{\partial x_j} = \\ \left\langle p' \frac{\partial u_i}{\partial x_i} \right\rangle - \frac{\partial \langle u_i p' \rangle}{\partial x_i} - \langle u_i \rangle \frac{\partial \langle p \rangle}{\partial x_i}, \end{aligned} \quad (5.8)$$

we can observe that the right hand side of Eq. (5.7) is equal to the left hand side of this equation. Thus, we can replace these terms by the right hand side of Eq. (5.8), which are from left to right; pressure dilatation, pressure diffusion and pressure work, respectively. All these pressure terms can be omitted in our case, since their influence on the sensible enthalpy evolution is very small in low Mach number and constant pressure flows.

Thus the enthalpy conservation equation in the simplified version reads

$$\frac{\partial \langle \rho \rangle \tilde{h}_s}{\partial t} + \frac{\partial \langle \rho \rangle \tilde{U}_i \tilde{h}_s}{\partial x_i} = \langle \rho \rangle \tilde{S}_h - \frac{\partial \langle \rho \rangle \widetilde{u_j h_s''}}{\partial x_j}. \quad (5.9)$$

This derivation shows the consistency between the averaged energy equations for the total energy and the enthalpy under the assumptions made in the previous subsection. Hence, it is verified that the Lagrangian particle solution algorithm solves the same approximated and simplified energy equation as the finite volume scheme (in the original system).

The modified Euler system is then written as

$$\frac{\partial \hat{\mathbf{w}}}{\partial t} + \frac{\partial \hat{\mathbf{F}}_x(\hat{\mathbf{w}})}{\partial x} + \frac{\partial \hat{\mathbf{F}}_y(\hat{\mathbf{w}})}{\partial y} = \mathbf{R} \quad (5.10)$$

with the new vector of conserved variables  $\hat{\mathbf{w}}$  and the flux vectors  $\hat{\mathbf{F}}_x$  and  $\hat{\mathbf{F}}_y$ :

$$\hat{\mathbf{w}} = \begin{pmatrix} \langle \rho \rangle \\ \langle \rho \rangle \tilde{U}_1 \\ \langle \rho \rangle \tilde{U}_2 \\ \langle \rho \rangle \tilde{h}_s \end{pmatrix}, \quad \hat{\mathbf{F}}_x(\hat{\mathbf{w}}) = \begin{pmatrix} \langle \rho \rangle \tilde{U}_1 \\ \langle \rho \rangle \tilde{U}_1^2 + \langle p \rangle \\ \langle \rho \rangle \tilde{U}_1 \tilde{U}_2 \\ \langle \rho \rangle \tilde{U}_1 \tilde{h}_s \end{pmatrix} \quad \text{and} \quad \hat{\mathbf{F}}_y(\hat{\mathbf{w}}) = \begin{pmatrix} \langle \rho \rangle \tilde{U}_2 \\ \langle \rho \rangle \tilde{U}_1 \tilde{U}_2 \\ \langle \rho \rangle \tilde{U}_2^2 + \langle p \rangle \\ \langle \rho \rangle \tilde{U}_2 \tilde{h}_s \end{pmatrix}. \quad (5.11)$$

Note that the right hand side  $\mathbf{R}$  remains unchanged and is as in Eq. (5.6).

The practical implementation of the new scheme gives rise to the question how the mean energy information of the particles is transferred to the finite volume scheme. Common approaches as e.g. in Muradoglu et al. [49] or Jenny et al. [36] pass over the extracted mean energy source term  $\tilde{S}_h$ . This is not possible in the new algorithm since the energy equation is not solved anymore in the finite volume scheme. We have seen that pressure variations in low Mach number deflagrations can be neglected and therefore the thermodynamic pressure can be assumed constant. Thus, the pressure used in the mean momentum equation (see Eq. (5.11)) is obtained by the ideal gas law

$$\langle p \rangle = \langle \rho \rangle^{\text{FV}} \tilde{h}_s^{\text{P}} (\gamma' - 1) / \gamma', \quad (5.12)$$

where  $\langle \rho \rangle^{\text{FV}}$  is the mean density of the finite volume scheme and  $\tilde{h}_s^{\text{P}}$  the extracted particle enthalpy. In the pseudo transient state of the simulation, which means that the averaged particle energy field has not yet converged,  $\langle p \rangle$  is not constant or in other words  $\langle \rho \rangle^{\text{FV}}$  and  $\tilde{h}_s^{\text{P}}$  are not in equilibrium. In the statistically stationary state the mass and momentum equations will adjust  $\langle \rho \rangle^{\text{FV}}$  such that

$$\langle \rho \rangle^{\text{FV}} \tilde{h}_s^{\text{P}} (\gamma' - 1) / \gamma' = \langle p_{\text{ref}} \rangle = \text{const.}, \quad (5.13)$$

where  $\langle p_{\text{ref}} \rangle$  is the mean ambient pressure imposed by the boundary conditions.

### 5.3 Boundary Conditions

The modified Euler equation, as the original one, is a system of hyperbolic differential equations, where flow and thermodynamic informations are transported along characteristic curves with characteristic velocities. Depending on the flow velocity and the thermodynamical properties of the flow, the absolute characteristic velocities of the system can be negative or positive, which means that information can travel either upstream or downstream. This implies that depending on the flow state some information at the boundaries must be prescribed and some other information is given by the flow state in the computational domain. Of course this also depends on the nature of the boundary, i.e. if it is an inflow or an outflow boundary. A characteristic analysis has to be performed in order to specify the correct boundary quantities.

The fundamental theory of hyperbolic equations and system of equations and their characteristic analysis can be found in the textbook of LeVeque [41].

Usually any two dimensional effects at the boundaries are neglected and the velocity is split up into a parallel and a perpendicular component. Obviously, only the perpendicular velocity component determines the in- or outflow behavior of the boundary characteristics. In the following analysis a boundary in  $y$ -direction is considered and accordingly the perpendicular flux points in  $x$ -direction.

The convection term of the modified Euler system (5.10) can be written using the Jacobian of the flux vector, i.e.

$$\frac{\partial \hat{\mathbf{w}}}{\partial t} + \frac{\partial \hat{\mathbf{F}}_x(\hat{\mathbf{w}})}{\partial \hat{\mathbf{w}}} \frac{\partial \hat{\mathbf{w}}}{\partial x} = R_x. \quad (5.14)$$

The eigenvalues of the flux Jacobian specify the characteristic velocities of the system and small disturbance waves are traveling with these velocities across the flow. The flux Jacobian has the following form

$$\frac{\partial \hat{\mathbf{F}}_x(\hat{\mathbf{w}})}{\partial \hat{\mathbf{w}}} = \begin{bmatrix} 0 & 1 & 0 & 0 \\ -\tilde{U}_1^2 & 2\tilde{U}_1 & 0 & (\gamma' - 1)/\gamma' \\ -\tilde{U}_1\tilde{U}_2 & \tilde{U}_2 & \tilde{U}_1 & 0 \\ -\tilde{U}_1\tilde{h}_s & \tilde{h}_s & 0 & \tilde{U}_1 \end{bmatrix} \quad (5.15)$$

and the eigenvalues arranged from the lowest to the highest value are

$$\hat{\lambda} = \begin{pmatrix} \tilde{U}_1 - \hat{c} \\ \tilde{U}_1 \\ \tilde{U}_1 \\ \tilde{U}_1 + \hat{c} \end{pmatrix}, \quad (5.16)$$

where  $\hat{c} = \sqrt{\langle p \rangle / \langle \rho \rangle}$  is the speed of sound of the modified system. Thus, the characteristic velocities are qualitatively identical to the ones of the classical Euler system, only that the absolute value of the sound speed  $\hat{c}$  differs. We will see later in the discussion section 5.4 that the two systems are quite distinct from a thermodynamical viewpoint.

In practical applications it is easier to work with primitive variables instead of the conserved



quantities. In the case here these are the density  $\langle \rho \rangle$ , the velocities in  $x$ - and  $y$ -direction  $\tilde{U}_1$  and  $\tilde{U}_2$ , respectively, and either enthalpy  $\tilde{h}_s$  or pressure  $\langle p \rangle$ , since density, enthalpy and pressure are related by the ideal gas law and only two of them are independent. The information about these quantities are transported along the characteristics with the respective characteristic speeds.

The informations associated to the velocities  $\hat{\lambda}_p > 0$  are coming from the upstream side or equivalently, the corresponding characteristics point downstream in flow direction. Vice versa, negative characteristic speeds  $\hat{\lambda}_p < 0$  are associated with upstream pointing characteristics and the informations come from the downstream direction (traveling against the flow). Note that here the subscript  $p$  denotes the  $p$ -characteristic with  $p \in \{1, 2, 3, 4\}$ . Since we restricted ourself to subsonic flows, i.e.  $|\tilde{U}_1| < \hat{c}$ , the  $p_1$ -characteristic with velocity  $\tilde{U}_1 - \hat{c}$  always travels upstream while the  $p_4$ -characteristic always travels downstream. If the flux Jacobian is assumed to be constant for a small time period (linearized equations) the characteristic curves become straight lines. Figs. 2(a) and 2(b) illustrate the situation in space-time coordinates for both, inflow and outflow boundaries (here  $\tilde{U}_1 > 0$ ). Hence, at

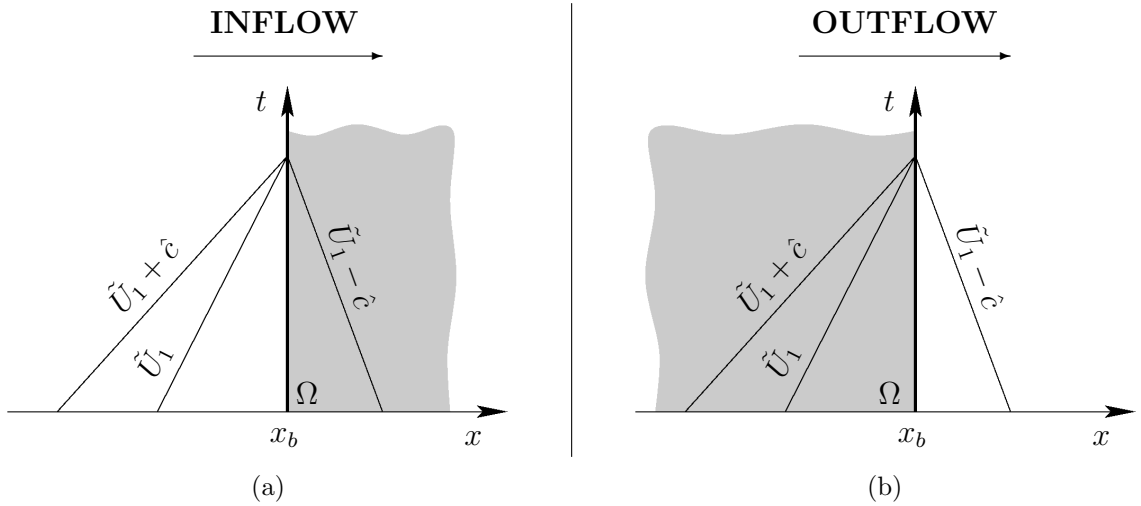


Figure 2: Characteristic inflow (a) and outflow (b) boundary conditions for the modified Euler system with the respective characteristic velocities and for  $\tilde{U}_1 > 0$ . The gray shaded area  $\Omega$  indicates the computational domain and  $x_b$  is the boundary location.

the inflow one boundary information is determined from inside the computational domain and the three other ones must be prescribed. The situation is reversed at the outflow boundary, where one piece of information has to be fixed and the three other ones are taken from the inside.

The question arises which information of the four independent quantities travels in upstream direction. From the theory of hyperbolic conservation laws it is known that the characteristics with velocities  $\tilde{U}_1 \pm \hat{c}$  are acoustic waves, which are small pressure and density disturbances in the flow. For practical applications it is reasonable to prescribe the pressure at the outflow boundaries and enthalpy and velocities at inflow boundaries. In our

case of constant pressure flames, the outflow pressure equals the ambient pressure  $p_{\text{ref}}$  and imposes the pressure level in the whole computational domain. The density of the inflowing fluid is calculated from the ideal gas law using the prescribed enthalpy and the pressure taken from inside the computational domain. Fig. 3 gives an overview of quantities, which

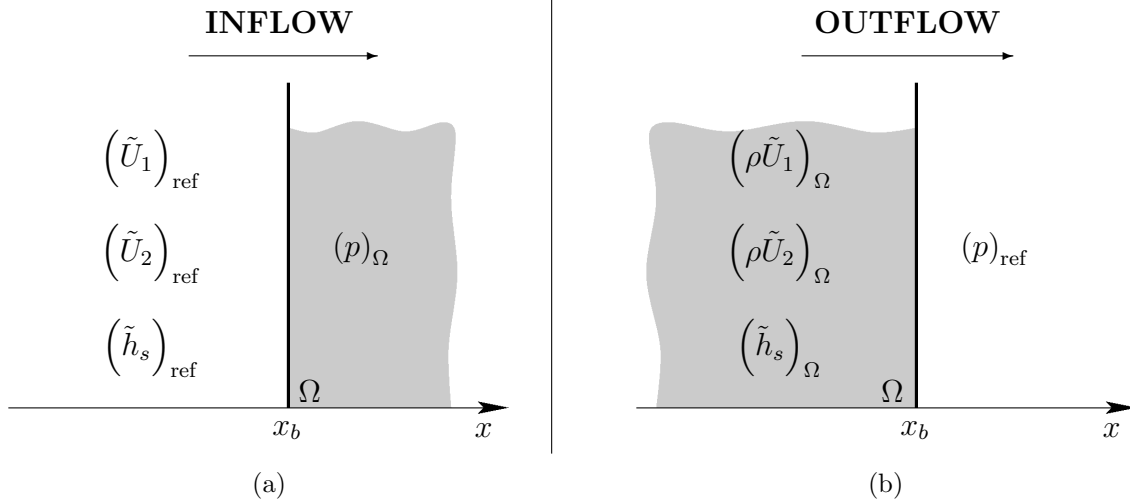


Figure 3: Characteristic boundary condition specification at (a) the inflow and (b) the outflow boundaries. Prescribed reference values are denoted by subscript 'ref' and values taken from inside the computational flow domain by subscript  $\Omega$ . The gray shaded area indicates the computational domain and  $x_b$  the boundary location.

are either prescribed (subscript "ref") or taken from the flow domain (subscript  $\Omega$ ) for both inflow and outflow boundaries. The conservative inflow boundary values, denoted by subscript  $b$ , are then calculated as

$$(\rho)_b = \frac{p_\Omega}{\tilde{h}_{s,\text{ref}}} \left( \frac{\gamma'}{\gamma' - 1} \right) \quad (5.17)$$

$$(\rho \tilde{U}_j)_b = \frac{p_\Omega}{\tilde{h}_{s,\text{ref}}} \left( \frac{\gamma'}{\gamma' - 1} \right) \tilde{U}_{j,\text{ref}} \quad \text{for } j \in \{1, 2\} \quad (5.18)$$

$$(\rho \tilde{h}_s)_b = p_\Omega \left( \frac{\gamma'}{\gamma' - 1} \right) \quad (5.19)$$

and the corresponding outflow quantities as

$$(\rho)_b = \frac{p_{\text{ref}}}{(\tilde{h}_s)_\Omega} \left( \frac{\gamma'}{\gamma' - 1} \right) \quad (5.20)$$

$$(\rho \tilde{U}_j)_b = (\rho \tilde{U}_j)_\Omega \quad \text{for } j \in \{1, 2\} \quad (5.21)$$

$$(\rho \tilde{h}_s)_b = p_{\text{ref}} \left( \frac{\gamma'}{\gamma' - 1} \right). \quad (5.22)$$

It is easy to check that if the pressure in the domain converges towards the reference pressure  $p_{\text{ref}}$  then the inflow density and therefore also the mass and energy fluxes become consistent.

## 5.4 Discussion

The characteristic velocities of the modified system (Eq. (5.16)) are similar to the ones in the common Euler system except for the value of the sound speed. This difference can be explained by an analysis of the two energy equations. If the entropy  $S$  is introduced, the energy equation of the normal Euler system can be manipulated to obtain the following entropy evolution equation (in  $x$ -direction)

$$\frac{\tilde{D}S}{\tilde{D}t} = \frac{\partial S}{\partial t} + \tilde{U}_1 \frac{\partial S}{\partial x} = 0. \quad (5.23)$$

Note that for this analysis we assume a vanishing energy source term. Evidently the entropy is conserved along a Lagrangian fluid particle path. This is also true if a particle crosses a smooth disturbance or even a weak shock. If there are strong shocks (discontinuities), the differential form is no longer valid and one has to work with the integral formulation of the conservation laws. However, here we excluded (see section 5.1) such scenarios. On the other hand, the energy equation in the modified Euler system (see Eq. (5.9)) implies a constant enthalpy (or at least a constant product of density and enthalpy) along particle paths and therefore the resulting speed of sound is the one obtained by a isothermal state change across a pressure disturbance. In reality the state change across a weak shock is isentropic and not isothermal and therefore the modified Euler system involves a "wrong" speed of sound. Pressure and density informations or disturbances are transported with the sound speed. To obtain time accurate results or correct acoustic effects, the speed of sound is of crucial importance but for steady state solutions the propagation velocity with which the disturbances spread has no influence.

A drawback, which has to be mentioned, is of course that a bias error in the averaged enthalpy field is introduced with the new scheme. Originally, the hybrid approach was introduced to avoid such bias errors stemming from particle field extractions. But here the practical experience showed that the tradeoff seems to be worth.

Shortly summarized, a new algorithm circumventing the energy consistency issue in hybrid PDF codes is presented in this chapter. Instead of solving an energy equation redundantly in both the finite volume and the particle Monte Carlo part only the leading energy field of the particle algorithm is used. Through a pseudo-pressure the energy information is transferred from the particle to the finite volume part. With this approach the system of equations solved by the finite volume scheme is modified and instead of the full Euler system we end up with a isothermal system. Calculations of deflagrations under the assumption of statistical stationary, high Reynolds number and low Mach number flow with the new algorithm converge theoretically to the correct physical solution.

## 6 Accurate Time Integration Scheme of SDEs for Joint Statistics

Stochastic differential equations (SDE) are used for modeling various processes in the physical world. Examples are stock market evolution, molecular dynamics or turbulent modeling. SDE's were first introduced by Einstein for the description of Brownian motion in a fluid [26]. Following up, Itô [34] and Stratonovich [72] developed the basic mathematical methods for the treatment of SDEs. Their names stand for the two versions of the stochastic calculus used until nowadays. The integration of SDEs is much more involved than that of ordinary differential equations because of the non-differentiability of the stochastic terms (e.g. Wiener process).

Here we concentrate on a special class of SDEs, i.e. the Langevin equations. The general Langevin equation was already introduced in section 4.1.2 Eq. (4.7). First a short recapitulation why such Langevin equations play a major role in the context of PDF methods. PDF transport equations are defined in a high dimensional space and this makes it inappropriate to solve them with a continuum method as for instance a finite volume scheme; instead particle Monte Carlo methods are employed. In these methods, the notional particles are treated such that the particle ensemble represents the joint PDF of flow and thermodynamical quantities at any point in space and time. Typically the modeled PDF transport equation (see for instance the modeled MDF transport Eq. (4.40)) is a Fokker-Planck equation, which is made consistent with stochastic rules for single fluid particles. These rules have the form of Langevin equations. Examples of such modeled particle equations are the SLM Eq. (4.35) or the Gamma distribution model for the turbulence frequency Eq. (4.38).

The general form of the Langevin equation for the evolution of a vector of stochastic variables  $\mathbf{X}(t)$  is

$$d\mathbf{X}(t) = \mathbf{a}(\mathbf{X}(t), t)dt + \mathbf{b}(\mathbf{X}(t), t)d\mathbf{W}(t), \quad (6.1)$$

with the given coefficients  $\mathbf{a}(\mathbf{X}(t), t)$  and  $\mathbf{b}(\mathbf{X}(t), t)$  and the vector valued Wiener process  $d\mathbf{W}(t)$ . It is important to note that very small timescales can be involved in Eq. (6.1), leading to severe time step restrictions if a common finite differencing scheme [31] is employed for the numerical integration. The goal of this chapter is to develop an integration scheme for such stochastic equations which accurately evolves the joint statistics of the stochastic variables without any time step restriction. This can be achieved by an appropriate construction of the stochastic terms in the evolution equations. The derivation is based on the analytical Itô integration of the equations and on the fact that the Wiener process is Gaussian and the Wiener increments are all independent.

The derivations and ideas follow closely the approach presented by Minier et al. [47]. They developed a first and second order accurate time integration scheme for SDEs used in polydispersed turbulent two - phase flows. This scheme is adapted for our case and the derivation is explained more specifically and more detailed.

Another related approach was presented by Pope [65]. There the Langevin equations for frequency and velocity are transformed and decomposed, such that the stochastic terms become linear. Then the equations are integrated analytically to obtain the numerical scheme. The main difference compared with the approach presented in this work is the consideration of the joint statistics of the different stochastic variables.

## 6.1 Numerical Integration Scheme

In the context of PDF methods for turbulent flows we are especially concerned about the accurate evolution of the particle positions and velocities. Therefore we developed a new integration scheme for the Langevin equations for these two quantities. First, an important result from the Itô calculus is given, which is used later during the derivation of the new approach.

### 6.1.1 Itô Calculus: Important Result

Consider a single valued stochastic process  $U(t)$  described by the Langevin equation

$$dU(t) = -aU(t)dt + b dW(t), \quad (6.2)$$

where the coefficients  $a$  and  $b$  are constant during the time interval from  $t = t_0$  to  $t = t_0 + \Delta t$  (they are evaluated at the beginning of a time step in the sense of Itô). Note that  $a$  and  $b$  are different coefficients from those in Eq. (6.1). The increment of the Wiener process  $dW(t)$  is an independent Gaussian random variable with  $\langle dW(t) \rangle \equiv 0$  (mean) and  $\langle dW(t)^2 \rangle \equiv dt$  (variance). The aim is now to find an analytical expression for  $U(t)$  by integrating Eq. (6.2) from  $t_0$  to  $t_0 + \Delta t$ . The integration yields

$$U(t) = U(t_0)e^{-a\Delta t} + \int_{t_0}^{t_0+\Delta t} b e^{a(s-\Delta t)} dW(s). \quad (6.3)$$

Additionally, for  $\Delta t \rightarrow 0$  there are the following important, albeit unusual, scaling laws in the context of Itô calculus:

- $dt^2 \rightarrow 0$
- $dt dW_j(t) \rightarrow 0$
- $dW_j(t)^2 = \mathcal{O}(dt)$ .

More detailed explanations can be found in Appendix A and for instance in the textbooks of Oksendal [53], Gardiner [29] or Gard [28].

### 6.1.2 Derivations

As mentioned in the introduction of this section we consider a particle system, where each particle has a position  $\mathbf{X}(t)$  and a velocity  $\mathbf{U}(t)$ . Note that in this section the superscript \* for denoting modeled fluid particle properties is omitted for better lucidity. The evolution of these particle properties is described by the following rules:

$$\frac{dX_i(t)}{dt} = U_i(t) \quad \text{and} \quad (6.4)$$

$$\frac{dU_i(t)}{dt} = F_i + \frac{1}{\tau} (\tilde{U}_i - U_i) + \sqrt{\Gamma} \frac{dW_i}{dt}, \quad (6.5)$$

where  $\mathbf{F}$ ,  $\tilde{\mathbf{U}}$ ,  $\tau$  and  $\Gamma$  are a forcing term, mean velocity, a flow time scale and the diffusion coefficient, respectively. For the following derivations, the forcing term  $\mathbf{F}$  and the mean fluid velocity  $\tilde{\mathbf{U}}$  are set to zero for simplicity, but it is straightforward to include these terms. Eq. (6.5) is a simplified Langevin equation for the fluid velocity and the particle position is the time integrated particle velocity. Note, that the randomness of the particle position is caused only by the random term in the velocity equation. Fig. 4 depicts three realizations of the process described by Eq. (6.5) with  $\mathbf{F} = \tilde{\mathbf{U}} = 0$ .

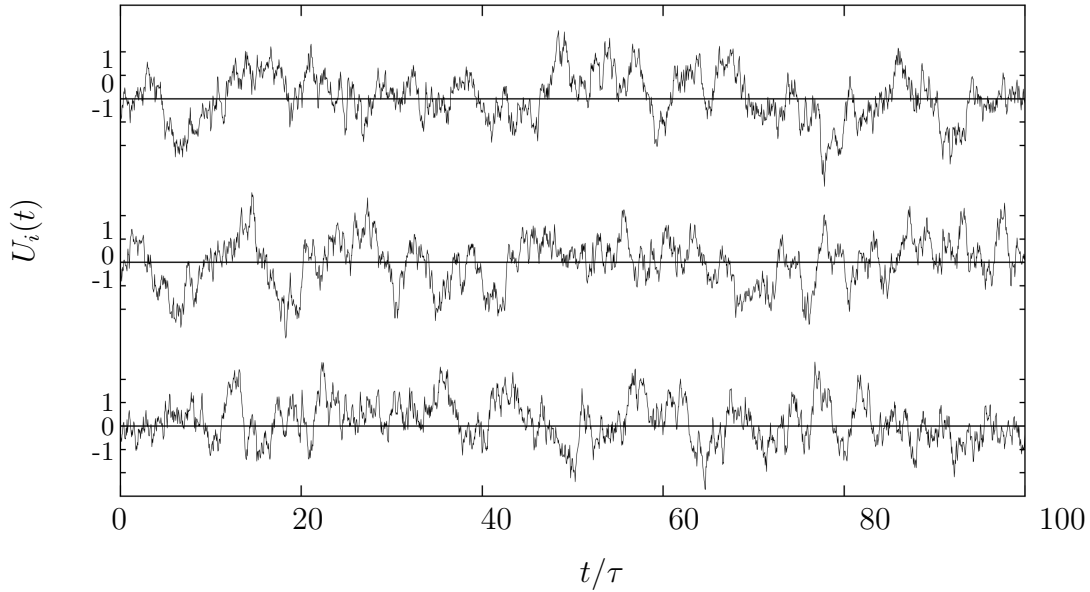


Figure 4: Three sample paths generated by the Langevin Eq. (6.5)

First, the Langevin equation for the velocity  $\mathbf{U}(t)$  is integrated from  $t = t_0$  to  $t = t_0 + \Delta t$  with the result of section 6.1.1 and one obtains

$$U_i(t_0 + \Delta t) = U_i(t_0) e^{-\frac{\Delta t}{\tau}} + \int_{t_0}^{t_0 + \Delta t} \sqrt{\Gamma} e^{\frac{1}{\tau}(s - \Delta t)} dW_i(s). \quad (6.6)$$

The question is now how to treat the integral of the stochastic term. Let us consider a general Riemann-Stieltjes integral of the function  $f(t)$

$$\int_{t_0}^{t_0+\Delta t} f(s)dg(s) = \lim_{N \rightarrow \infty} \sum_{k=0}^{N-1} f(\tau_k) (g(t_{k+1}) - g(t_k)), \quad (6.7)$$

with  $\tau_k$  taken in the interval  $[t_k, t_{k+1}]$  with  $t_k = t_0 + k/N\Delta t$ . For a smooth function  $g(t)$  the sum on the right side converges to the correct value for any  $\tau_k$ . Since here the function  $g(t)$  is the non-continuous Wiener process  $W(t)$ , the choice of  $\tau_k$  determines the value of the integral. We made the decision to work with the rules of Itô, therefore we have to take  $\tau_k = t_k$ . Now the integral in Eq. (6.6) can be written as follows

$$\int_{t_0}^{t_0+\Delta t} \sqrt{\Gamma} e^{\frac{1}{\tau}(s-\Delta t)} dW_i(s) = \lim_{N \rightarrow \infty} \sum_{k=0}^{N-1} \sqrt{\Gamma} e^{-\frac{\Delta t}{\tau}(1-\frac{k}{N})} \Delta W_{i,k}. \quad (6.8)$$

From the properties of the Wiener process it is known that its increments  $\Delta W_{i,k}$  are Gaussian distributed with zero mean and a variance of  $\Delta t/N$ . Therefore the increments can be substituted by

$$\Delta W_{i,k} = \left(\frac{\Delta t}{N}\right)^{1/2} \xi_{i,k}, \quad (6.9)$$

where  $\xi_{i,k}$  are independent normalized Gaussian random variables. Using Eqs. (6.8) and (6.9) in Eq. (6.6) leads to

$$U_i(t_0 + \Delta t) = U_i(t_0) e^{-\frac{\Delta t}{\tau}} + \lim_{N \rightarrow \infty} \sum_{k=0}^{N-1} \sqrt{\Gamma \frac{\Delta t}{N}} \xi_{i,k} e^{-\frac{\Delta t}{\tau}(1-\frac{k}{N})}. \quad (6.10)$$

The same procedure is applied for the position Eq. (6.4) after inserting the result for  $U_i(t)$  to obtain

$$\begin{aligned} X_i(t_0 + \Delta t) = & X_i(t_0) + \tau U(t_0) \left(1 - e^{-\frac{\Delta t}{\tau}}\right) \\ & + \lim_{N \rightarrow \infty} \sum_{k=0}^{N-1} \sqrt{\Gamma \frac{\Delta t}{N}} \xi_{i,k} \tau \left(1 - e^{-\frac{\Delta t}{\tau}(1-\frac{k}{N})}\right). \end{aligned} \quad (6.11)$$

$\xi_{i,k}$  are the same Gaussian random variables as in Eq. (6.10).

To construct a time step independent and accurate integration scheme, we have to evolve position and velocity statistics accurately. Therefore, the following solution scheme is proposed:

$$U_i(t_0 + \Delta t) = U_i(t_0) e^{-\frac{\Delta t}{\tau}} + \sqrt{A} \hat{\xi}_{i,1} + \sqrt{B} \hat{\xi}_{i,2}/quadand \quad (6.12)$$

$$X_i(t_0 + \Delta t) = X_i(t_0) + \tau U_i(t_0) \left(1 - e^{-\frac{\Delta t}{\tau}}\right) + \sqrt{C} \hat{\xi}_{i,1}. \quad (6.13)$$

The split-up of the stochastic term in the velocity equation is necessary to gain an additional degree of freedom for adjusting the joint moment. So the task is to determine  $A$ ,  $B$  and  $C$  such that the following is fulfilled:

- 1) The kinetic energy is preserved.
- 2) The correct velocity autocorrelation  $e^{-t/\tau}$  is recovered.
- 3) The correct first conditional moments  $\langle U_i(t_0 + \Delta t) | \mathbf{U}(t_0) \rangle$  and  $\langle X_i(t_0 + \Delta t) | \mathbf{X}(t_0), \mathbf{U}(t_0) \rangle$  are recovered.
- 4) The correct second conditional moments  $\langle U_i(t_0 + \Delta t)U_j(t_0 + \Delta t) | \mathbf{U}(t_0) \rangle$  and  $\langle X_i(t_0 + \Delta t)X_j(t_0 + \Delta t) | \mathbf{X}(t_0), \mathbf{U}(t_0) \rangle$  are recovered.
- 5) The correct joint moments  $\langle X_i(t_0 + \Delta t)U_j(t_0 + \Delta t) | \mathbf{X}(t_0), \mathbf{U}(t_0) \rangle$  are recovered.

To achieve this, we derive these moments from the exact equations (6.10) and (6.11) as well as from the proposed scheme (Eqs. (6.12) and (6.13)). Then, by comparison, the three coefficients  $A$ ,  $B$  and  $C$  are identified. Note, from now on we denote  $\mathbf{U}(t_0)$  by  $\mathbf{U}^n$  and  $\mathbf{U}(t_0 + \Delta t)$  by  $\mathbf{U}^{n+1}$ . First, we multiply Eq. (6.10) by  $U_j^{n+1}$  and take the conditional average. This leads to

$$\langle U_i^{n+1}U_j^{n+1} | \mathbf{U}^n \rangle = \left\langle \left[ \left( U_i^{n+1} e^{-\frac{\Delta t}{\tau}} + \lim_{N \rightarrow \infty} \sum_{k=0}^{N-1} \sqrt{\Gamma \frac{\Delta t}{N}} \xi_{i,k} e^{-\frac{\Delta t}{\tau} (1 - \frac{k}{N})} \right) \times \right. \right. \\ \left. \left. \left( U_j^{n+1} e^{-\frac{\Delta t}{\tau}} + \lim_{N \rightarrow \infty} \sum_{k=0}^{N-1} \sqrt{\Gamma \frac{\Delta t}{N}} \xi_{j,k} e^{-\frac{\Delta t}{\tau} (1 - \frac{k}{N})} \right) \right] \middle| \mathbf{U}^n \right\rangle. \quad (6.14)$$

If the brackets are expanded and the averaging operator is applied to each term then cross correlations of velocity and random numbers and between random numbers appear. The following rules apply to these moments due to the independence of the random numbers

$$\langle U_i \xi_{j,k} \rangle = 0 \quad \text{and} \quad (6.15)$$

$$\langle \xi_{i,k} \xi_{j,h} \rangle = \delta_{ij} \delta_{kh}. \quad (6.16)$$

Evaluating all terms in Eq. (6.14) results in

$$\langle U_i^{n+1}U_j^{n+1} | \mathbf{U}^n \rangle = \langle U_i^n U_j^n \rangle e^{-\frac{2\Delta t}{\tau}} + \delta_{ij} \lim_{N \rightarrow \infty} \sum_{k=0}^{N-1} \Gamma \frac{\Delta t}{N} e^{-\frac{2\Delta t}{\tau} (1 - \frac{k}{N})}. \quad (6.17)$$

We observe that the last term in Eq. (6.17) contains no random number anymore and can be evaluated as

$$\langle U_i^{n+1}U_j^{n+1} | \mathbf{U}^n \rangle = \langle U_i^n U_j^n \rangle e^{-\frac{2\Delta t}{\tau}} + \delta_{ij} \int_0^{\Delta t} \Gamma e^{-\frac{2t}{\tau}} dt \\ = \langle U_i^n U_j^n \rangle e^{-\frac{2\Delta t}{\tau}} + \delta_{ij} \frac{1}{2} \tau \Gamma \left( 1 - e^{-\frac{2\Delta t}{\tau}} \right). \quad (6.18)$$

From this analytical expression for the evolution of the velocity variance follows that the correct evolution of the velocity  $\mathbf{U}$  can be described by the integration scheme

$$U_i^{n+1} = U_i^n e^{-\frac{\Delta t}{\tau}} + \overbrace{\sqrt{\frac{1}{2} \tau \Gamma \left( 1 - e^{-\frac{2\Delta t}{\tau}} \right)}}^{M_{i,U}} \xi_{i,U}, \quad (6.19)$$



where  $\xi_{i,U}$  is a further independent, normalized Gaussian random variable and the expression  $M_{i,U}$  is used later. Note that with this integration scheme the correct evolution of the mean velocity (i.e.  $\langle U_i^{n+1} | \mathbf{U}^n \rangle = \langle U_i^n \rangle e^{-\frac{\Delta t}{\tau}}$ ) is of course ensured as well.

Similarly from Eq. (6.11) one obtains the evolution equation

$$\begin{aligned} \langle X_i^{n+1} X_j^{n+1} | \mathbf{X}^n, \mathbf{U}^n \rangle &= \langle X_i^n X_j^n \rangle + \tau \left( 1 - e^{-\frac{\Delta t}{\tau}} \right) (\langle X_i^n U_j^n \rangle + \langle X_j^n U_i^n \rangle) \\ &\quad + \tau^2 \langle U_i^n U_j^n \rangle \left( 1 - e^{-\frac{\Delta t}{\tau}} \right)^2 \\ &\quad + \delta_{ij} \Gamma \tau^2 \left( \Delta t - \frac{3}{2} \tau + 2\tau e^{-\frac{\Delta t}{\tau}} - \frac{1}{2} \tau e^{-\frac{2\Delta t}{\tau}} \right) \end{aligned} \quad (6.20)$$

for the particle position variance and subsequent the corresponding evolution for the particle position itself

$$\begin{aligned} X_i^{n+1} &= X_i^n + \tau U_i^n \left( 1 - e^{-\frac{\Delta t}{\tau}} \right) \\ &\quad + \overbrace{\sqrt{\Gamma \tau^2 \left( \Delta t - \frac{3}{2} \tau + 2\tau e^{-\frac{\Delta t}{\tau}} - \frac{1}{2} \tau e^{-\frac{2\Delta t}{\tau}} \right)}}^{M_{i,X}} \xi_{i,X}. \end{aligned} \quad (6.21)$$

To account for the correct correlation between position and velocity, the analytical expression for the covariance is derived by multiplying Eq. (6.10) with Eq. (6.11) and by subsequently taking the conditional average which leads to

$$\begin{aligned} \langle X_i^{n+1} U_j^{n+1} | \mathbf{X}^n, \mathbf{U}^n \rangle &= \langle X_i^n U_j^n \rangle e^{-\frac{\Delta t}{\tau}} + \tau \langle U_i^n U_j^n \rangle \left( e^{-\frac{\Delta t}{\tau}} - e^{-\frac{2\Delta t}{\tau}} \right) \\ &\quad + \delta_{ij} \frac{1}{2} \Gamma \tau^2 \left( 1 - e^{-\frac{\Delta t}{\tau}} \right)^2. \end{aligned} \quad (6.22)$$

The same moments are now calculated from the proposed particle evolution equations (6.12) and (6.13). They read as

$$\langle U_i^{n+1} U_j^{n+1} | \mathbf{U}^n \rangle = \langle U_i^n U_j^n \rangle e^{-\frac{2\Delta t}{\tau}} + \delta_{ij} (A + B), \quad (6.23)$$

$$\begin{aligned} \langle X_i^{n+1} X_j^{n+1} | \mathbf{X}^n, \mathbf{U}^n \rangle &= \langle X_i^n X_j^n \rangle + \tau \left( 1 - e^{-\frac{\Delta t}{\tau}} \right) (\langle X_i^n U_j^n \rangle + \langle X_j^n U_i^n \rangle) \\ &\quad + \tau^2 \langle U_i^n U_j^n \rangle \left( 1 - e^{-\frac{\Delta t}{\tau}} \right)^2 + \delta_{ij} C \quad \text{and} \end{aligned} \quad (6.24)$$

$$\begin{aligned} \langle X_i^{n+1} U_j^{n+1} | \mathbf{X}^n, \mathbf{U}^n \rangle &= \langle X_i^n U_j^n \rangle e^{-\frac{\Delta t}{\tau}} + \tau \langle U_i^n U_j^n \rangle \left( e^{-\frac{\Delta t}{\tau}} - e^{-\frac{2\Delta t}{\tau}} \right) \\ &\quad + \delta_{ij} \sqrt{AC}. \end{aligned} \quad (6.25)$$

Comparing the above moment equations with Eqs. (6.18), (6.20) and (6.22) results in the system

$$A + B = \frac{1}{2} \Gamma \tau \left( 1 - e^{-\frac{2\Delta t}{\tau}} \right) = Q \quad (6.26)$$

$$C = \Gamma \tau^2 \left( \Delta t - \frac{3}{2} \tau + 2\tau e^{-\frac{\Delta t}{\tau}} - \frac{1}{2} \tau e^{-\frac{2\Delta t}{\tau}} \right) = T \quad (6.27)$$

$$\sqrt{AC} = \frac{1}{2} \Gamma \tau^2 \left( 1 - e^{-\frac{\Delta t}{\tau}} \right)^2 = P \quad (6.28)$$

for the unknown coefficients  $A$ ,  $B$  and  $C$ . Solving this system and inserting the result into the proposed scheme (Eqs. (6.12) and (6.13)) leads us to the final integration scheme

$$U_i^{n+1} = U_i^n e^{-\frac{\Delta t}{\tau}} + \overbrace{\sqrt{\frac{P^2}{T}} \hat{\xi}_{i,1} + \sqrt{Q - \frac{P^2}{T}} \hat{\xi}_{i,2}}^{M'_{i,U}} \quad (6.29)$$

$$X_i^{n+1} = X_i^n + \tau U_i^n \left(1 - e^{-\frac{\Delta t}{\tau}}\right) + \underbrace{\sqrt{T} \hat{\xi}_{i,1}}_{M'_{i,X}} \quad (6.30)$$

for the statistically correct particle evolution. Note that the following consistencies are fulfilled

$$\langle M'_{i,U} M'_{j,U} \rangle = \langle M_{i,U} M_{j,U} \rangle = \delta_{ij} Q \quad , \quad (6.31)$$

$$\langle M'_{i,X} M'_{j,X} \rangle = \langle M_{i,X} M_{j,X} \rangle = \delta_{ij} T \quad \text{and} \quad (6.32)$$

$$\langle M'_{i,U} M'_{j,X} \rangle = P. \quad (6.33)$$

Further, it can be shown that the terms  $P^2/T$ ,  $Q - P^2/T$  and  $T$  are all non-negative.

## 6.2 Results

Validation of the new particle integration scheme is done for non-decaying (forced) homogeneous turbulence. First we proof analytically that the new integration scheme recovers the theoretically correct velocity variance (or kinetic energy) evolution and the correct autocorrelation function. The time scale  $\tau$  and the diffusion coefficient  $\Gamma$  are substituted with the corresponding expressions of the SLM (see for instance Eq. (4.46)), which are

$$\tau = \left(\frac{3}{4} C_0 \Omega\right)^{-1} \quad \text{and} \quad \Gamma = C_0 k \Omega, \quad (6.34)$$

where  $C_0$ ,  $k$  and  $\Omega$  are a model constant, turbulent kinetic energy and a turbulence frequency, respectively. Inserting these quantities into Eq. (6.29) and subsequently multiplying with  $U_i^{n+1}$  and taking the average leads to

$$\langle U_i^{n+1} U_i^{n+1} \rangle = \langle U_i^n U_i^n \rangle e^{-\frac{2\Delta t}{\tau}} + \frac{2}{3} k^n \left(1 - e^{-\frac{2\Delta t}{\tau}}\right). \quad (6.35)$$

Taking the sum  $i = 1$  to  $i = 3$  gives

$$\begin{aligned} 2k^{n+1} &= 2k^n e^{-\frac{2\Delta t}{\tau}} + 2k^n \left(1 - e^{-\frac{2\Delta t}{\tau}}\right) \\ &= 2k^n \end{aligned} \quad (6.36)$$

independent of the time step size  $\Delta t$ .

The velocity autocorrelation function can be derived by multiplying Eq. (6.29) with  $U_j^n$  and subsequent averaging. The result

$$\frac{\langle U_i^{n+1} U_j^n \rangle}{\langle U_i^n U_j^n \rangle} = e^{-\frac{\Delta t}{\tau}} \quad (6.37)$$

proves the correct behavior.

Further validation is now done by conducting numerical experiments. To illustrate the improvements of the new scheme, calculations are performed with both the new scheme and a standard second order finite differencing method [31], i.e. with the schemes

$$U_i^{n+1} = U_i^n + \left( -\frac{\Delta t}{\tau} U_i^n + \sqrt{\Gamma \Delta t} \xi_i \right) \left( 1 - \frac{\Delta t}{2\tau} \right) \quad \text{and} \quad (6.38)$$

$$X_i^{n+1} = X_i^n + \frac{U_i^n + U_i^{n+1}}{2} \Delta t. \quad (6.39)$$

To simulate the forced turbulence, the diffusion coefficient  $\Gamma$  was adjusted such that the turbulent kinetic energy  $k = 0.5 \langle U_i U_i \rangle$  is conserved and was set to

$$\Gamma = \sqrt{\frac{4k}{3\tau}}. \quad (6.40)$$

To keep the statistical error small, in all simulations an ensemble of  $10^6$  particles was employed, which were released at the initial position  $\mathbf{X}(t_0) = 0$ . The simulation time was  $10 \times \tau$  in all cases and the time resolutions  $\Delta t/\tau \in \{0.05, 0.1, 0.5, 1.0, 1.5\}$  were used. In a first experiment the effect of the time scale resolution on the kinetic energy evolution was investigated. A Gaussian initial particle velocity distribution with  $\langle U_i \rangle = 0$  and  $\langle U_i U_i \rangle = 2k_0$  was employed. In this study,  $k$  was evaluated from the evolving particle ensemble after every time step. The progress in time of  $k$  is depicted in Fig. 5 for both the new and the common second order particle integration scheme. Clearly, in forced homogeneous turbulence the kinetic energy should be preserved. One can observe that the common scheme does not preserve  $k$  for reasonable time step sizes; even for  $\Delta t = 0.1\tau$  the decrease of  $k$  after a simulation time of  $10\tau$  is significant. With the new scheme, on the other hand, the kinetic energy is preserved up to a very small statistical error for  $\Delta t$  as large as  $1.5\tau$ .

The goal of the second numerical experiment was to investigate the accuracy of the predicted conditional moments. This time,  $k = k_0$  was kept constant throughout the whole simulation and  $U_1$  at  $t = 0$  was  $0.945\sqrt{2k_0/3}$  for all computational particles, which were launched at  $X_1 = 0$ . Figs. 6, 7, 8, 9 and 10 show the evolutions of the normalized conditional moments  $\langle X_1 | \mathbf{X}(t_0) \mathbf{U}(t_0) \rangle$ ,  $\langle X_1 X_1 | \mathbf{X}(t_0) \mathbf{U}(t_0) \rangle$ ,  $\langle U_1 | \mathbf{U}(t_0) \rangle$ ,  $\langle U_1 U_1 | \mathbf{U}(t_0) \rangle$  and  $\langle X_1 U_1 | \mathbf{X}(t_0) \mathbf{U}(t_0) \rangle$ , respectively. In particular for  $\langle X_1 | \mathbf{X}(t_0) \mathbf{U}(t_0) \rangle$ ,  $\langle X_1 X_1 | \mathbf{X}(t_0) \mathbf{U}(t_0) \rangle$  and  $\langle U_1 U_1 | \mathbf{U}(t_0) \rangle$  huge errors can be observed for the common scheme, even for time steps as small as  $\Delta t = \tau/2$ . Contrariwise, the solutions with the new scheme are exact, independent of the time step size. A similar statement can be made about the autocorrelation function of  $U_1$ , which is depicted in Fig. 11. Note that for the normalization of the plots (Figs. 6-10) the reference quantities  $U_r = \sqrt{2k_0/3}$  and  $L_r = U_r \tau$  are employed.

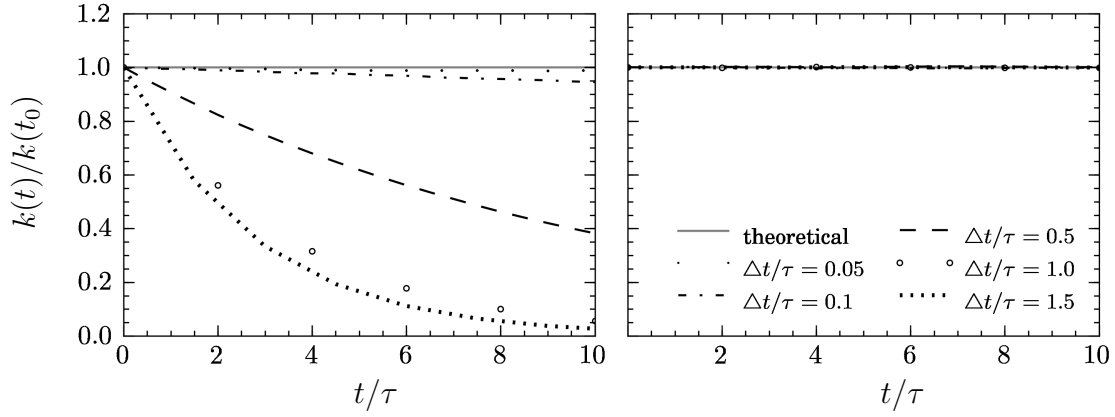


Figure 5: Time evolution of the normalized kinetic energy for (left) the finite differencing scheme and (right) the new integration scheme for different time steps

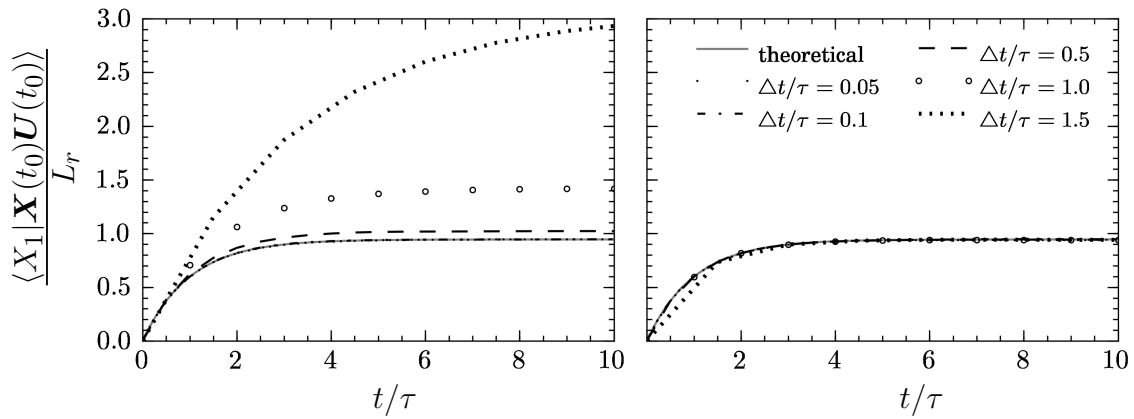


Figure 6: Mean particle position conditioned on the initial particle velocity for (left) the finite differencing scheme and (right) the new integration scheme.

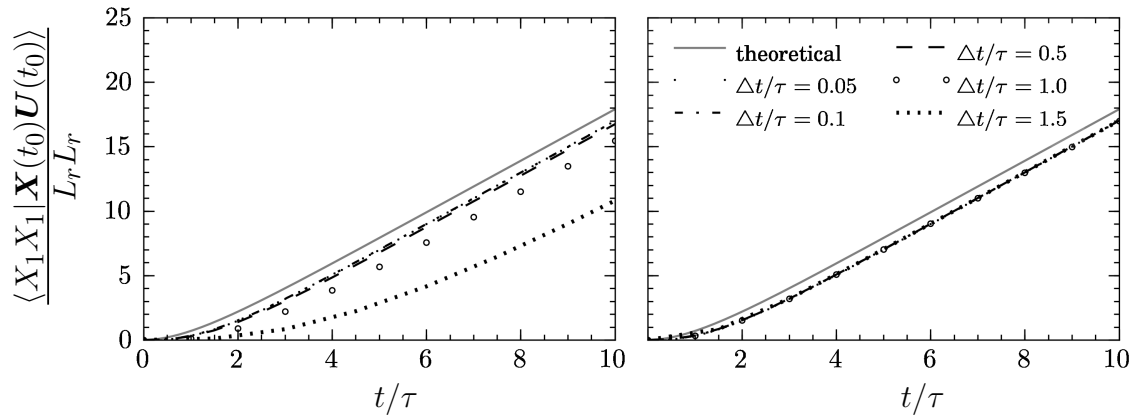


Figure 7: Conditioned particle position variance for (left) the finite differencing scheme and (right) the new integration scheme.

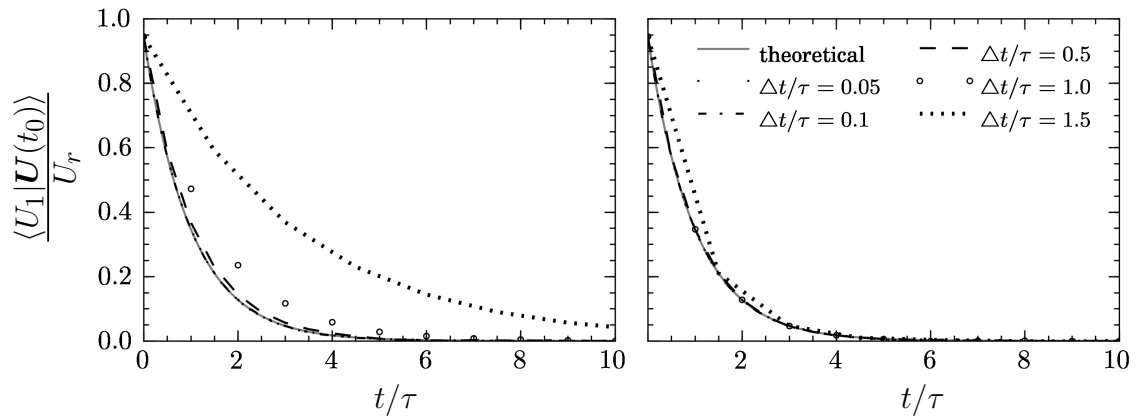


Figure 8: Mean particle velocity conditioned on the initial velocity for (left) the finite differencing scheme and (right) the new integration scheme.

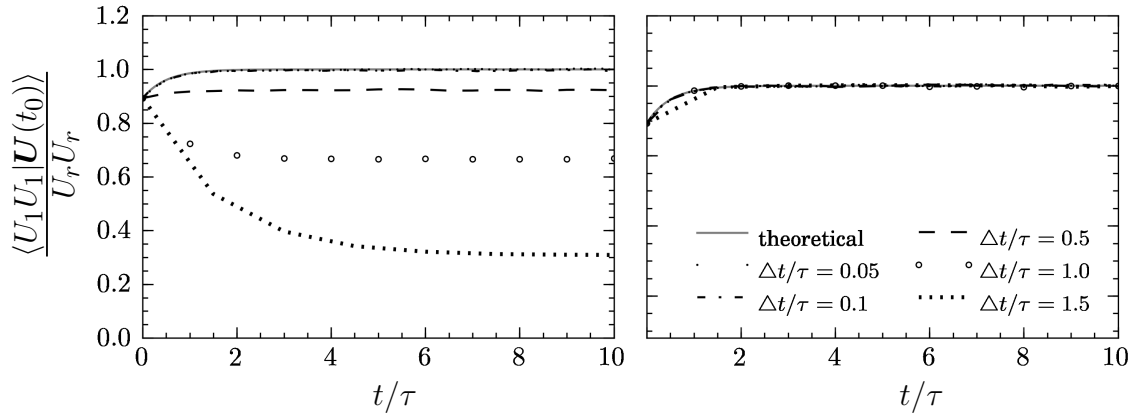


Figure 9: Conditioned particle velocity variance for (left) the finite differencing scheme and (right) the new integration scheme.

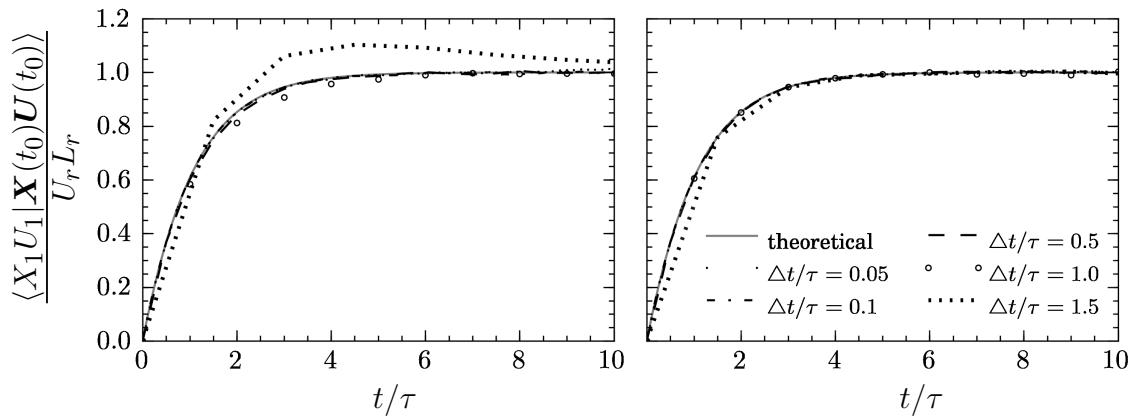


Figure 10: Conditioned particle position-velocity covariance for (left) the finite differencing scheme and (right) the new integration scheme.

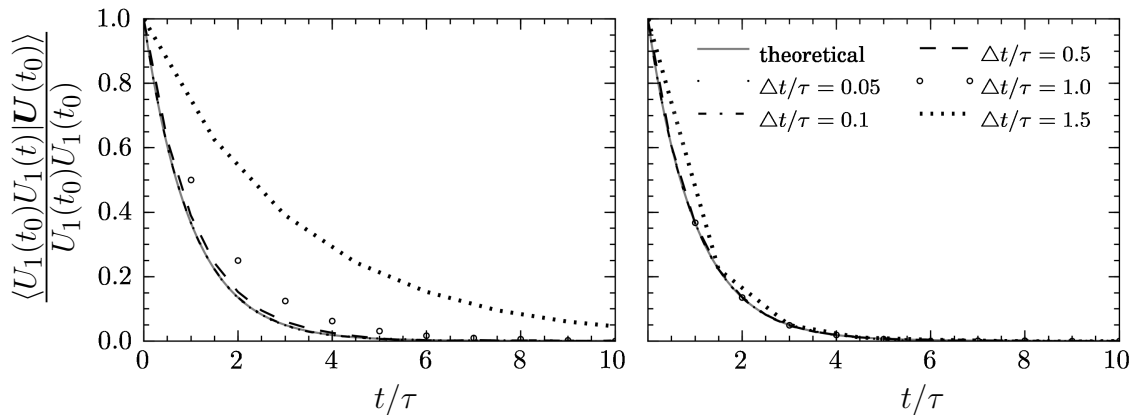


Figure 11: Conditioned velocity autocorrelation function for (left) the finite differencing scheme and (right) the new integration scheme.

### 6.3 Discussion and Conclusion

Chapter 6 deals with the accurate integration of particle position and velocity in a Monte Carlo PDF method, where a Langevin equation is employed to model the fluctuating velocity. Of course the developed method could be applied for other statistical properties as long as the evolution equation is in the form of a Langevin equation.

Besides spatially resolving the statistical moments, which appear in the particle evolution equations (see for instance Eq. (4.35)), it is crucial to honor the involved time scales appropriately with the time stepping scheme. If for example a local time stepping scheme is employed (see Appendix B and Muradoglu et al. [50],  $\tau$  may be much smaller than the time step size.

As mentioned at the beginning the development here follows closely and is an adaption of the work by Minier and coworkers [47]. Based on Itô calculus and the interpretation of the stochastic integral as Riemann sums, a statistically exact integration scheme is devised. The exact integration of each of the considered stochastic differential equation alone, would lead to exact statistical results for the single quantities. Here we devised a scheme, which also takes care of the joint moments between the stochastic variables. For that the stochastic term in one of the equations is split up into two terms and one of the appearing random numbers is used in the stochastic term of the second equation. Furthermore, the coefficients of the stochastic terms are determined by comparing the exact moment evolution equations with the proposed general moment equations.

Numerical studies of forced homogeneous turbulence demonstrate the superiority of the developed scheme compared with a standard second order scheme of finite difference type. The results also confirm that the solutions for the first and second moments are statistically exact, independent of the time step size. Moreover, the computational costs of the two schemes are in the same order.





Part II

# Modeling of Partially Premixed Turbulent Combustion



## 7 Review of Combustion Regimes and Modeling Approaches

In this chapter a short introduction to the wide field of turbulent combustion is given. Usually one divides it into premixed, non-premixed and partially premixed combustion regimes. The basic distinction between non-premixed and premixed combustion is due to the state of reactants when they enter the combustion chamber. Partially premixed flames exhibit features from both of the basic regimes and are especially challenging to model. In the next two subsections an introduction to premixed (subsection 7.1), non-premixed and partially premixed combustion (subsection 7.2) phenomena is given and a short review of existing modeling approaches. In the latter subsection the basic concept of a new modeling approach for partially premixed combustion is outlined, which is presented in detail in chapter 8.

### 7.1 Premixed Combustion

#### 7.1.1 Phenomenological Observations

In premixed combustion the fuel and oxidizer streams are completely mixed before they approach the combustion zone. Typical examples of practical devices with premixed flames are stationary gas turbines, spark-ignition engines or household burners.

The most characteristic physical phenomenon of a premixed flame is its ability to propagate through the mixture and normally we can clearly distinguish unburnt and burnt regions. The two regions are divided by the reaction zone, which propagates towards the unburnt mixture. In a laminar premixed flame the flame front is a smooth line (2D) or plane (3D), which moves with the so called laminar flame speed  $s_L$ . The structure of a laminar premixed flame is depicted in Fig. 12. The zone where the temperature increases can be divided into a reaction zone and a preheated zone. The preheating of the unburnt gas through heat diffusion is in laminar flames the main reason for the flame propagation.

If the mixture field is turbulent, the flame front interacts with the turbulent eddies and the flame zone becomes wrinkled. Two dimensionless parameters are important for the characterization of premixed flames in turbulent flows, i.e. the Damköhler and the Karlovitz

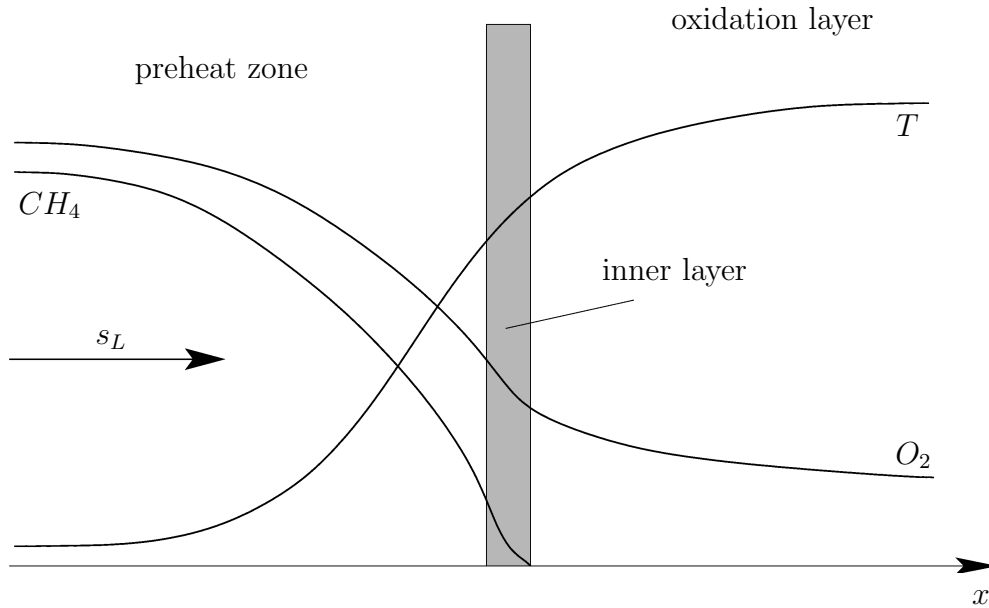


Figure 12: Sketch of a laminar premixed methane-air flame. The flame propagates with the laminar flame speed  $s_L$  and the main reactions are taking place in the so called inner-or reaction layer.

numbers. The Damköhler number is the ratio of the integral turbulent time scale  $\tau_t$  to a chemical time scale  $\tau_c$ , i.e.

$$Da = \frac{\tau_t}{\tau_c}, \quad (7.1)$$

whereas the Karlovitz number relates the chemical time scale  $\tau_c$  to the Kolmogorov time scale  $\tau_K$ , i.e.

$$Ka = \frac{\tau_c}{\tau_K}. \quad (7.2)$$

There are different approaches for flame regime characterizations, for instance by Borghi [6], Peters [57], Abdel-Gayed and Bradley [1] and Poinso et al. [61]. There are some basic distinctions which can generally be made. If  $Ka < 1$  the chemical time scale is smaller (faster) than the smallest turbulent time scales and the turbulent structures cannot entrain the flame zone. This is usually called the wrinkled and the corrugated flamelet regimes. In the thin reaction zone regime the eddies disturb the preheated zone. This happens if  $1 < Ka < 100$ . If  $Ka > 100$  the reaction zone gets disrupted by the turbulence and is correspondingly called the broken reaction zone regime. The Damköhler number can give a further criterion for the flame characterization and is mostly used to decide if the overall reaction rate is limited by mixing or by the chemical reaction itself.

Further physical phenomena concerning mainly the mutual influence of turbulence and flame zone are listed below:

- (i) Viscosity dependency on temperature can lead to relaminarization of the turbulent flow downstream of the flame front.

- (ii) Gas expansion due to heat release leads to counter gradient diffusion (gradient diffusion assumptions are wrong in this case).
- (iii) Flame generated turbulence due to flow acceleration and heat release through the flame front.
- (iv) Flame modification through strain in the flow field.

More extensive information about the definitions of length and time scales and about the characterization of premixed flames can be found for instance in the textbooks of Poinso and Veynante [60] and Peters [58].

### 7.1.2 Modeling Approaches

In the modeling approaches for premixed combustion one usually defines a quantity which indicates the location of the flame front and solves a appropriate transport equation for this indicator variable in order to track the evolution of the flame front. This transport equation contains terms which describe the interaction of the flame with the turbulence as well as source terms. The modeling of those terms is a major challenge. There are two main approaches, one the one hand the so called Bray-Moss-Libby (BML) model [11] and on the other hand the level set approaches, e.g. Osher and Sethian [54] or Williams [80]. In the BML approach a transport equation for a progress variable  $c$  is solved, where usually the progress variable is defined as a normalized temperature. In the thin reaction zone regime one can assume a bimodal PDF of  $c$ , which means that the state of a fluid particle is either fully unburnt or fully burnt. Finding a closure for the progress variable source term is the main challenge in the BML approach.

The level set approach employs instead of a progress variable a so called  $G$ -equation. The function  $G(\mathbf{x}, t)$  is defined with  $G < G_0$  in regions of unburnt gases and  $G > G_0$  in burnt gases, where  $G_0$  is an arbitrary but for a specific combustion event fixed level of  $G$  in the flame front. From the  $G$ -equation it is possible to derive a flamelet equation similar to the one in non-premixed combustion. This level set approach is mainly suited for the corrugated premixed regime.

*Remark:* In the context of this work, premixed combustion is insofar of interest, since physical phenomena of both premixed and non-premixed combustion regimes are observed in partially premixed flames. Here, the modeling will start from the non-premixed perception but also includes elements of premixed approaches.

## 7.2 Non-Premixed and Partially Premixed Combustion

### 7.2.1 Phenomenological Observations

The main characteristic of non-premixed combustion is that the fuel and oxidizer streams are supplied separately into the combustion chamber. Typical representatives of non-premixed combustion are found in furnaces, airplane gas turbines, diesel engines, but also candle flames (laminar). The reaction rate in non-premixed combustion is mainly controlled by the diffusion of fuel and oxidizer towards the reaction zone and therefore they are also called diffusion flames. The most obvious difference of the flame behavior compared to premixed flames is that they do not exhibit a propagation mechanism. From a security point of view this is an advantage, since the flame cannot propagate into the combustion chamber intake (flashback) and furthermore flammable mixture exists only in the flame zone. In a turbulent flow field the fuel and oxidizer streams are mixed by turbulent and molecular diffusion and in the region where a flammable mixture is formed chemical reactions can take place, if enough initial heat is supplied. The turbulence-flame interaction is characterized by the same effects as presented for premixed combustion, which are: relaminarization, gas expansion effects, flame stretching and flame induced vorticity. The influence of the turbulence on the diffusion process makes the understanding of non-premixed flames especially difficult. Turbulent structures interact with the diffusion layer around the reaction zone and change the mass flow rate of the flammable mixture into the reaction zone, which again influences the total heat release due to chemical reactions. In many cases the mixing time scale (of both turbulent and diffusive mixing) is much larger than the chemical time scales and therefore the assumption of infinitely fast chemistry can be made. This assumption simplifies the problem significantly, since the mixing process is decoupled from the chemical reaction part and can be treated isolated. Burke and Schumann [14] were the first who introduced the infinitely fast chemistry assumption in 1928. In this context the conserved scalar concept is important, where Bilger [5] was one of the major contributor and still his definition of a conserved scalar is often used. A passive scalar is constructed, for instance from elemental mass fractions, which are not affected by chemical reactions and can be used to characterize the mixing problem. Typically, such a scalar is normalized and called mixture fraction  $Z$ . The mixture fraction can then uniquely be related to temperature, mass concentrations and the density of the mixture.

If the mixing time scale is in the same order of magnitude as the chemical time scale, the assumption of infinitely fast chemistry is no more justified. This is the case when the turbulence intensity increases and accelerates the mixing rate. From a certain level of turbulence intensity the flame can even locally or globally extinguish due to too fast heat diffusion away from the reaction zone. Considering for instance a jet diffusion flame, this happens most probably locally after the fuel jet exits the nozzle, where the turbulent production is maximal. In this region fuel and oxidizer can already mix without being burnt and stratified mixing layer structures evolve. That is when the regime of partially premixed combustion is entered. As the name implies, both premixed and non-premixed combustion features occur in this regime. A canonical example are the lifted jet flames.

In such a configuration if the jet velocity is small enough, the flame remains attached to the burner nozzle, but if the fuel jet velocity exceeds a certain value, the flame detaches from the burner rim and the main flame zone travels farther downstream. See Fig. 13 for an illustration. The stabilization mechanisms of such lifted flames are still not definitely

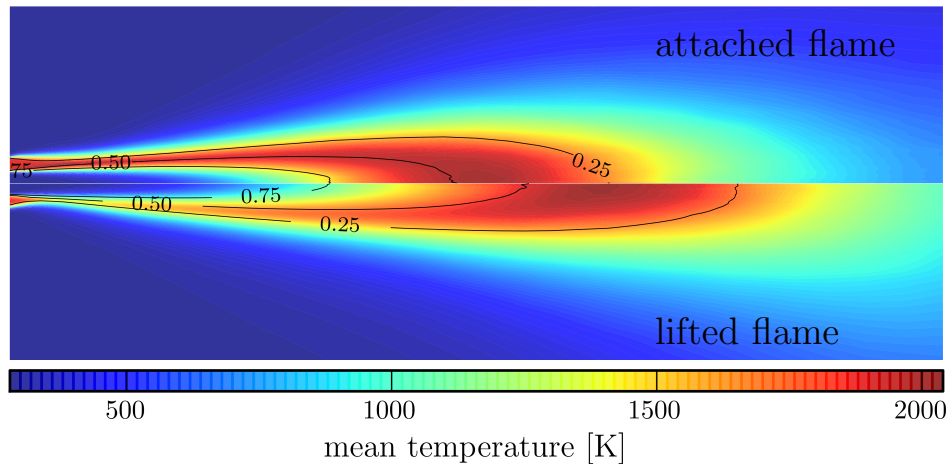


Figure 13: Temperature contour plot of a attached (upper part) and a lifted jet flame (lower part). The contour plots are simulation results of Sandia flame D and F.

known, but different experimental and numerical (DNS) investigations show that so called triple or edge flames play an important role. Some important DNS studies are: Domingo and Vervisch [21], Echekki and Chen [25], Domingo et al. [23].

There are a few points which are generally accepted:

- 1) At the stagnation point of the flame the scalar dissipation rate is considerably below the quenching limit.
- 2) A premixed flame propagation exists at the stagnation point.
- 3) The flame structure involves lean and rich premixed branches with trailing diffusion flames attached. These structures are known as triple or edge flames.
- 4) The heat release is inversely proportional to the scalar dissipation rate. High scalar dissipation rate means low heat release.

### 7.2.2 Modeling Approaches

The most successful modeling approach for non-premixed combustion is the laminar flamelet model. The original idea stems from Williams in 1975 [79]. He considered a turbulent flame

as an ensemble of embedded laminar flamelets, which is the basic assumption of this approach. Liew in 1981 [42] suggested to use calculated profiles of laminar diffusion flames to obtain statistical information of the turbulent flame. Peters [55] and Kuznetsov [39] derived flamelet equations based on the mixture fraction dependent on the scalar dissipation rate. The classical flamelet equation is a diffusion - reaction balance equation and reads (e.g. [58] sec. 3.11)

$$\rho \frac{\partial \phi_\alpha}{\partial t} = \frac{\rho}{Le_\alpha} \frac{\chi}{2} \frac{\partial^2 \phi_\alpha}{\partial Z^2} + \omega_\alpha, \quad (7.3)$$

where  $\phi_\alpha$ ,  $Le_\alpha$ ,  $\chi$  and  $\omega_\alpha$  are species mass fraction of species  $\alpha$ , Lewis number, scalar dissipation rate and chemical source term, respectively. The Lewis number is the relation of energy and mass diffusion rate

$$Le_\alpha = \frac{\Gamma_h}{\Gamma_\alpha}. \quad (7.4)$$

$\Gamma_h$  is the heat diffusion coefficient and  $\Gamma_\alpha$  the mass diffusion coefficient for species  $\alpha$ . The scalar dissipation rate is a measure for the mixture fraction variance decay and is defined as

$$\chi = 2\Gamma |\nabla Z|^2. \quad (7.5)$$

$\Gamma$  is the diffusion coefficient for the mixture fraction. More about the definition of the mixture fraction, the scalar dissipation rate and the choice of  $\Gamma$  can be found in Peters [58] secs. 1.8, 3.2 and 3.7.

The flamelet approach is valid as long as the smallest eddies (Kolmogorov scale) are larger than the reaction layer thickness, in that case the flamelets are embedded in laminar fluid structures of the turbulent flow field. The advantage of this approach is that the overall problem, i.e. the interaction between turbulence and reaction is split into a mixture problem and a flame structure problem. The mixture problem consists of finding the mixture fraction field  $Z(\mathbf{x}, t)$ , which is of course strongly influenced by the turbulence. The relation between  $Z$ , the species mass fractions, temperature and the chemical source terms states the flame structure problem. In numerical simulations this problem is treated completely separate and precomputed flamelet tables parameterized by mixture fraction and scalar dissipation rate are produced. During the flow calculations, the chemical source terms for the scalar values are obtained by a lookup in the flamelet tables.

The classical flamelet approach fails in the case of partially premixed combustion, since the model has no features accounting for extinction and reignition or premixed flame propagation. Some early modeling contributions are due to Bradley et al. [7] and [8], Sanders and Lamers [69], Müller et al. [48] and Chen et al. [16]. Bradley et al. successfully applied a premixed combustion model with imposed flammability limits and extended the model to allow for premixed flame quenching due to strain. On the contrary, Sanders and Lamers used diffusion flamelets and extinction is due to flame stretching by Kolmogorov eddies. Both models predict the linear dependency of lift off height on the fuel jet velocity, whereas the model of Bradley also correctly reproduces the blow off velocity as a function of the nozzle diameter. Müller et al. calculate scalar fields of a level set function  $G$  and the mixture fraction. In the  $G$ -equation the turbulent flame speed appears as an unclosed quantity.



Three different terms contribute to the flame speed: a premixed flame propagation involving the laminar premixed flame speed as a function of the mixture fraction, a term for partial premixing, which limits the flame propagation to region with high probability of stoichiometric mixture, and a flame quenching term based on the scalar dissipation. This model successfully predicts the correct lift off height of jet flames. More recent approaches use a reaction progress variable together with a flamelet model. Such combustion models are applied for instance in multiple mapping conditioning (MMC) methods by Kronenburg [38] or in the context of subgrid combustion models in LES codes by Domingo et al. [22], Pierce et al. [59], Vervisch et al. [75] or Ihme et al. [33]. The main task in these modeling approaches is to obtain accurate statistical information for different scalar quantities, where also joint information is of crucial importance. Most of the above references use presumed PDFs for the scalar distribution and the modeling is done at the level of first and second moment equations.

A similar approach can be adapted for transported PDF methods and is the topic of the following chapter 8. The difficulty thereby is to find appropriate models for the unclosed terms in the PDF transport equation but if this can be achieved, the advantage is that the PDF evolves in a physical way. An important effect which appears unclosed in transported PDF methods is the molecular mixing. Note that also in LES/FDF approaches molecular mixing is unclosed since it happens on the subgrid scale. Going from simple to more complex mixing model approaches, there are the interaction by exchange with the mean (IEM) mixing model by Villermaux and Devillon [76], the Curl model [19], the mapping closure (MC) model by Pope [64], the Euclidean minimum spanning tree (EMST) model by Subramaniam and Pope [73] and the parameterized scalar profile (PSP) model by Meyer and Jenny [46] and [45]. Also many modifications and specializations of those models were developed by different research groups.

In this work we are going to develop a combustion model based on the transported joint PDF method presented in part I. The new model uses the flamelet and progress variable approaches in combination with a phenomenologically motivated reactive mixing model.

Very insightful reviews about non-premixed and partially premixed combustion and their modeling approaches can be found in the textbooks of Peters [58], Poinson and Veynante [60] and Warnatz et al. [77].

## 8 New Model for Partially Premixed Combustion

Based on the turbulent combustion introduction of the previous chapter a physical motivation for the new combustion model is given in the first subsection. Then, in subsection 8.2, the single ingredients, i.e. a reactive mixing model, a progress variable approach and a scalar dissipation rate model are derived and explained. In subsection 8.3 the validation test cases and the results are presented and the overall approach is summarized and some concluding remarks are drawn in section 8.4. Finally, a future extension of the model is outlined in subsection 8.5, which is the calculation of laminar triple flames and completes the idea of the presented combustion model.

### 8.1 Motivation

The new modeling approach is based on the physical fine scale picture of a turbulent partially premixed flame composed of laminar triple flames embedded in the turbulent structures. The sketch in Fig. 14 illustrates this assumption, using a lifted jet flame setup as a typical example. In the classical flamelet approach the thermo-chemical state of a fluid particle is uniquely related to the mixture fraction and the scalar dissipation rate, i.e.

$$h_s = f(Z, \chi), \quad (8.1)$$

where the scalar dissipation rate is defined according to Eq. (7.5). Here,  $Z$  can be seen as a normalized fuel to oxidizer ratio of the mixture and if the diffusion coefficients of all species are assumed to be equal and also the Lewis number  $Le_\alpha = \Gamma_h/\Gamma_\alpha$  is unity, then  $\Gamma = \Gamma_h = \Gamma_\alpha$ .

The functional dependency in Eq. (8.1) implies that in mixture fraction-enthalpy space only the gray shaded region (indicated in Fig. 15(a)) between the hottest and coldest burning flamelets is accessed. This means that a mixture with  $Z$  not equal 0 (pure oxidizer) or 1 (pure fuel) has an increased enthalpy according to the flamelet relation Eq. (8.1). This unique relation breaks down in the case of partially premixed combustion (see for instance the example of a lifted jet flame in Fig. 14) and implies that the whole region in the  $Z$ - $h$ -space below the hottest flamelet can be accessed as depicted in Fig. 15(b) by the gray shaded area.

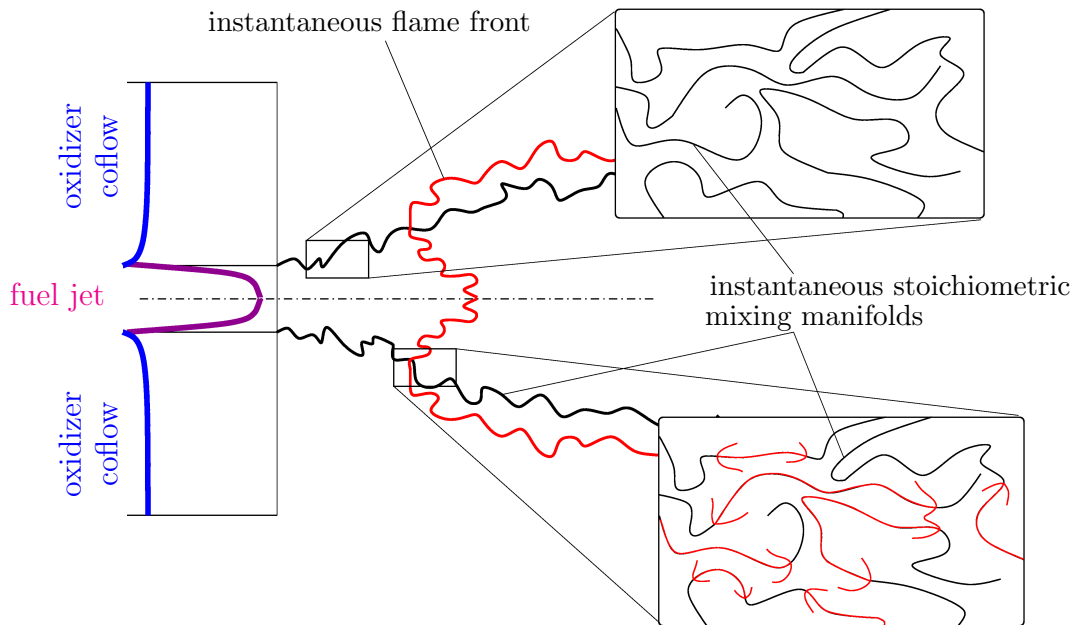


Figure 14: Sketch of a lifted jet flame. The upper box represents an enlarged extinguished region of a partially premixed mixture field with lines on the stoichiometric manifolds. The lower zoom shows a sketch of the flame base with triple or edge flames traveling along the stoichiometric manifolds.

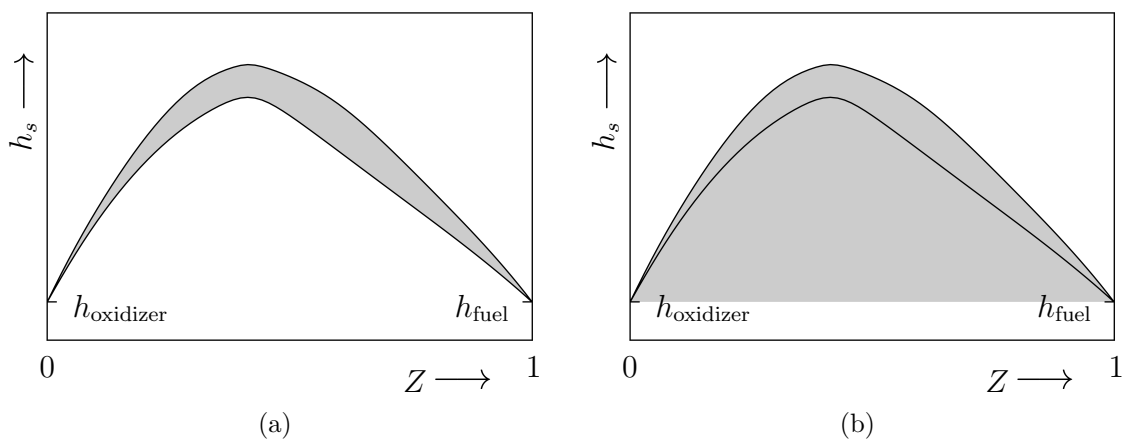


Figure 15: Accessed region in  $Z-h_s$ -space in a) the classical flamelet approach for non-premixed combustion and b) in the case of partially premixed combustion.

High turbulence levels and high strain rates in such flames lead to flame quenching and therefore fuel and oxidizer are mixing without combustion taking place. Hence, in order that a fluid particle can ignite or reignite, two basic requirements must be fulfilled: on one hand, the strain or scalar dissipation rate must be below the extinction limit, and on the other hand the flame front (edge flame) must have reached the particle.

To cope with this physical phenomenon, we propose a combustion model which is a combination of a modified flamelet and a progress variable approach. The latter one is used to decide, if a fluid particle has the ability to react or not. The flamelet idea is modified, such that one can account for the different combustion regimes. A reactive mixing model is developed to evolve particles in enthalpy - mixture fraction space based on the progress variable condition (i.e. extinct or ignited) and on the state of the environment around the particle.

In the context of transported joint PDF methods, we have the advantage that the joint statistics of different quantities is available and can be used for model developments. Of course, the single models themselves influence the evolution of the used joint statistics. However, in PDF methods one has the possibility to improve the models such that the joint statistics is represented more accurately, which then allows for potentially better physical models. Here, the joint statistics of mixture fraction, progress variable and scalar dissipation rate is considered. Since the numerical solution algorithm for the joint PDF equation is based on a Lagrangian particle method, the modeling can be done by considering the evolution of Lagrangian fluid particles. A further advantage is that in such a stochastic Lagrangian formulation nonlinear turbulent convection appears in closed form; for instance no gradient diffusion assumptions like for instance  $\widetilde{uc''} \approx -\Gamma_c \nabla \tilde{c}$  have to be made.

## 8.2 Model Development

### 8.2.1 Reactive IEM Mixing Model

The reactive mixing model is an approach to cope with local extinction and instead of sequentially applying a mixing and a reaction time step, these two processes are treated simultaneously by constructing physically motivated fluid particle paths in mixture fraction - enthalpy space.

In the classical flamelet approach, a diffusion - reaction equation (see Eq. (7.3)) is solved and the resulting flame tables are used in a flame calculation to obtain the reaction source term. Here, however, these flame tables are applied differently to account for partially premixed combustion. In the non-flammable regions of such a flame, fuel and oxidizer evolve according to a modified mixing model. Moreover, the evolution of a fluid particle depends on its reaction state (i.e. extinct or ignited) and on the environment around the particle. Various new symbols are introduced at this point; see Fig. 16 for the notation. First, we define the mixture fraction values  $Z_{f1}$  and  $Z_{f2}$ , which mark the left and right

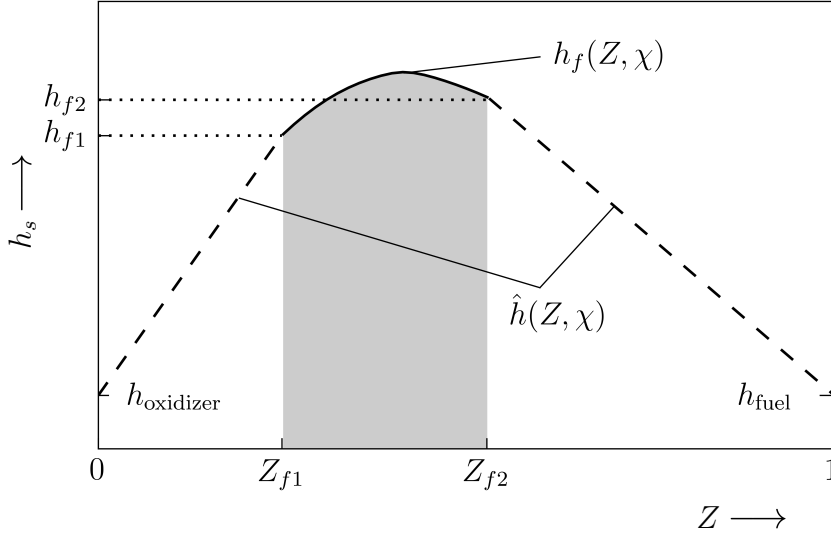


Figure 16: Notations used during the explanations of the reactive mixing model, sketched for a particular scalar dissipation rate. The gray shaded region between  $Z_{f1}$  and  $Z_{f2}$  is the flammable zone in mixture fraction space,  $\hat{h}(Z, \chi)$  denotes the mixing lines from the flame zone edge to the oxidizer, respectively the fuel streams,  $h_f(Z, \chi)$  is the enthalpy of the steady flamelet solution inside the flammable zone and  $h_{f1}$  and  $h_{f2}$  are the enthalpies of the flamelet solution on the edge of the flame zone. Note that  $h_{f1}$  and  $h_{f2}$  depend on  $\chi$  as well.

locations of the flammable range ( $Z_{f1} < Z_{f2}$ ). The evolution of the particle's mixture fraction  $Z^*$  is described by the IEM mixing model, i.e.

$$\frac{dZ^*}{dt} = -\frac{2\tilde{\varepsilon}}{C_\phi \tilde{k}} (Z^* - \tilde{Z}), \quad (8.2)$$

where  $\tilde{k}$ ,  $\tilde{\varepsilon}$  and  $\tilde{Z}$  are the Favre averages of the turbulent kinetic energy, the turbulent dissipation rate and the mixture fraction, respectively, and  $C_\phi$  a model constant, describing the mechanical to scalar time scale ratio (here  $C_\phi = 2.5$ ).

To evolve the particle's sensible enthalpy  $h_s^*$ , one has to distinguish between different scenarios. If a particle is not ignited (see Fig. 17(a)) (i.e. if its progress variable  $c^*$  is zero) then  $h_s^*$  evolves according the IEM mixing model, i.e.

$$\frac{dh_s^*}{dt} = -\frac{2\tilde{\varepsilon}}{C_\phi \tilde{k}} (h_s^* - \tilde{h}_s). \quad (8.3)$$

This means that no chemical reactions are considered in that case.

On the other hand, if a particle is ignited (i.e. if its  $c^*$ -value is 1), its sensible enthalpy is set on a constructed curve in the  $Z$ - $h$ -space while the new  $Z^*$  is determined by the IEM mixing

model. If both  $Z^{*,n}$  (the superscript  $n$  denotes values at the beginning of a time step) and  $\tilde{Z}$  are either larger than  $Z_{f2}$  (see Fig. 17(b)) or smaller than  $Z_{f1}$ , the constructed curve is the line from  $(Z^{*,n}, h^{*,n})$  to  $(\tilde{Z}, \hat{h}(\tilde{Z}, \chi))$ . The function  $\hat{h}(Z, \chi)$  represents the mixing lines from  $(0, h_{\text{oxidizer}})$  to  $(Z_{f1}, h_{f1})$  and from  $(1, h_{\text{fuel}})$  to  $(Z_{f1}, h_{f2})$ . The values of  $h_{f1}$  and  $h_{f2}$  are those given by the corresponding steady flamelet solution at  $Z_{f1}$  and  $Z_{f2}$ , respectively, and also depend on the scalar dissipation rate  $\chi$  (since the flamelet solution depends on  $\chi$ ). If  $Z^{*,n}$  and  $\tilde{Z}$  are separated either by  $Z_{f1}$  or  $Z_{f2}$ , then the constructed curve consists of three sections. If  $Z^{*,n}$  is smaller than  $\tilde{Z}$  (see Fig. 17(c)), the first section is the straight line from  $(Z^{*,n}, h^{*,n})$  to  $(Z_{f1}, h_{f1})$ . The second section consists of the steady flamelet solution from  $Z_{f1}$  to  $Z_{f2}$  and the third section is the straight line from  $(Z_{f2}, h_{f2})$  to  $(1, h_{\text{fuel}})$ . Analogously, the three sections in the case if  $Z^{*,n} > Z_{f2}$  are the straight line from  $(Z^{*,n}, h^{*,n})$  to  $(Z_{f2}, h_{f2})$ , the flamelet solution between  $Z_{f1}$  and  $Z_{f2}$  and finally the straight line from  $(Z_{f1}, h_{f1})$  to  $(0, h_{\text{oxidizer}})$ . If the particle lies in the flammable range (see Fig. 17(d)), i.e. if  $Z_{f1} \geq Z^{*,n} \geq Z_{f2}$ , the first section of the curve is the vertical line (in the  $Z$ - $h$ -space) from  $(Z^{*,n}, h^{*,n})$  to  $(Z^{*,n}, h_f(Z^{*,n}))$ , where  $h_f(Z, \chi)$  is the corresponding flamelet solution. The second part is the flamelet solution between  $Z^{*,n}$  and  $Z_{f2}$  (if  $\tilde{Z} \geq Z^{*,n}$ ) or  $Z_{f1}$  (if  $\tilde{Z} < Z^{*,n}$ ). The third section in this case is either the line from  $(0, h_{\text{oxidizer}})$  to  $(Z_{f1}, h_{f1})$  (if  $\tilde{Z} < Z^{*,n}$ ) or the line from  $(Z_{f2}, h_{f2})$  to  $(1, h_{\text{fuel}})$  (if  $\tilde{Z} \geq Z^{*,n}$ ).

### 8.2.2 Progress Variable

In the previous section, the particle evolution in mixture fraction-enthalpy space depending on the particle state is explained. Now we introduce the particle property  $c^* \in \{0, 1\}$ , which describes whether a flamelet associated with a particle is ignited. A transport equation for the Favre mean of this progress variable can be derived by multiplying the model equation for the joint PDF of velocity, mixture fraction, progress variable and turbulence frequency with the sample space variable of  $c$  and subsequent integration over the whole sample space. It reads

$$\langle \rho \rangle \frac{\partial \tilde{c}}{\partial t} + \langle \rho \rangle \tilde{U}_i \frac{\partial \tilde{c}}{\partial x_i} = - \frac{\partial \langle \rho \rangle \widetilde{u_i c''}}{\partial x_i} + \langle \rho \rangle \tilde{S}_c, \quad (8.4)$$

where  $\tilde{S}_c$  is the mean source term of  $c$  and is the only term which needs modeling. In our context we have to specify the ignition probability  $P$  for a statistical particle during a time step  $\Delta t$  and we propose the model

$$P = 1 - \exp(-\alpha \omega^* \langle c \rangle \Delta t), \quad (8.5)$$

where  $\alpha$  is a model parameter and  $\omega^*$  the particle's turbulence frequency. It can be shown that if a bimodal PDF for the progress variable and the previous ansatz for the ignition probability is assumed, then the source term becomes

$$\langle \rho \rangle \tilde{S}_c = \langle \rho \rangle (1 - \tilde{c}) \alpha \tilde{\omega} \langle c \rangle. \quad (8.6)$$

Note that Eq. (8.4) with source term (8.6) is equivalent to the transport equation used by the BML model of Bray and Moss [13] and Bray, Moss and Libby [11], which was developed

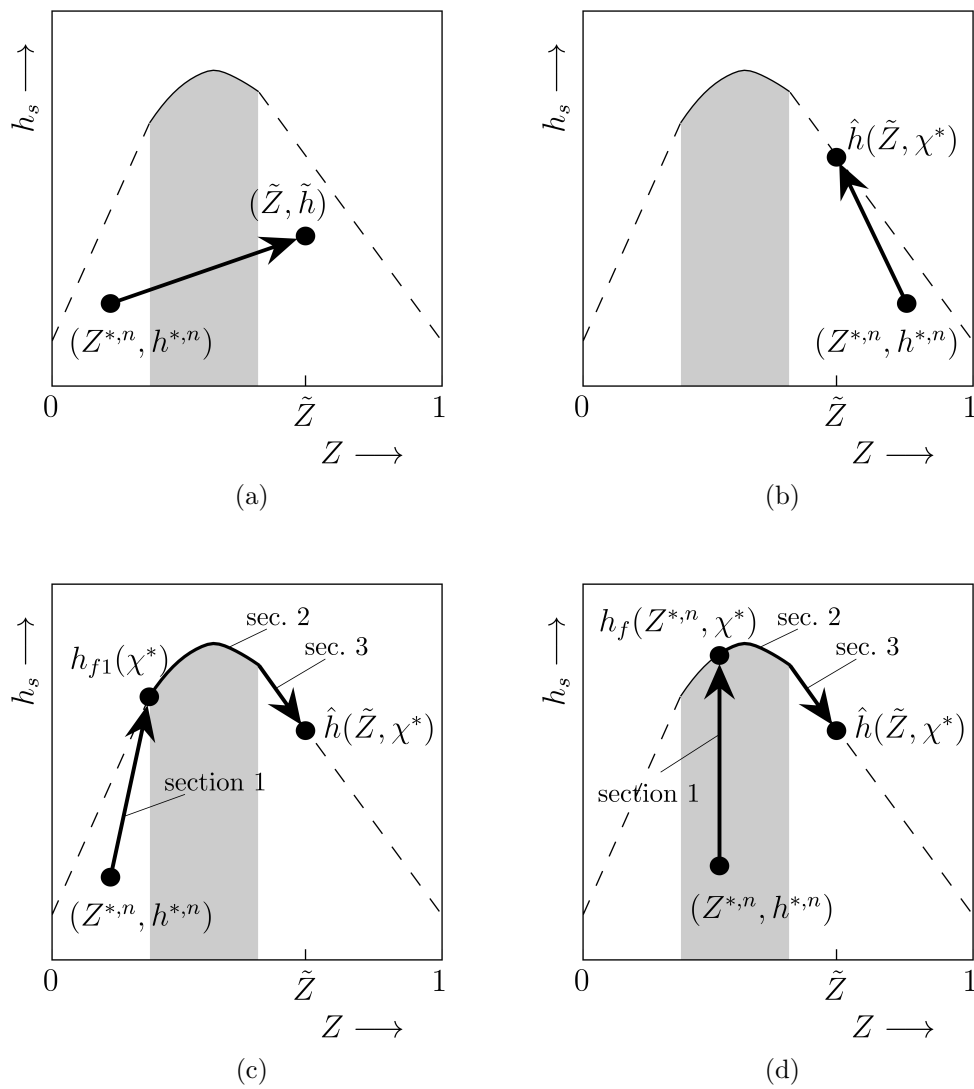


Figure 17: Different profiles of the reactive IEM mixing model; a) inert mixing, b) reactive profile if  $Z^{*,n}$  and  $\tilde{Z}$  are both on the right side of the flammable zone, c) reactive profile if  $Z^{*,n}$  and  $\tilde{Z}$  are on different sides of the flammable zone, and d) reactive profile if  $Z^{*,n}$  is located in the flammable zone.

for premixed combustion.

The dependency of the model parameter  $\alpha$  can be estimated on the basis of the source term closure in the BML approach. There, two kind of basic models exist: the flame crossing frequency model and the flame surface density model (see Bray and Libby [12] for considerations about the flame crossing frequency and general for both models the textbooks of Poinso and Veynante [60] secs. 5.3.5 and 5.3.6 and of Peters [58]).

In the first approach, the main driving phenomenon for the reaction rate is assumed to be the crossing frequency of the flame front at a certain point. The mean reaction rate is obtained as the product of the flame crossing frequency and the reaction rate per flame crossing. In the latter approach, the flame surface area per unit fluid volume is considered to be the key quantity and a transport equation for it is solved. In our case, if the ignition probability (8.5) is considered, the resulting source term (8.6) in Eq. (8.4) is similar to existing flame crossing frequency models, where the parameter  $\alpha$  accounts for the reaction rate per flame crossing. Note that for a general model,  $\alpha$  should be a function of the embedded triple flame propagation velocity and a flame stretch factor. For now, however,  $\alpha$  is set to a constant value, which implies that the ignition probability is assumed to be a function only of the mean progress variable  $\langle c \rangle$ , the particle's turbulence frequency  $\omega^*$  and the time step size  $\Delta t$ . It will be shown that despite this simplification the main effects occurring in the validation flames can be captured.

### 8.2.3 Scalar Dissipation Rate

To close the proposed combustion model, the scalar dissipation rate of a particle is modeled as

$$\chi^* = C_\chi \widetilde{Z''Z''} \omega^*, \quad (8.7)$$

where  $C_\chi$  is a constant as proposed by Poinso and Veynante in [60], sec. 6.4.3. Note that this model correctly predicts  $\chi^* = 0$  for  $\widetilde{Z''Z''} = 0$ . Moreover, since the individual turbulence frequency  $\omega^*$  is used, the scalar dissipation rate is different for each particle. Of course this model heavily depends on the performance of the mixing model, if the mixing model provides a wrong scalar field, then also the statistics of the scalar dissipation rate is inaccurate.

## 8.3 Validation and Results

Validation of the presented combustion model is performed with the Sandia flames E and F [3]. These are partially premixed jet flames with jet bulk velocities of  $74.4m/s$  and  $99.2m/s$ , respectively, and are stabilized by a pilot burner around the cold fuel jet. Those jet exit velocities lead to jet Reynolds numbers of 33600 for flame E and 44800 for flame F. The jet diameter  $D_j$  is for both cases  $7.2mm$  and the pilot diameter is  $D_P = 18.2mm$ . See Fig. 18 for a sketch of the flame setup. The jet is a mixture of 25% methane diluted by 75% air. The mixture fraction is defined according to Bilger [4] and leads to  $Z_j = 1$



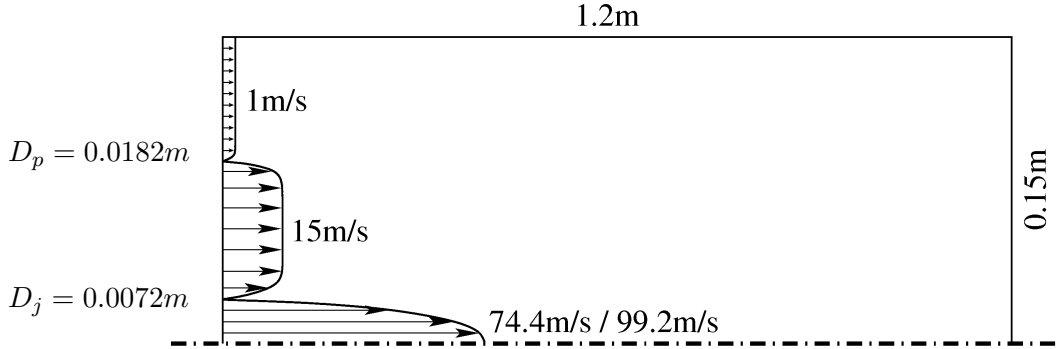


Figure 18: Setup of Sandia flames E and F.  $74.4\text{m/s}$  is the jet velocity of flame E and  $99.2\text{m/s}$  of flame F. The pilot and coflow velocities are for both flames the same.

in the jet, a stoichiometric mixture fraction of about 0.35 in the pilot stream (resulting in a pilot temperature of  $T_{st} = 1880\text{K}$ ) and  $Z_{co} = 0$  in the coflow. Both flames experience considerable amount of local extinction and reignition and are very challenging test cases for partially premixed turbulent combustion models. While flame E is only slightly lifted, flame F is close to global extinction.

The experimental setup is accurately described on the TNF workshop web site. The inlet boundary conditions required for the numerical simulations are available from the same web site together with detailed experimental data. The computational domain is chosen quite large with a width of  $L_y = 0.15\text{m}$  and a length of  $L_x = 1.2\text{m}$  in order to minimize the influence of the slip (at  $y = L_y$ ) and outlet (at  $x = L_x$ ) boundary conditions. To improve the results, the model constants  $\alpha$ ,  $C_\chi$  and  $C_{\omega_1}$  ( $C_{\omega_1}$  is used in the model for  $\omega^*$  in Pope [66] sec. 15.5.3) were adjusted. While  $C_{\omega_1}$  was set to 0.74, tuning of the other two model parameters was more difficult. Results confirm that the assumption of constant values for  $\alpha$  and  $C_\chi$  is not general enough and therefore further investigations will be necessary.

For the PDF simulations presented here, a grid of  $N_x = 50$  cells in downstream and  $N_y = 60$  cells in radial direction was employed. The grid was refined towards the jet outer diameter and towards the inlet, which results in approximately 20 cells located in the fuel jet region. The grid is depicted in Fig. 19 on top of the contour plot of the absolute velocity field magnitude. In average, approximately 25 particles per cell were employed and a particle number control algorithm was applied. Furthermore, local particle time stepping was used (see Muradoglu and Pope [50]). For more algorithmic details of the PDF method used here see section 4.3.1 and also Jenny et al. [36].

First, simulation results of the Sandia flame E are presented. Model parameter studies for  $\alpha$  and  $C_\chi$  were conducted at the beginning and revealed optimal values of 40 and 5, respectively. Only results with these optimal values are shown here, since the goal of this study is to demonstrate the concept of the new combustion modeling approach.

The hydrodynamic flow field comparison is shown in Figs. 20, 21 and 22. Note that experimental data for the flow field of the Sandia flame E are only available at downstream positions  $15 \times D_j$  and  $45 \times D_j$ . The jet spreading farther downstream and the Reynolds

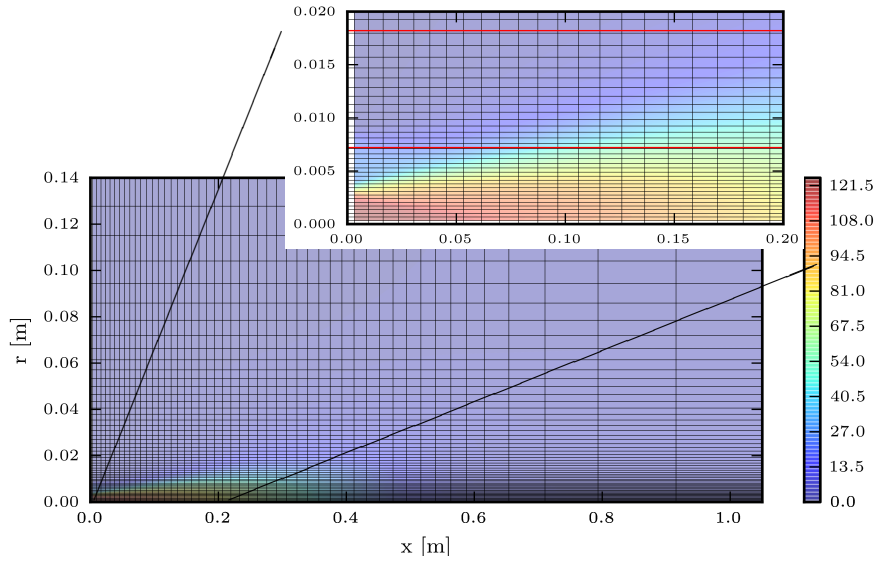


Figure 19: Employed grid for the simulations of Sandia flames E and F. The underlying contour plot depicts the absolute magnitude of the velocity field of the Sandia flame F simulation. The two red lines in the zoomed box are the boundaries of the fuel jet and the pilot burner, respectively.

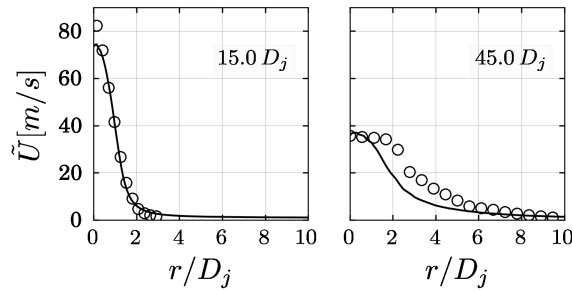


Figure 20: Sandia flame E: radial Favre averaged downstream velocity profiles at different axial locations. Symbols represent the experimental data and the lines are numerical solutions.

stresses at position  $15 \times D_j$  are both underpredicted. The underestimation of the Reynolds stresses close to the burner exit has been observed consistently in different jet calculations. Figs. 23, 24, 25 and 26 show radial profiles of the mixture fraction and temperature mean and root mean square (rms) values at different downstream positions. Mean mixture fraction and mean temperature are captured quite well; only a slight overshoot of the peak temperature at positions  $30 \times D_j$  and  $60 \times D_j$  is observed. A good match is obtained for the rms of mixture fraction and the temperature. Note that this quantity is very important for the calculation of minor species, e.g.  $NO_x$ .

The scatter plots in Fig. 27 show the particle distributions in the  $Z$ - $T$ -space at different

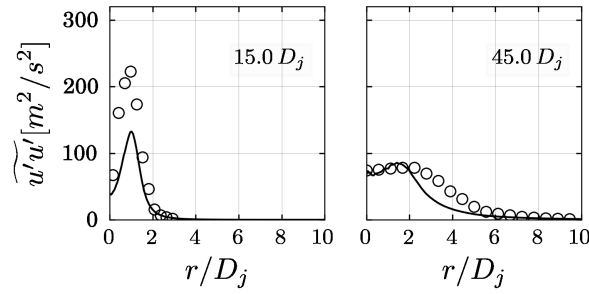


Figure 21: Sandia flame E: radial Reynolds stress profiles in downstream direction at different axial locations. Symbols represent the experimental data and the lines are numerical solutions.

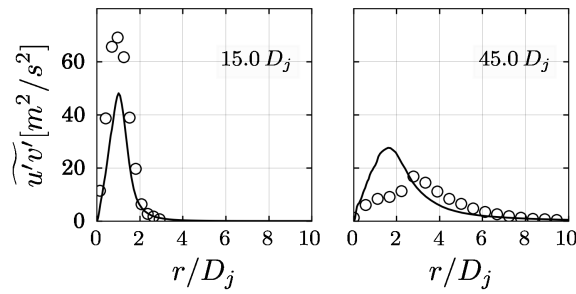


Figure 22: Sandia flame E: radial  $u$ - $v$ -Reynolds stress (axial-radial direction) profiles at different axial locations. Symbols represent the experimental data and the lines are numerical solutions.

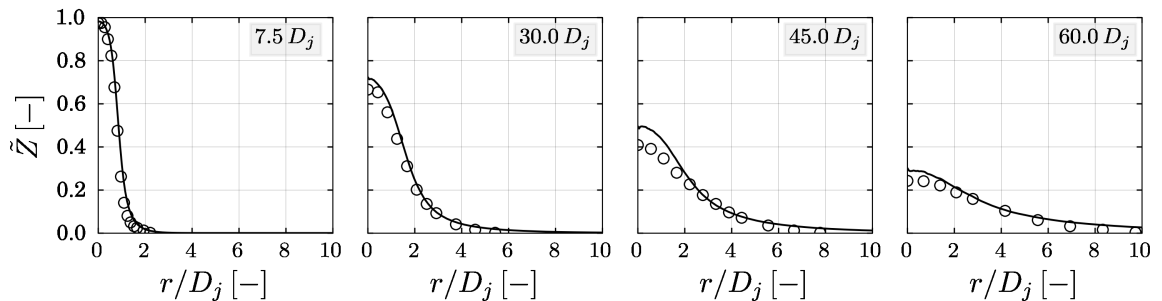


Figure 23: Sandia flame E: radial Favre averaged mixture fraction profiles at different axial locations. Symbols represent the experimental data and the lines are numerical solutions.

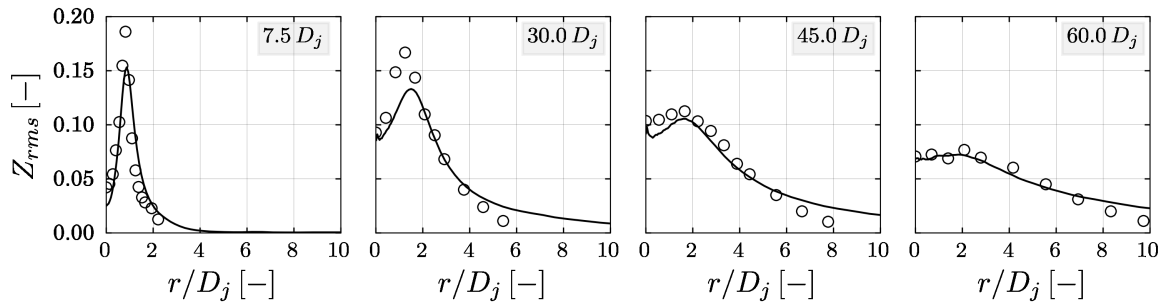


Figure 24: Sandia flame E: radial root mean square (rms) mixture fraction profiles at different axial locations. Symbols represent the experimental data and the lines are numerical solutions.

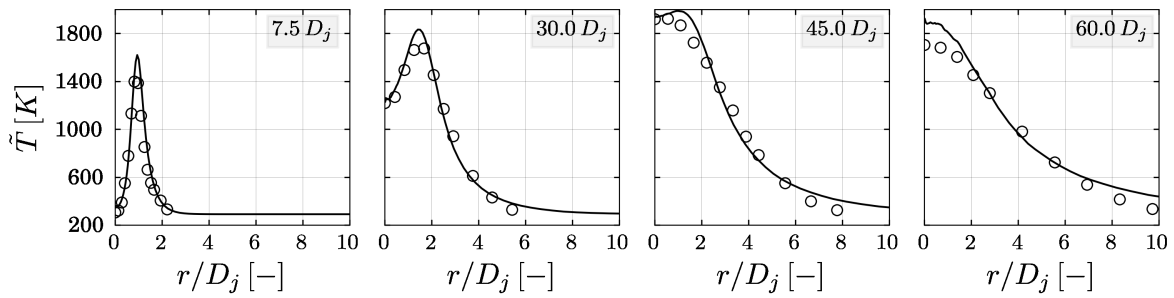


Figure 25: Sandia flame E: radial Favre averaged temperature profiles at different axial locations. Symbols represent the experimental data and the lines are numerical solutions.

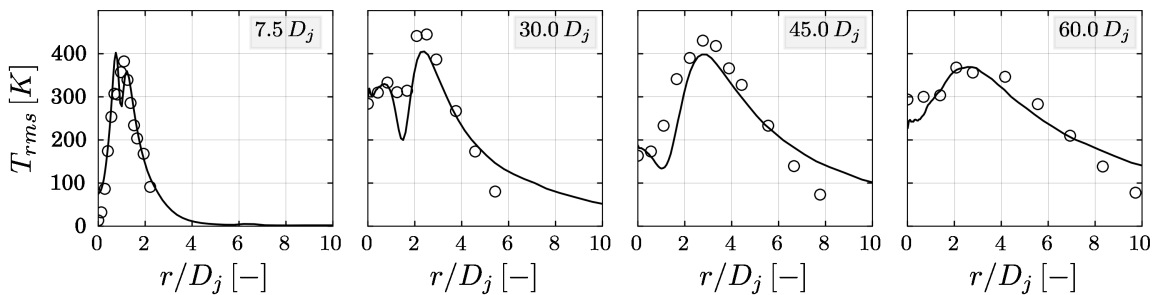


Figure 26: Sandia flame E: radial root mean square (rms) temperature profiles at different axial locations. Symbols represent the experimental data and the lines are numerical solutions.

downstream locations. On the left side are the experimental data and on the right side the

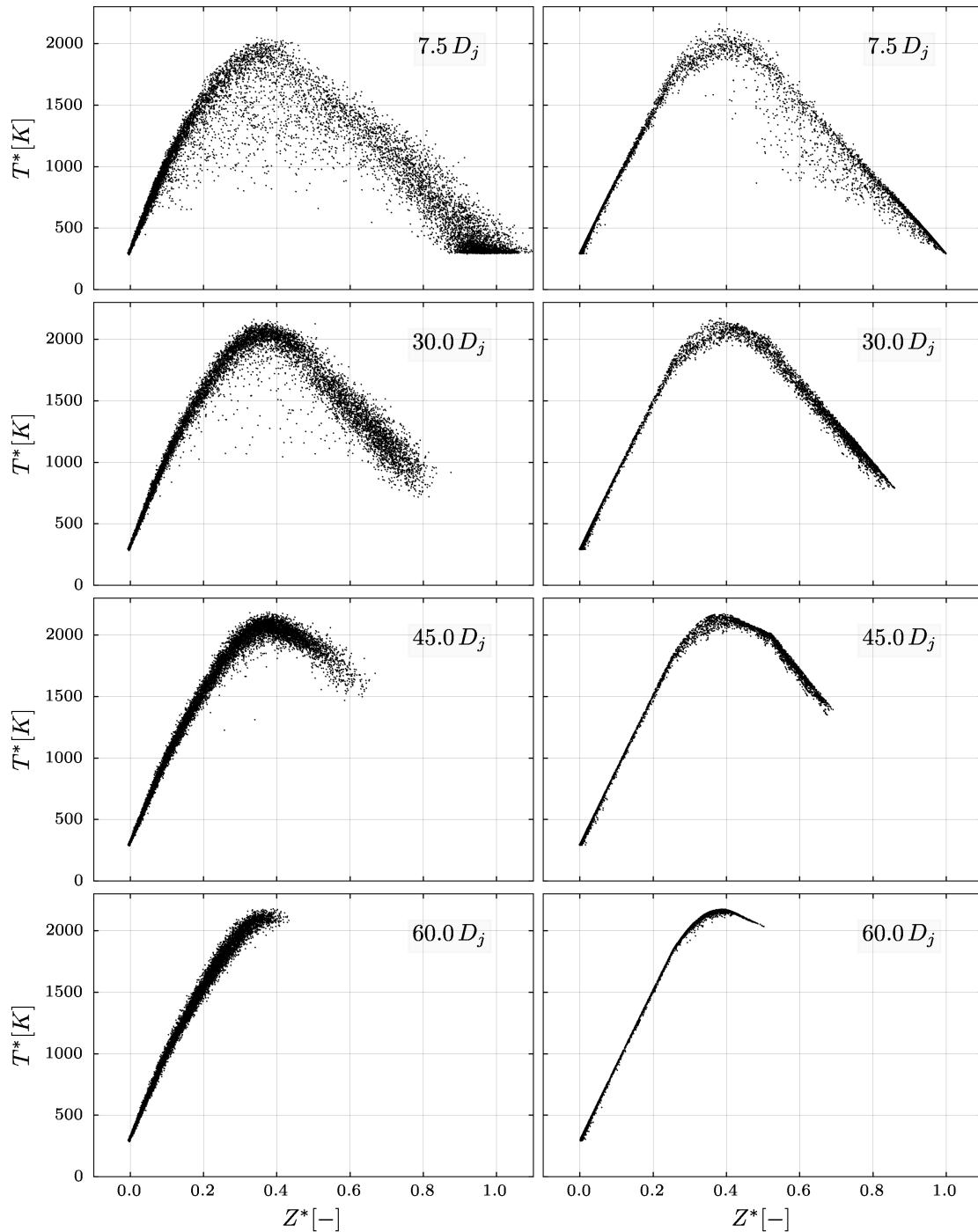


Figure 27: Sandia flame E: scatter plots in  $Z$ - $T$ -space at different axial locations; left are the experimental data and right the simulation results.

simulations results. Some of the larger variance in the experimental scatter data might be attributed to measurement inaccuracies. For example, mixture fraction values larger than

one can be observed, which is not possible by definition. Apart from that, the mixture fraction range is captured well and the overall agreement between calculated and measured data is good.

The parameter study for the Sandia flame F yielded the optimal value 10 for both  $\alpha$  and  $C_\chi$ .

First, in Figs. 28, 29 and 30 the flow field solution is shown in comparison with the experimental measurements. The agreement is reasonable; only, as observed for flame E, the

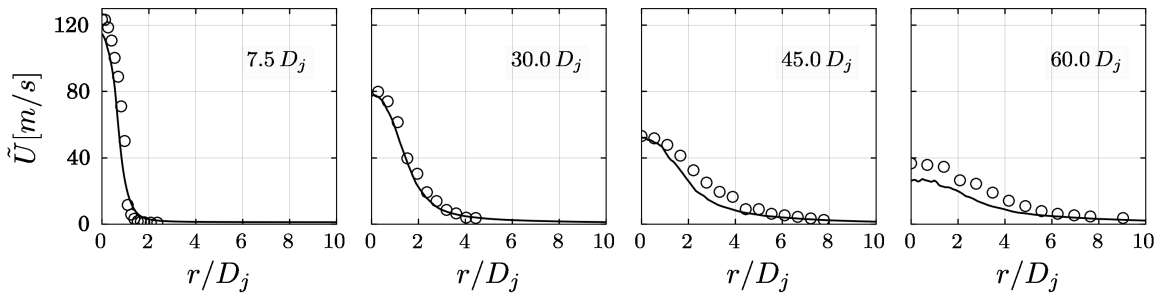


Figure 28: Sandia flame F: radial Favre averaged downstream velocity profiles at different axial locations. Symbols represent the experimental data and the lines are numerical solutions.

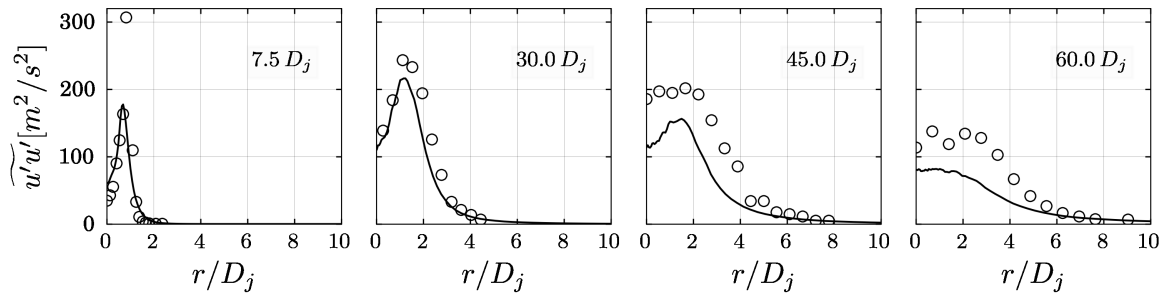


Figure 29: Sandia flame F: radial Reynolds stress profiles in downstream direction at different axial locations. Symbols represent the experimental data and the lines are numerical solutions.

Reynolds stresses closer to the burner exit are underpredicted.

The comparison of the mixture fraction and temperature statistics with the experimental data is shown in Figs. 31, 32, 33 and 34. The higher degree of local extinction at position  $7.5 \times D_j$  is captured well in the calculation and can be observed by the lower mean temperature at that position in Fig. 33. Also the second moments of mixture fraction and temperature are reproduced well (see Figs. 32 and 34), only at position  $30 \times D_j$  a larger deviation of the rms temperature from the experimental data occurs. The strong local minimum in the simulation result at  $r/D_j \approx 1.7$  is only very weakly observable in the experiment. The local minimum is created by the development of the gradient  $d\tilde{T}/dr$ ,

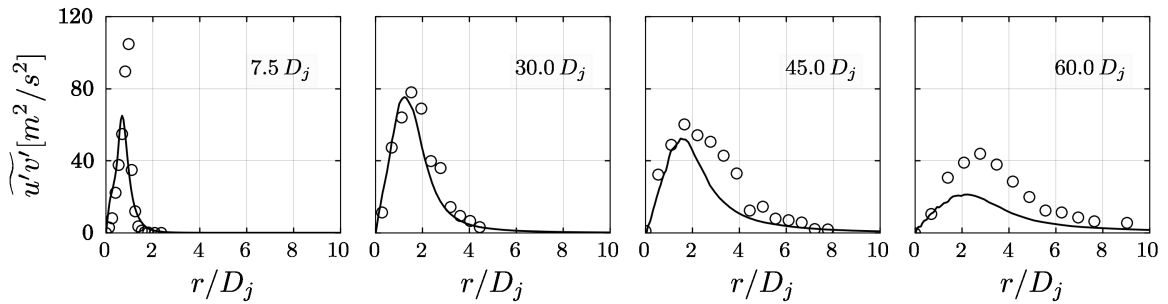


Figure 30: Sandia flame F: radial  $u$ - $v$ -Reynolds stress (axial-radial direction) profiles at different axial locations. Symbols represent the experimental data and the lines are numerical solutions.

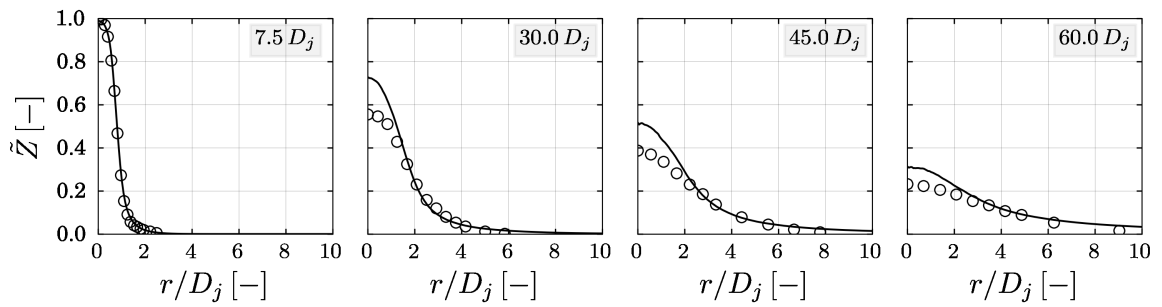


Figure 31: Sandia flame F: radial Favre averaged mixture fraction profiles at different axial locations. Symbols represent the experimental data and the lines are numerical solutions.

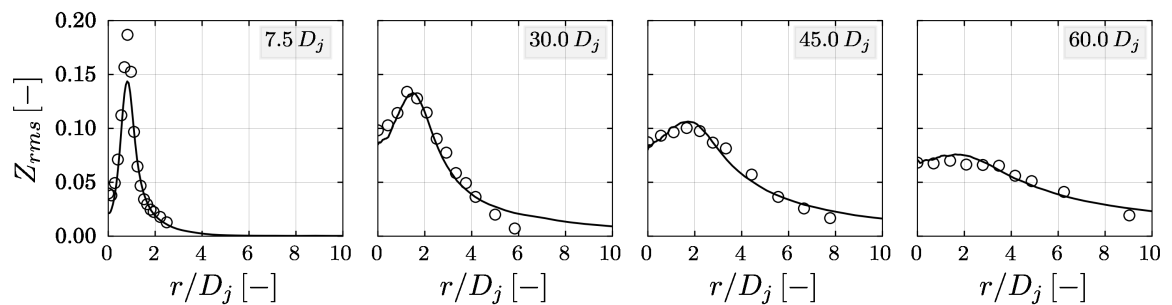


Figure 32: Sandia flame F: radial root mean square (rms) mixture fraction profiles at different axial locations. Symbols represent the experimental data and the lines are numerical solutions.

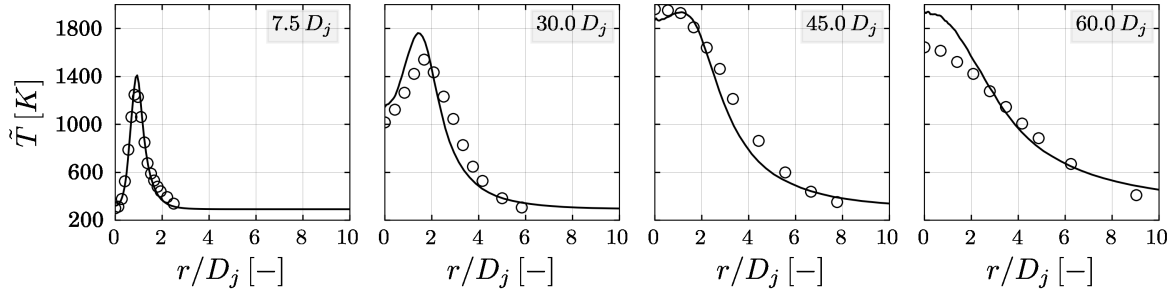


Figure 33: Sandia flame F: radial Favre averaged temperature profiles at different axial locations. Symbols represent the experimental data and the lines are numerical solutions.

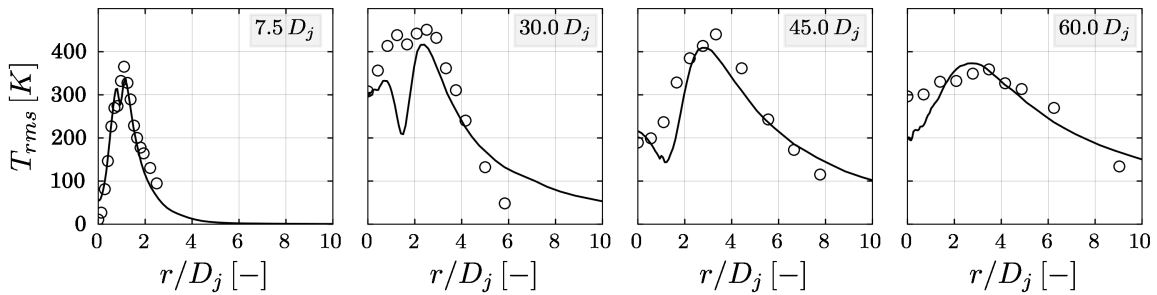


Figure 34: Sandia flame F: radial root mean square (rms) temperature profiles at different axial locations. Symbols represent the experimental data and the lines are numerical solutions.

which drives the production of temperature fluctuations. Left of  $r/D_j \approx 1.7$  (see Fig. 33) the gradient is positive and becomes negative on the right side. Therefore, in between a local minimum is expected. That it is too distinct could be that the radial turbulent transport is underpredicted in the simulation. However, the same is not observed in the  $\tilde{Z}$  and  $Z_{rms}$  profiles, which suggests that the  $T_{rms}$ -minimum originates from an artifact of the combustion model. More investigations are needed to further clarify this point.

Some artificial structures are visible in the scatter data (see Fig. 35), which originate very likely from the construction of the particle paths in the  $Z$ - $h$ -space as described in section 8.2.1 and from some unphysical behavior of the IEM mixing model. It would be quite easy to obtain a better particle distribution in  $Z$ - $T$ -space by increasing the model parameter  $C_\chi$ . This would lead to a higher level of the scalar dissipation rate and finally to more extinct particles. However, tests revealed that a higher degree of local extinction results in too low mean temperature peaks, especially at downstream positions  $x = 7.5D_j$  and  $30D_j$ . Therefore, we think that the problem lies more in the very simple model for the scalar dissipation rate (and at the end also of the mixing model of course). Here, we expect major improvements by using more sophisticated mixing models, which supposedly also yield to a much better scalar dissipation rate statistics.

A further very rigorous validation for flame F was performed by comparing mixture fraction-temperature joint PDFs and marginal mixture fraction and temperature PDFs at different



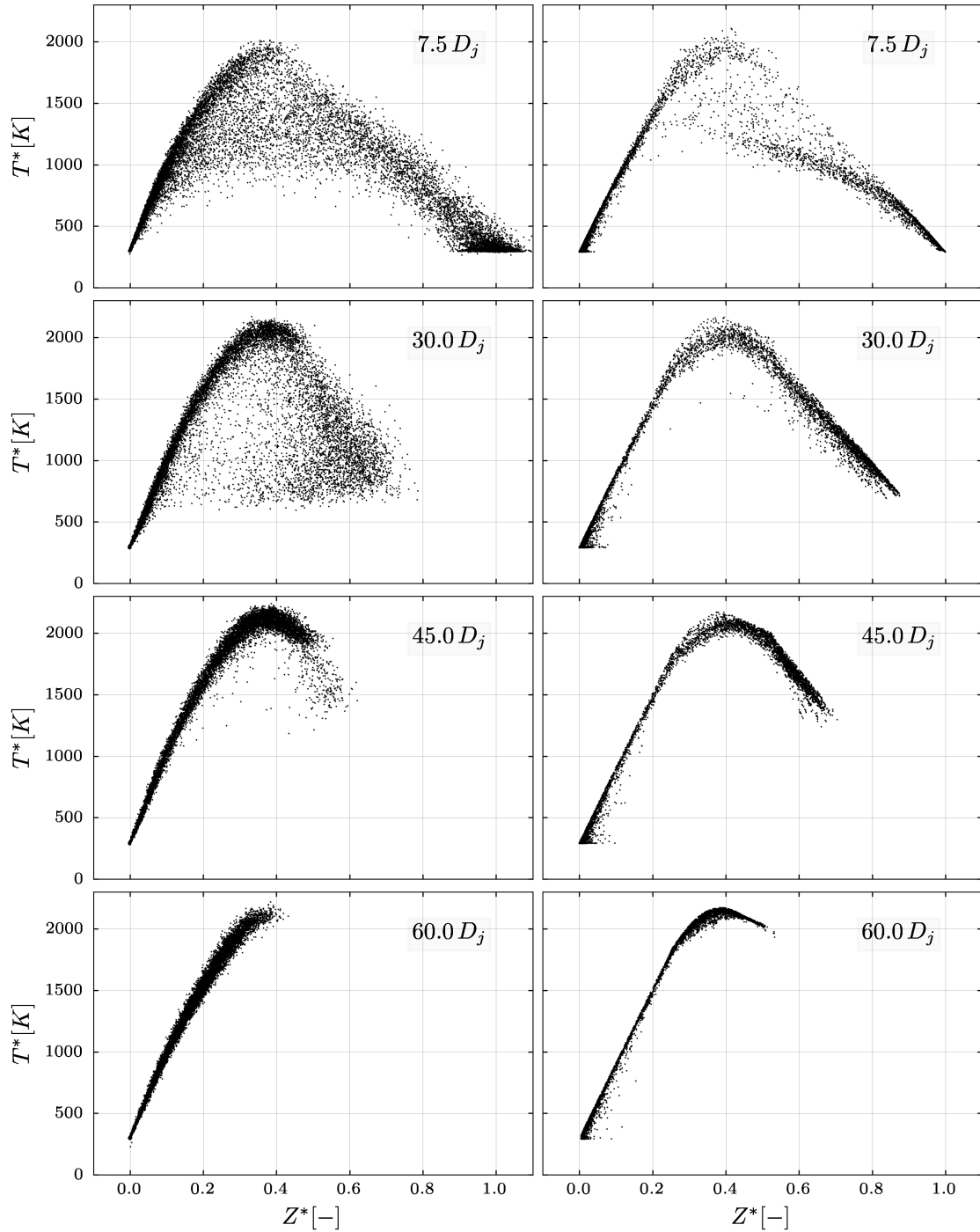


Figure 35: Sandia flame F: scatter plots in  $Z$ - $T$ -space at different axial locations; left are the experimental data and right the simulation results.

physical locations. Those locations in the flow domain are indicated in Fig. 36.

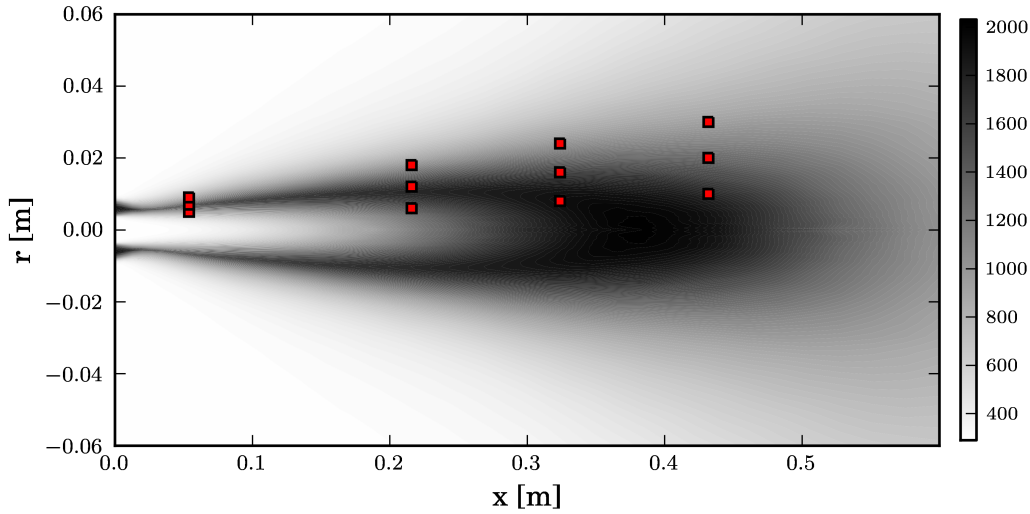


Figure 36: Temperature contour plot of Sandia flame F. The marked points are the locations, where the joint  $Z$ - $T$ -PDFs of experiment and calculation are extracted.

The extraction was done by dividing the accessed  $Z$ - $T$ -space into  $10 \times 10$  even spaced bins and both, the experimental and the computed scatter data were sampled. Note that for the sampling of the simulation data a small range in physical space must be defined in order to collect enough particles (realizations). Caution is advised here that effectively the same PDFs are extracted from experimental and calculated data. The scatter data of the experiment consist of consecutive measurements at the same location and it can be assumed that each single measurement is an average over equally sized fluid volumes. Therefore each value (or sample) contributes with the same weight to the PDF. In the calculations we deal with notional particles, which have a certain statistical and physical weight  $m^*$ . With the weight and the fluid density at the particle location, calculated via the particle energy and the ideal gas law, the representative particle volume is determined. During the sampling of the calculated data, each particle is weighted by its volume and finally, it was ensured that all extracted PDFs fulfill the normalization condition. In Figs. 37, 38, 39 and 40, the extracted and normalized mixture fraction - temperature joint PDFs are depicted. The general qualitative agreement between experiment and calculation is good and justifies once more the basic model assumptions. Closer to the centerline, for instance in Fig. 37 at  $r = 5\text{mm}$  and Fig. 38 at  $r = 6\text{mm}$ , the discrepancies are larger, whereas at the other positions the match is much better. Some of the deviations close the centerline can be partially attributed to algorithmic issues which often occur in a 2 dimensional axis symmetric setup. Further downstream and further away from the centerline, where we are mainly in the co-flow region (Fig. 38 at  $r = 18\text{mm}$ , Fig. 39 at  $r = 24\text{mm}$  and Fig. 40 at  $r = 30\text{mm}$ ), the peak of the calculated PDF is very close to  $Z = 0$  compared to the experiment, where the PDF is more smeared out.

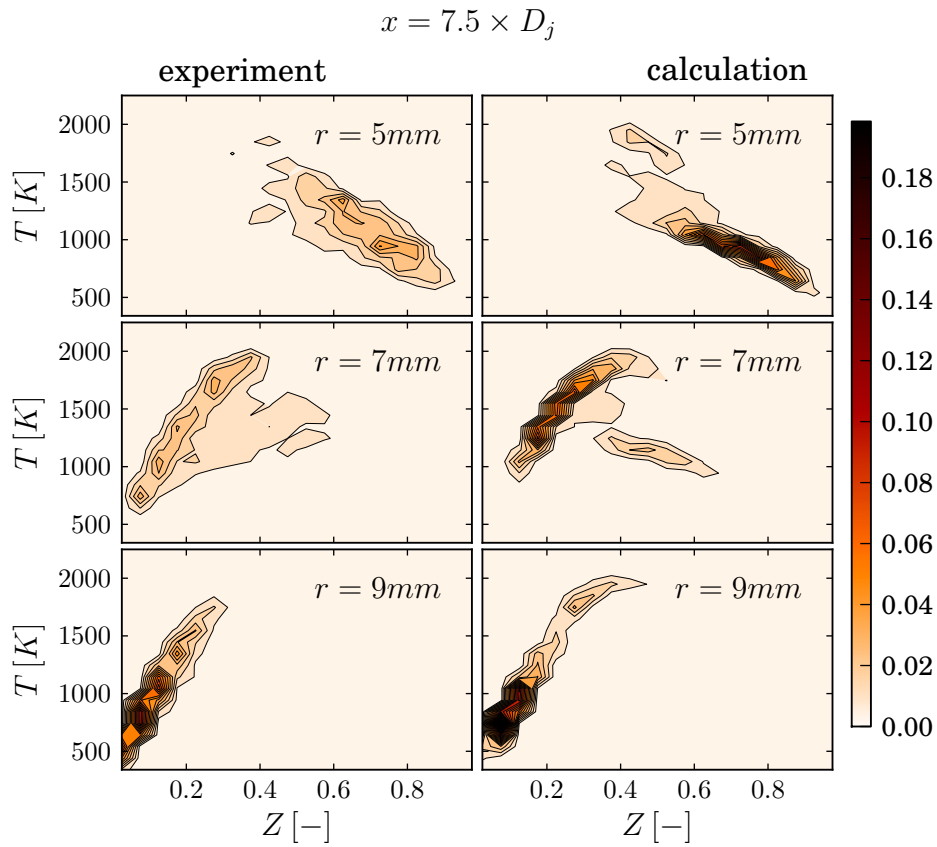


Figure 37: Sandia flame F: joint PDF of mixture fraction and temperature at downstream position  $x = 7.5 \times D_j$  and at three radial positions. On the left are the experimental and on the right side the calculated data.

Finally, the marginal mixture fraction and temperature PDFs are shown in Figs. 41, 42, 43, and 44 and in Figs. 45, 46, 47 and 48, respectively. The qualitative behavior in the mixture fraction PDFs is reproduced quite satisfactorily. The discrepancies are highest in region where the most action is going on in the flow and the flame at downstream positions  $30$  and  $45D_j$ . The agreement is less good for the temperature PDFs, which can be expected since here the uncertainties from the combustion model are directly seen. Nevertheless, the trends are captured correctly for most of the shown locations, at some position there is even a good quantitative match.

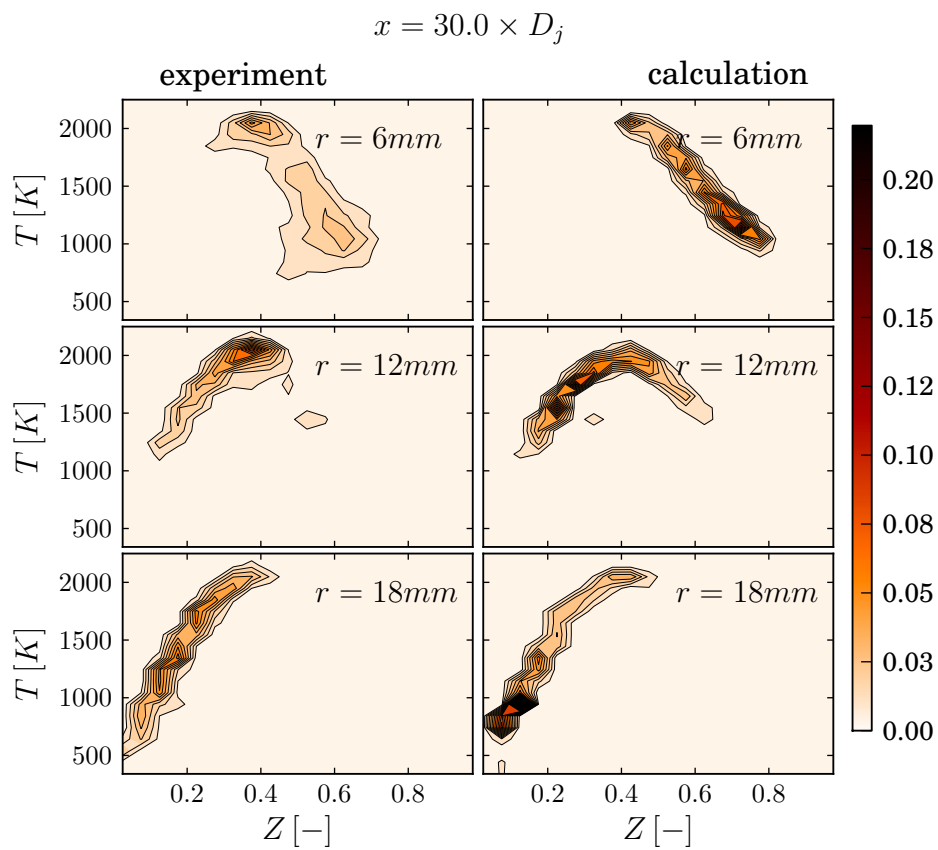


Figure 38: Sandia flame F: joint PDF of mixture fraction and temperature at downstream position  $x = 30 \times D_j$  and at three radial positions. On the left are the experimental and on the right side the calculated data.

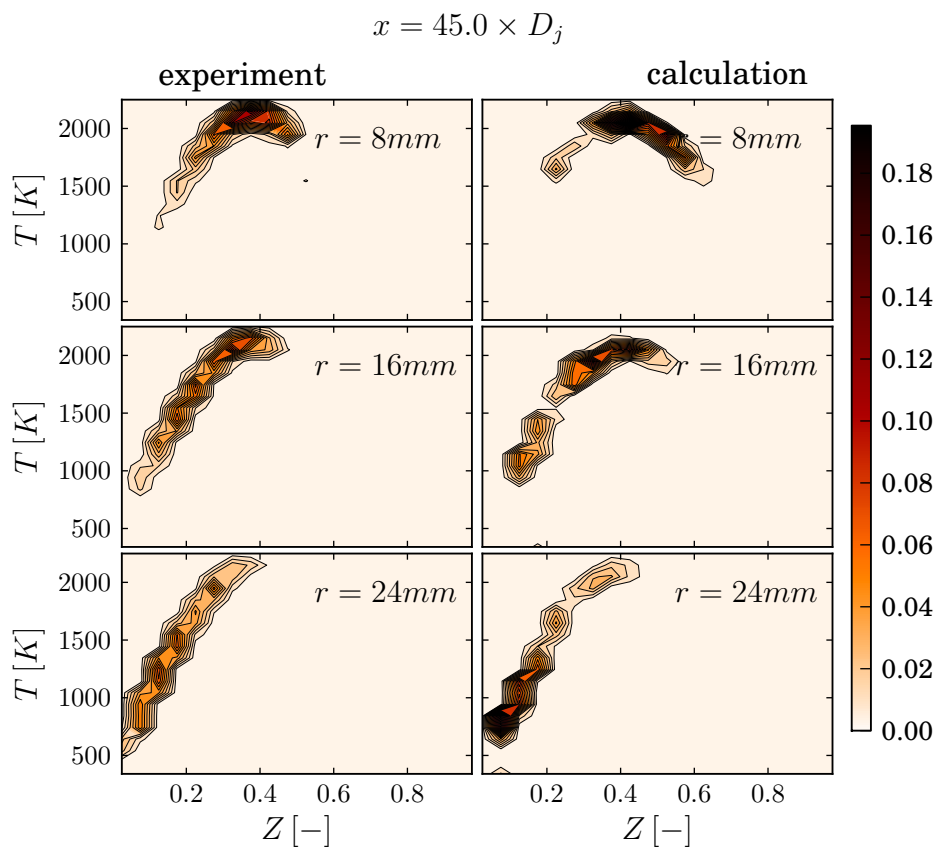


Figure 39: Sandia flame F: joint PDF of mixture fraction and temperature at downstream position  $x = 45 \times D_j$  and at three radial positions. On the left are the experimental and on the right side the calculated data.

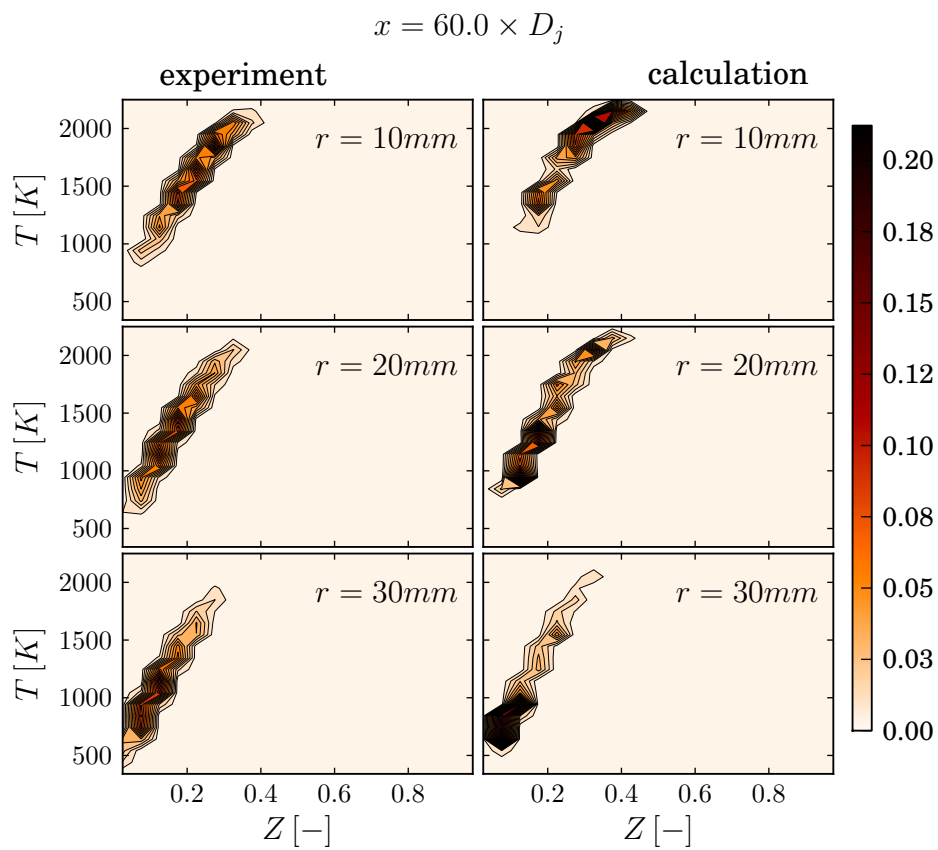


Figure 40: Sandia flame F: joint PDF of mixture fraction and temperature at downstream position  $x = 60 \times D_j$  and at three radial positions. On the left are the experimental and on the right side the calculated data.

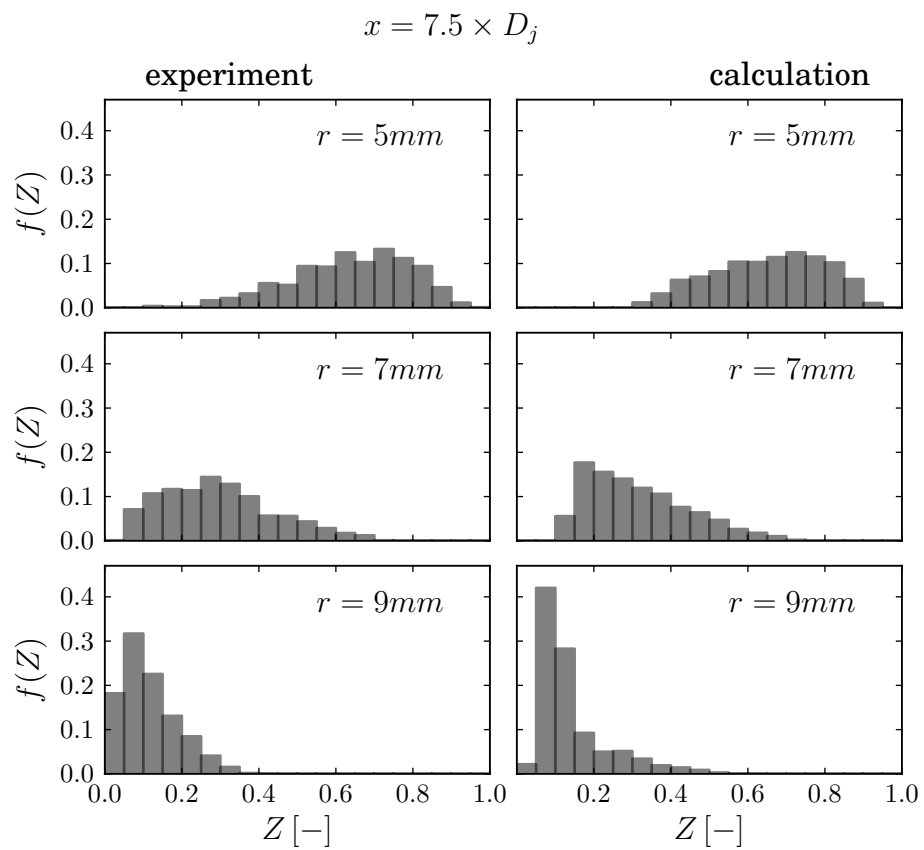


Figure 41: Sandia flame F: marginal mixture fraction PDF  $f(Z)$  at downstream position  $x = 7.5 \times D_j$  and at three radial positions. On the left are the experimental and on the right side the calculated data.

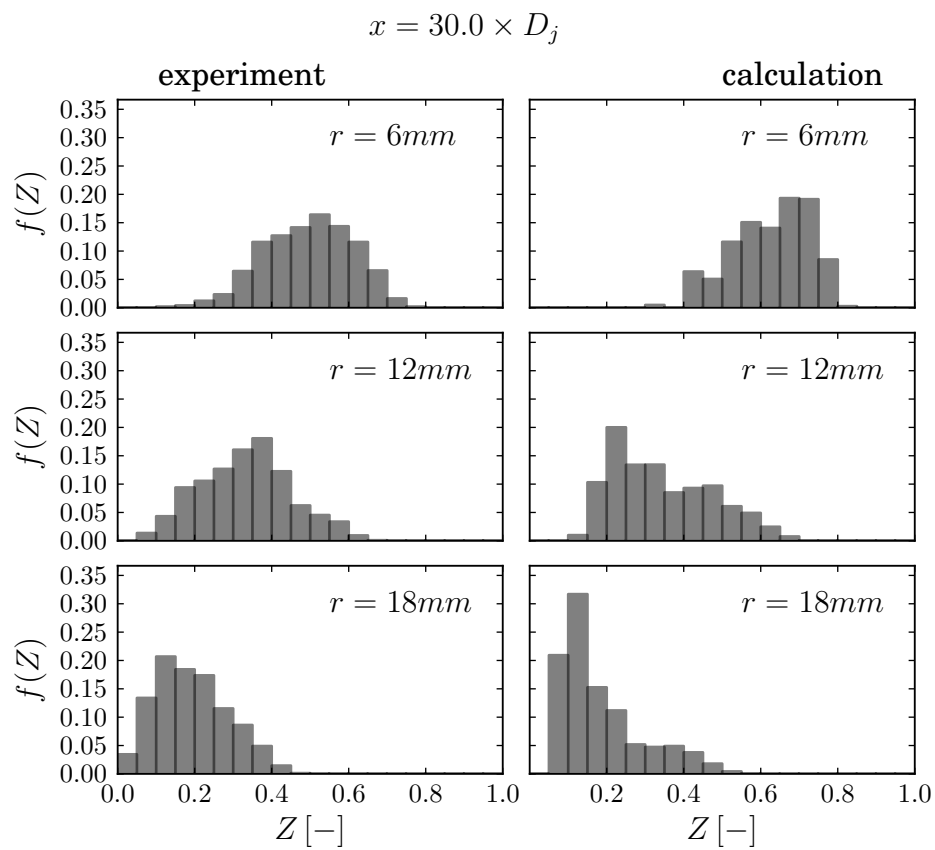


Figure 42: Sandia flame F: marginal mixture fraction PDF  $f(Z)$  at downstream position  $x = 30 \times D_j$  and at three radial positions. On the left are the experimental and on the right side the calculated data.



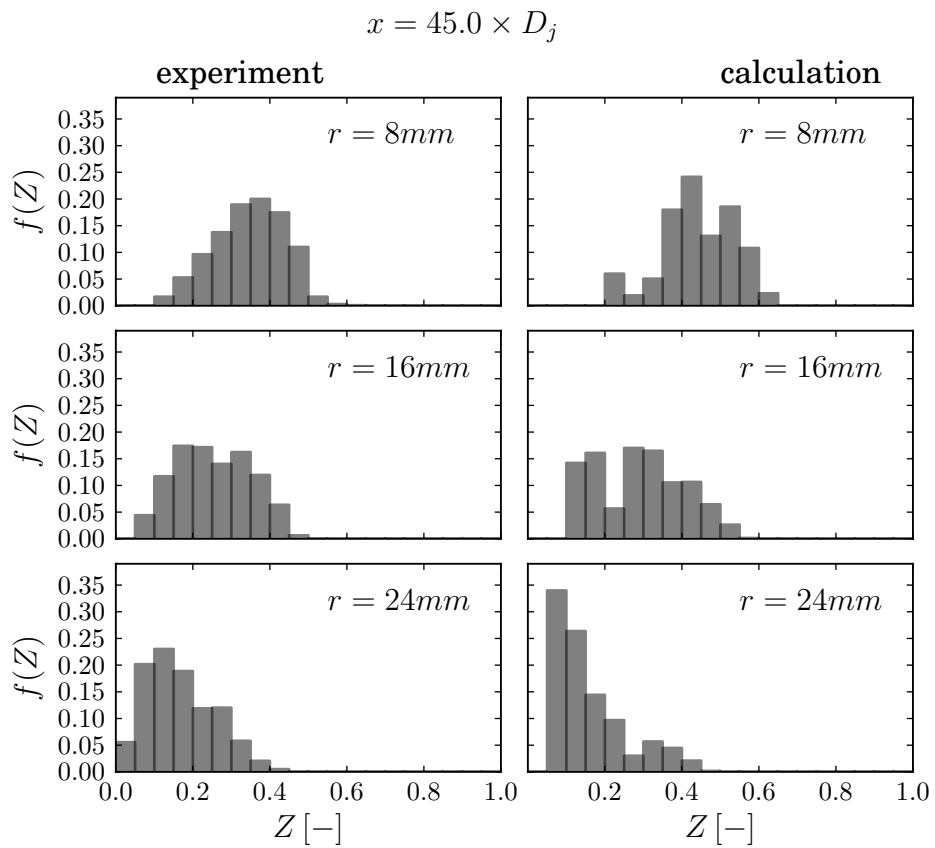


Figure 43: Sandia flame F: marginal mixture fraction PDF  $f(Z)$  at downstream position  $x = 45 \times D_j$  and at three radial positions. On the left are the experimental and on the right side the calculated data.

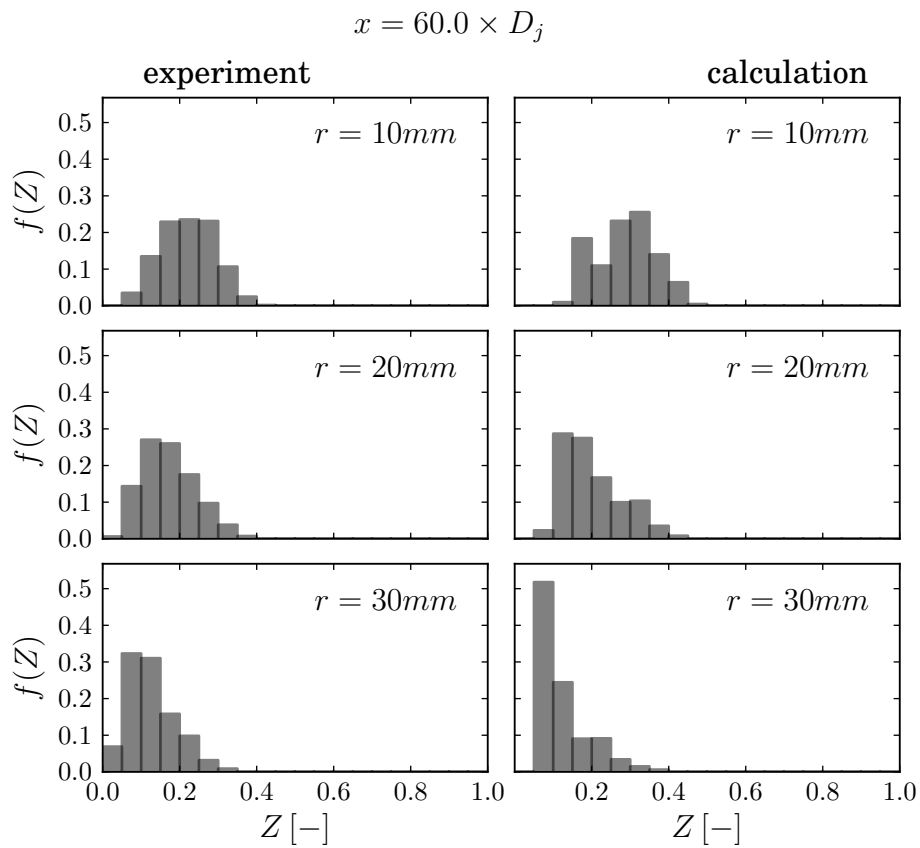


Figure 44: Sandia flame F: marginal mixture fraction PDF  $f(Z)$  at downstream position  $x = 60 \times D_j$  and at three radial positions. On the left are the experimental and on the right side the calculated data.

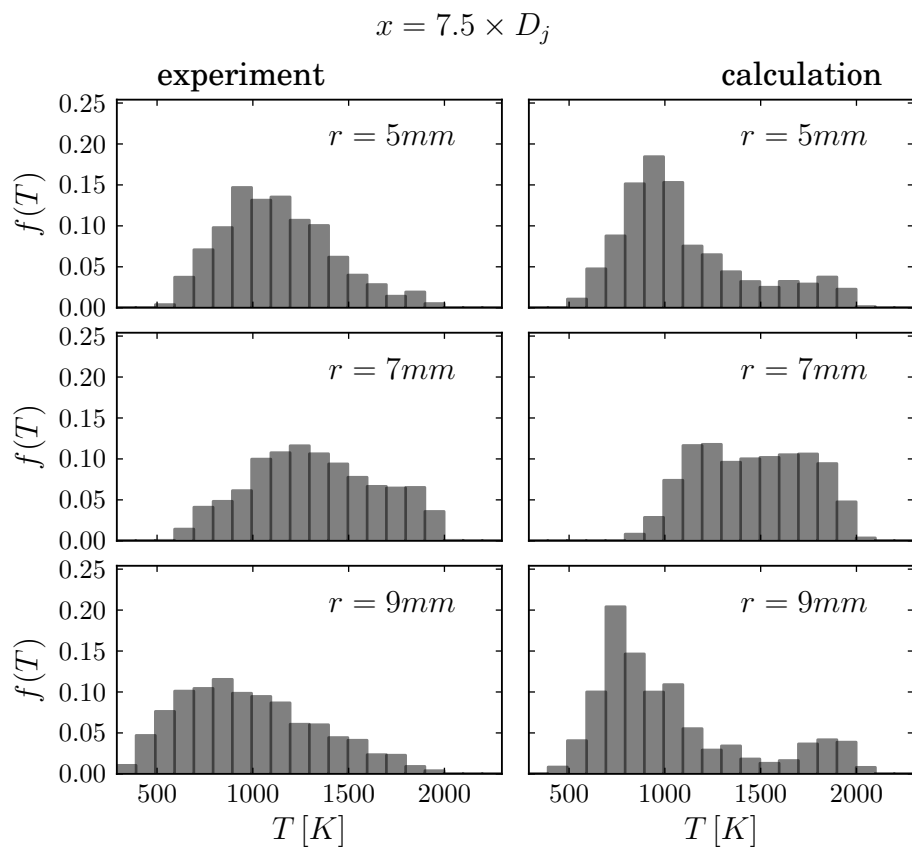


Figure 45: Sandia flame F: marginal temperature PDF  $f(T)$  at downstream position  $x = 7.5 \times D_j$  and at three radial positions. On the left are the experimental and on the right side the calculated data.

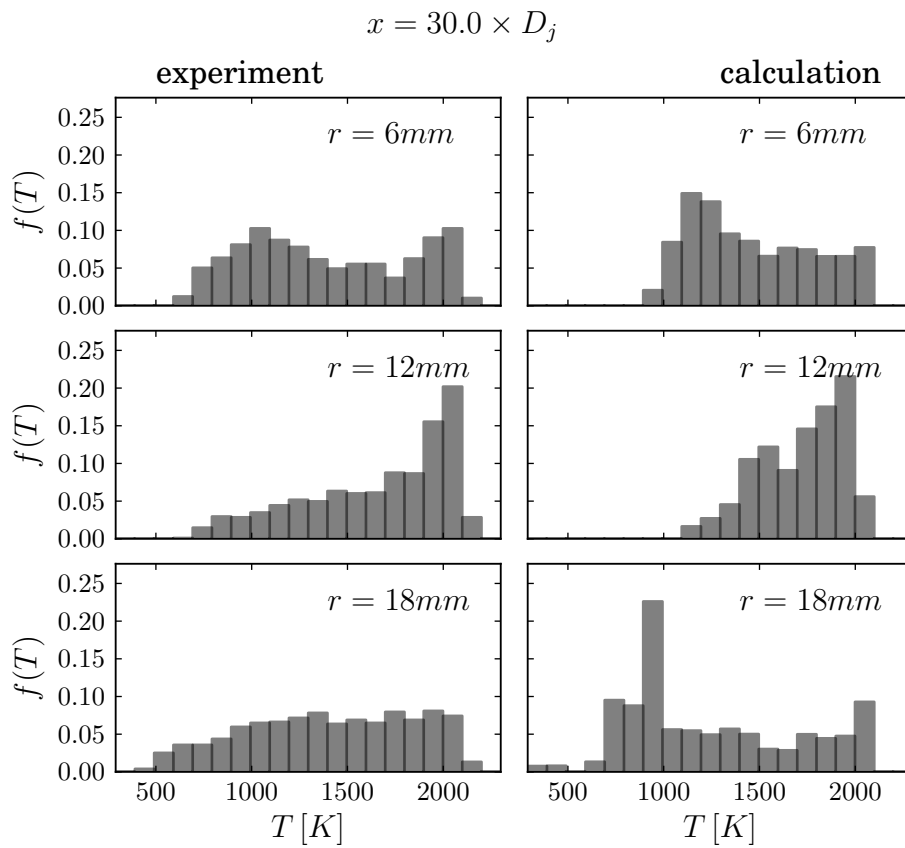


Figure 46: Sandia flame F: marginal temperature PDF  $f(T)$  at downstream position  $x = 30 \times D_j$  and at three radial positions. On the left are the experimental and on the right side the calculated data.

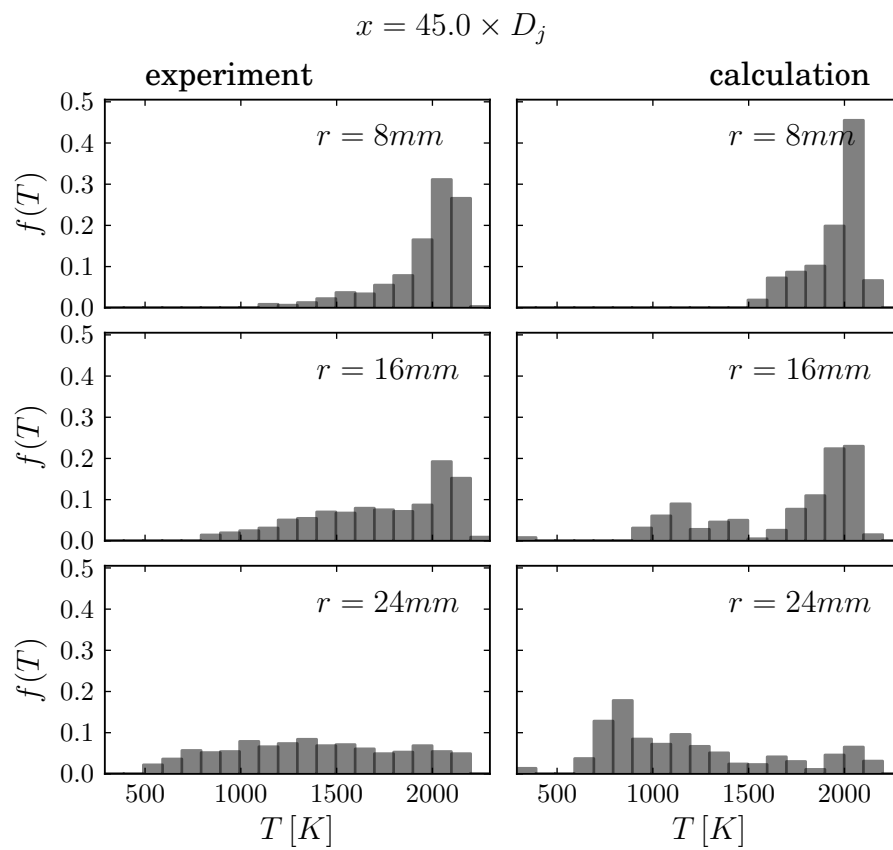


Figure 47: Sandia flame F: marginal temperature PDF  $f(T)$  at downstream position  $x = 45 \times D_j$  and at three radial positions. On the left are the experimental and on the right side the calculated data.

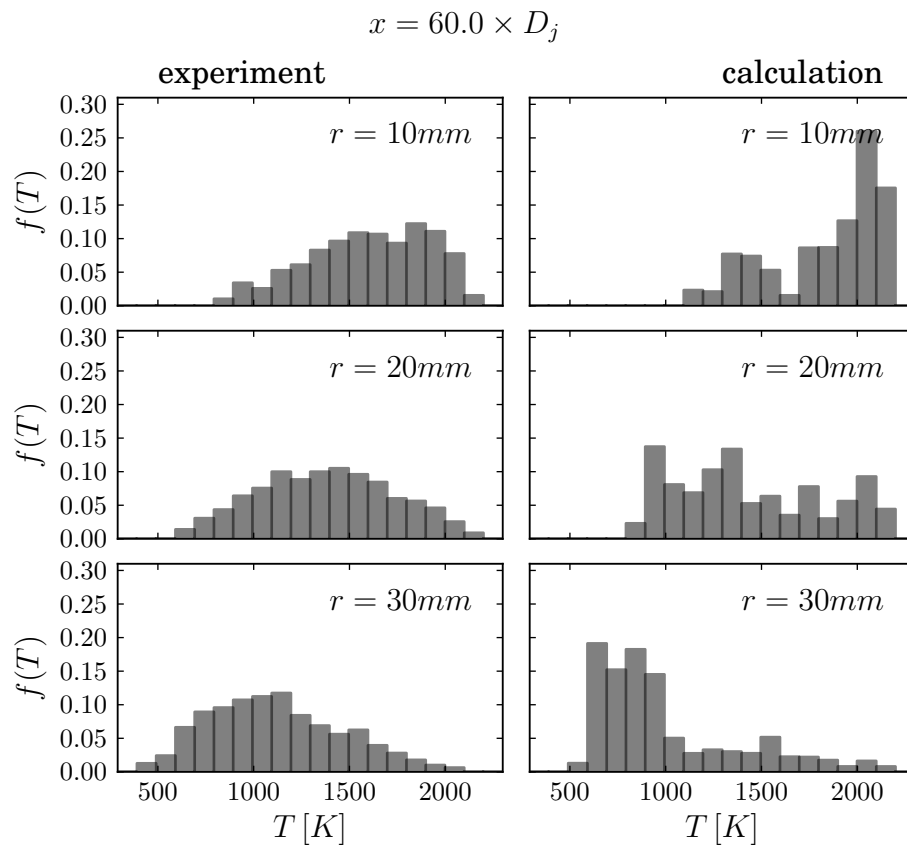


Figure 48: Sandia flame F: marginal temperature PDF  $f(T)$  at downstream position  $x = 60 \times D_j$  and at three radial positions. On the left are the experimental and on the right side the calculated data.

## 8.4 Conclusions

In this chapter, a novel modeling framework for partially premixed combustion is presented. It is based on a PDF algorithm combined with a reactive mixing model and a progress variable. The reactive mixing model is an approach to describe appropriate particle paths in mixture fraction-enthalpy space, which are fundamentally different in partially premixed flames compared to diffusion flames without local extinction. An other ingredient of the new approach is a model for the scalar dissipation rate.

The main model parameters are  $\alpha$  and  $C_\chi$ , which are used to model the ignition probability and the scalar dissipation rate, respectively. Here, in a first approach constant values were chosen for these two parameters but this proved not to be universal. Parameter studies were performed in order to find the optimal values of the model constants for the two investigated test cases. The results of this study confirm the a priori assumption that an increase of  $\alpha$  leads to faster ignition of the particles and thus the flame shifts towards the inlet nozzle. In the limit of  $\alpha \rightarrow \infty$ , the steady flamelet approach is recovered. The model constant  $C_\chi$  directly determines the amount of extinction in regions with high scalar dissipation rate. These regions are primarily located in the shear layer between the jet and the pilot streams. Scatter plots confirm that there exist more extinct particles near a mixture fraction of one, if  $C_\chi$  is increased.

The model was applied to simulate two piloted jet flames, i.e. the Sandia flames E and F. Both flames depict a considerable amount of local extinction, whereas flame F is close to global extinction. The results give confidence that the PDF method together with the new combustion model has the ability to account for the effects in partially premixed flames and comparisons with experimental data shows good agreement for the first two statistical moments of temperature and mixture fraction. However, the scatter plots reveal some discrepancies in the higher statistical moments, showing the limitations of this model. We believe these limitations can be overcome by using more elaborated ingredients for the single model components. Questionable for instance is the IEM mixing model, which is known to evolve a scalar PDF not really physically, since it is purely deterministic and does not change the shape of the initial scalar PDF. The behavior of the mixture fraction PDF is also crucial for the scalar dissipation rate statistics and is assumed not to be very accurate in the case here. Using a more sophisticated mixing model as e.g. the parameterized scalar profile (PSP) mixing model by Meyer and Jenny [46] and [45] may help to overcome these shortcomings. Meyer showed with rigorous test cases that the PSP model very accurately describes the evolution of the scalar, the scalar dissipation rate and their joint PDF.

Another desirable improvement concerns the constructed particle paths. As described in the result section, there are artificial effects visible in the scatter data, which evidently originate from the constructed particle paths. One approach could be to adopt the basic assumption from the PSP model of a statistical representation of the mixture field by scalar profiles. Here however, the profile shape of reactive scalars must be modified due to the chemical reactions. Similarly as in the described reactive IEM mixing model, the particles must evolve on curved paths in mixture fraction-enthalpy space.

Further potential improvement is concerned with the modeling of the progress variable source term. If the physical picture of embedded laminar edge flames is considered, then

this source term must take into account the propagation of turbulent flame fronts, which consist of such laminar triple flames. DNS studies of laminar partially premixed triple flames for different strain rates would be necessary to obtain the laminar flame speed. See the next subsection 8.5 for a more detailed explanation about this topic.

Finally it can be concluded that the new combustion model contains the required mechanisms to deal with partially premixed flames, but further model improvements and fine tuning are required to make it more general and reliable.

## 8.5 Extension: 2D Laminar Flame Tables

In subsection 8.1 we introduced the fine scale picture of laminar triple flames, which are embedded in the partially premixed turbulent flow field. However, the presented simulations were done using common stationary one dimensional flamelets. Here, the idea of including the structure of laminar triple flames is explained in more detail.

The main assumption in the flamelet approach is that a turbulent diffusion flame consists of an assembly of embedded laminar diffusion flame sheets. These laminar flame sheets are computed by solving the reaction-diffusion equation in mixture fraction space [58]. The underlying physical setup is a 1D physical domain with fixed boundary conditions; fuel stream condition on one side and oxidizer stream condition on the other side. Between the boundaries near the point of stoichiometric mixture, a diffusion flame gets established. Oxidizer and fuel are transported by diffusion towards the reaction zone and the heat produced in the flame is transported away from the reaction zone. The scalar dissipation rate depends on the physical width of the domain, i.e. the narrower the domain the higher the scalar dissipation rate. This situation is depicted in Fig. 49. Instead of this one-dimensional fine scale picture, two-dimensional triple (edge) flames are considered for the case of partially premixed combustion. The idea is motivated by DNS data of Domingo and Vervisch [21] of an igniting laminar partially premixed mixture field, where such flame structures are clearly observable. Fig. 50 shows a sketch of such triple flames, which are able to propagate into the unburnt reactive mixture; similar as premixed flames. The propagation ability is an important feature, since taking for instance the case of lifted jet flames, this is considered as one of the flame stabilization mechanisms (see subsections 7.2.1 on page 60 and 7.2.2 on page 61). In our approach, the propagation mechanism is modeled by the progress variable approach described in sec. 8.2.2 (page 68).

To account for such embedded laminar triple flames in numerical turbulent flame simulations, they are computed in a preprocessing step and stored in so called flame tables. A rectangular two dimensional domain in physical space is considered with Dirichlet boundary conditions on both sides, i.e. fuel conditions ( $Z = 1$ ) on one side and oxidizer conditions ( $Z = 0$ ) on the other side. Slip boundary conditions for the velocity are applied at both sides (see Fig. 51). At the inflow boundary, a laminar uniform flow with a linear mixture fraction distribution is imposed. The scalar dissipation rate is proportional to  $1/L_y^2$ , where



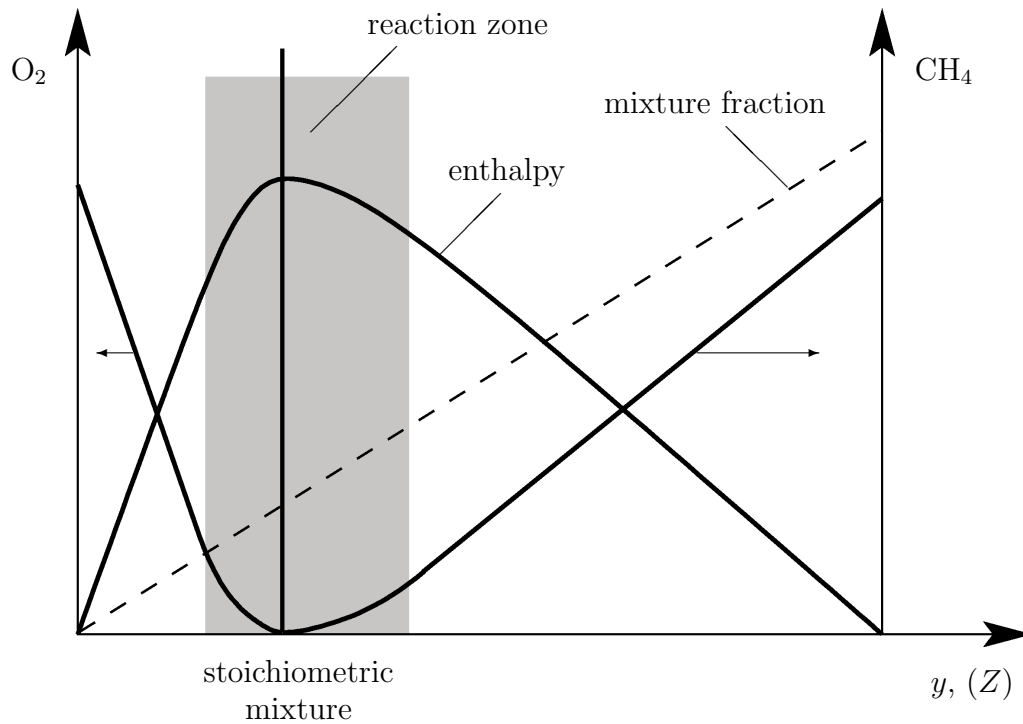


Figure 49: Sketch of a one-dimensional laminar flame sheet. Dirichlet boundary conditions are applied with pure oxidizer on the left and pure fuel on the right side. The gray shaded region indicates the main reaction zone. Outside the reaction zone pure diffusive mixing takes place. The mixture fraction is a passive scalar and hence, is not affected by the reactions.

$L_y$  is the width of the domain. Similar as for one dimensional flamelets, the scalar dissipation rate can be adjusted through the width of the domain. The inlet velocity  $U_d$  has to be controlled such that it equals the propagation speed of the triple flame to achieve a quasi steady state situation. The computational domain must be long enough, such that a fully developed diffusion flame sheet, similar to the one in the classical flamelet approach, can establish. Such calculations are performed for different scalar dissipation rates and then transformed into mixture fraction - burning time space. The burning time  $\tau_b$  is defined as the time elapsed since a particle crossed a virtual starting line. This line lies at the base of the triple flame and in the context here it coincides with the location, where the progress variable switches from zero to one. In a Lagrangian context this means as soon as the progress variable of a particle changes its state from 0 to 1, the burning time starts to run and is stored as a particle property. Note that the burning time is only used in the turbulent flame calculation and not during the preprocessing simulation.

After transformation from the physical to the  $Z$ - $\tau_b$ -space, the triple flames are stored in flame tables, which are parameterized by the mixture fraction  $Z$ , the scalar dissipation rate  $\chi$  and the burning time  $\tau_b$ . These tables then can be employed for cheap look-up

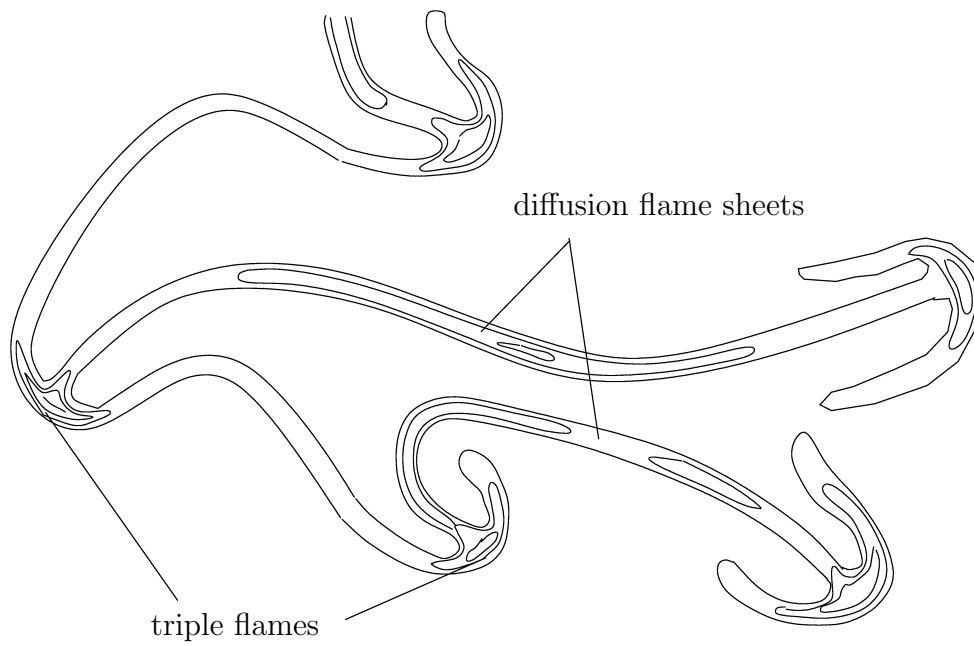


Figure 50: Sketch of a laminar igniting mixture field with characteristic triple or edge flame structures (inspired by DNS data of Domingo and Vervisch [21])

operations during subsequent PDF simulations.

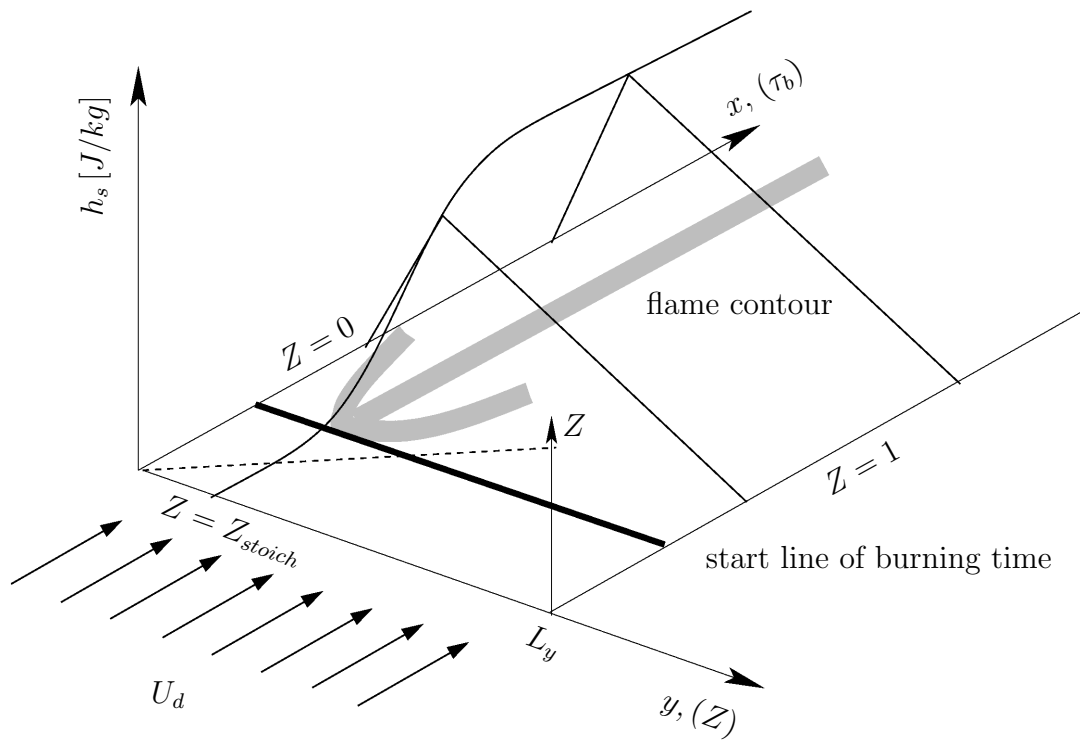


Figure 51: Setup for a laminar two dimensional triple flame calculation. The inlet flow has a uniform velocity  $U_d$  and a linear mixture distribution with pure oxidizer ( $Z = 0$ ) on the left side ( $y = 0$ ) and fuel ( $Z = 1$ ) on the right side ( $y = L_y$ ). For the tabulation the downstream direction  $x$  is mapped to the burning time space  $\tau_b$  and the  $y$ -direction into mixture fraction space  $Z$ .

## 9 Conclusions and Outlook

There are many different ways to tackle the governing equations for turbulent reactive flows. The methods can be classified by the level of closure or in other words by the extent of modeling effort. On one hand, the computational cost of a certain strategy increases with a higher closure level, but on the other hand there is a gain in accuracy.

In the case of reactive flows, one can distinguish between the closure of turbulence and the closure of chemical reaction source terms in the energy and scalar conservation equations. Often a good compromise are transported PDF methods, which lie in terms of computational cost and accuracy between the widely used RANS models with averaged scalar transport equations and LES or even DNS.

Complete PDF methods, where a transport equation for the joint PDF of velocity, turbulence frequency and compositions is solved, have the advantage that turbulent convection and the chemical source terms appear closed. Moreover, the full one point, one time joint statistics of all flow, scalar and thermodynamic properties is available and can be used to develop appropriate models for the remaining unclosed terms. This is a major advantage over RANS methods where, usually only for first and second moment statistics is solved.

The first two major contributions in the first part of this work are algorithmic and numerical improvements of transported PDF solution methods.

The reason why transported PDF methods are not more often used is mainly because of the nonstandard solution algorithms, numerical difficulties and the mathematical theory behind it. The joint PDF transport equation is defined in a high dimensional space and therefore is usually solved by particle Monte Carlo methods. The so called hybrid finite volume-particle algorithms proved to be more efficient than pure particle methods, but they introduce additional difficulties, as for instant consistency requirements between quantities which are computed in different ways, i.e. by the particle and the finite volume methods. In part I of this thesis the energy consistency issue is addressed and a new solution algorithm proposed. In hybrid methods, usually, the averaged polytropic Euler equations are solved by a finite volume scheme and the chemical reaction energy source term is extracted from the particle field. In the new approach the finite volume energy equation is abandoned completely and instead, the whole energy information is extracted from the particles and passed as thermodynamic pressure on to the momentum equation of the new Euler system. Certain requirements must be fulfilled to ensure that the new algorithm is valid; only statistically stationary solutions can be obtained, the Mach number in the fresh gas must be

small ( $\lesssim 0.3$ ), the flame speed has to be much lower than the speed of sound (deflagrations) and the Reynolds number of the flow must be high. The treatment of the finite volume inflow- and outflow boundaries needs special attention, since the behavior of the modified Euler scheme is different compared to the polytropic system.

The drawback of this new scheme is that the extracted particle energy field introduces a bias error. However, for stationary solution, the bias can be diminished by an appropriate time averaging method. Note that all combustion simulations, which are presented in part II of this thesis, were performed with the new algorithm.

The general PDF transport equation has the form of a differential Chapman-Kolmogorov equation and if it is solved with a particle method, the particles evolve consistently according to stochastic differential equations; typically in the form of Langevin equations (for continuous processes). Examples of such SDEs are the Simplified Langevin equation for modeling the turbulent velocity or the model equation for the turbulence frequency. In these model equations may appear time scales, which impose severe time step restrictions on conventional numerical integration schemes. Therefore, we developed a new time accurate integration scheme for the particle movement in physical space. The new scheme honors the single and joint statistics of the particle position and the velocity for arbitrarily large time steps. The idea behind the approach is to integrate the particle position and velocity evolution equations with the rules of Itô calculus, using the properties of the Wiener increments and expanding a stochastic term in order to increase the degree of freedom and finally adjusting the derived parameters such that the theoretically correct evolution of the first and second statistical moments is ensured. The approach was validated for a homogeneous test case and it was shown that huge errors are made with a common finite differencing integration scheme, if the time step resolution is too coarse.

In part II, a novel model for partially premixed turbulent combustion is presented. In this model we tried to combine the influences of molecular mixing and chemical reactions on the fluid. The IEM mixing model together with a flamelet approach were modified, such that they become a reactive IEM mixing model, which describes evolution paths of fluid particles in mixture fraction - enthalpy space. The reactive mixing model is only applied in a predefined flammable mixture fraction range, which is located around the point of stoichiometric mixture fraction and additionally only if the fluid element is ignited. Whether an extinct fluid element ignites depends on a progress variable, which in a Monte Carlo context means that the ignition probability for single particles has to be determined each time step. This ignition probability depends on the chemical and thermodynamic state of the particle's environment. Here, the progress variable describes the propagation of laminar triple flames embedded in a turbulent flow field, which is an adaptation for partially premixed combustion of the classical flamelet concept. It is important to note that for the new model concept, the knowledge of the joint statistics of mixture fraction, scalar dissipation rate and a progress variable is mandatory and can only be provided by transported PDF methods. Of course the quality of the joint statistics depends on the model performance itself.

It may be questioned why a combustion model is developed, despite the fact that the chemical reaction source term appears closed in the governing equation. There are mainly

two reasons: first, due to algorithmic efficiency reasons and second, even if all possible reactions are taken into account, there are still unsolved modeling issues concerning the interplay of mixing and chemical reactions.

In common methane - air combustion dozens of species and several hundreds of different reactions are involved and the smallest chemical time scales are much smaller than the Kolmogorov time scale. Direct integration of such a coupled system of equations is computationally extremely expensive. There are approaches, as for instance in situ adaptive tabulation (ISAT) of the chemical source term or pre-tabulation of the accessed species manifold and its description by a suitable set of progress variables (e.g. ILDIM- or REDIM-approaches). However, these approaches usually are computationally still much more expensive than a combustion model as it is presented here.

The issue of the interplay between mixing and reaction as well as the one between reaction and turbulence are among the most discussed topics in turbulent reactive flows and yet not fully understood. By solving the chemistry exactly, one still has to apply a mixing model for the unclosed molecular mixing term and in most solution methods the two processes are treated separately. Our approach is an attempt to combine these two processes in one model by taking physical knowledge of the interaction between mixing and reaction into account.

The new model was successfully applied to demanding test cases of turbulent lifted jet flames and proved the ability to deal with important phenomena occurring in partially premixed flames. The agreement of first and second moment statistics with experimental data is comparable to that of calculations with exact chemistry or with LES. However, comparisons of scatter data, of the mixture fraction-temperature joint PDFs and their marginal PDFs at different locations reveal that the model needs further refinements. Especially the particle paths in mixture fraction - enthalpy (temperature) space show some artifacts, which can be attributed to the simple IEM mixing model and the way the particle profiles were constructed.

Thus, using the same idea but applying a more sophisticated mixing model as for instance the PSP mixing model and more physical particle profiles, which take the nonlinearity of the chemical reactions into account, should lead to improved scalar statistics.

Furthermore, the closure of the progress variable source term, i.e. the ignition probability for a fluid particle, needs to be refined. For that it would be helpful to study in isolation the propagation of laminar and turbulent partially premixed flames and try to find correlations between propagation speed, flow and thermodynamical properties of the fresh and burnt mixtures.

Part III

## Appendices





# A Itô Calculus for Stochastic Differential Equations

Let us assume a stochastic process  $U(t)$  with a PDF  $f(V; t)$  ( $V$  is the sample space variable of  $U(t)$ ) evolves according to the general stochastic differential equation (SDE)

$$\frac{dU(t)}{dt} = a(U, t) + b(U, t) \frac{dW(t)}{dt}, \quad (\text{A.1})$$

where  $a(U, t)$  and  $b(U, t)$  are drift and diffusion coefficients, respectively and  $W(t)$  a Wiener process. The increment of the Wiener process  $dW(t)$  is an independent Gaussian random variable with mean equal 0 and variance equal  $dt$ , i.e.  $\langle dW(t) \rangle \equiv 0$  and  $\langle dW(t)^2 \rangle \equiv dt$ . The stochastic process, here  $W(t)$ , is non-continuous in time and therefore not differentiable. Strictly speaking, Eq. (A.1) is only valid in an integral form. For the integration of the non-continuous stochastic term, standard rules of calculus do not apply and instead we consider here the rules of Itô. The integral form of Eq. (A.1) reads

$$\int_{t_0}^{t_1} dU(t) = -a' \int_{t_0}^{t_1} U(t) dt + b \int_{t_0}^{t_1} dW(t), \quad (\text{A.2})$$

where we assume linear drift and constant diffusion coefficients,  $a = a'U$  and  $b$ , respectively, during a small time interval  $\Delta t = t_1 - t_0$ . For the general case  $a$  and  $b$  are estimated at  $t_0$  and assumed to remain constant during the time interval  $\Delta t$ . Eq. (A.2) is multiplied with  $e^{a't}$  to obtain

$$\int_{t_0}^{t_1} e^{a't} dU(t) = -a' \int_{t_0}^{t_1} U(t) e^{a't} dt + b \int_{t_0}^{t_1} e^{a't} dW(t). \quad (\text{A.3})$$

Now, a new stochastic process

$$G(t) = e^{a't} U(t) \quad (\text{A.4})$$

is defined, which is again an Itô process. The Itô formula is a sort of chain rule for Itô integrals or processes. With this formula and the following scaling laws of Itô calculus

- $dt^2 \rightarrow 0$
- $dt dW(t) \rightarrow 0$
- $dW(t)^2 = \mathcal{O}(dt)$ ,

the evolution of  $G$  is governed by

$$dG = \frac{\partial G}{\partial t} dt + \frac{\partial G}{\partial U} dU + \frac{1}{2} \frac{\partial^2 G}{\partial U^2} dU^2. \quad (\text{A.5})$$

After inserting the definition of  $G$  (Eq. (A.4)) into Eq. (A.5) we obtain

$$dG = d\left(e^{a't}U\right) = a'e^{a't}U dt + e^{a't}dU. \quad (\text{A.6})$$

Eqs. (A.3) and (A.6) are combined and manipulated, such that it results in the solution for the stochastic process  $U(t)$

$$U(t_1) = U(t_0)e^{-a'(t_1-t_0)} + \int_{t_0}^{t_1} be^{a'(t_1-t)}dW(t). \quad (\text{A.7})$$

A key point in the Itô calculus and at the same time also the major difference to the ordinary calculus is that

$$\int_0^t W(s)dW(s) = \frac{1}{2} (W(t)^2 - W(0)^2 - t). \quad (\text{A.8})$$

This difference originates as mentioned above from the scaling  $dW(t)^2 = \mathcal{O}(dt)$  and therefore terms in  $dW(t)^2$  must be retained in e.g. a first order Taylor series expansion.

## B Local Particle Time Stepping Algorithm

In general, the numerical solution algorithm for the PDF transport equation is based on particle Monte Carlo methods (see also secs. 3 and 4.3 in this thesis). Usually the particle time step is universal for all particles in the computational domain and is calculated based on a Courant-Friedrich-Lewy (CFL) condition for the worst particle (meaning the particle with the largest ratio of particle velocity and cell size, i.e.  $|\mathbf{U}^*|/L_{cell}$ ). This leads to the situation that fast particles in small cells travel in very few time steps through a cell and slow particles in large cells remain in the same cell for a long time. This behavior results in an uneven distributed level of statistical accuracy.

If the particles reside in a cell for many time steps, then the ensemble renewal rate is very low and the extracted statistics becomes poor. Note that this is mainly the case if statistically stationary solutions are considered, where a time averaging technique is applied to reduce the statistical and bias errors (see moving time averaging by Jenny et al. [36]).

Another problem arises in the pseudo transient state of the simulation, which concerns the particle distribution. The internal consistency requirements of a hybrid finite volume/particle algorithm (see section 4.3.1, last paragraph) demand that the weighted cloud in cell particle number density matches the mean finite volume fluid density. On the algorithmic level, this is enforced by a correction scheme, which adjusts the particle positions such that the particle number density becomes consistent with the fluid density. However, during the initial phase of the calculation, starting with possibly unphysical initial conditions, it is extremely difficult to fulfill this consistency requirement, which influences the convergence behavior of the algorithm.

Both of the issues described above can be improved by a local particle time stepping scheme, where each particle is evolved with an individual time step size. Such a scheme was developed by Muradoglu and Pope [50]. Here we give an overview of the scheme and we additionally present some practical implementation details. It is important to note that this asynchronous time stepping scheme is only applicable for statistical steady state simulations.

If we denote global and individual particle time steps as  $\Delta t$  and  $\Delta t^*$ , respectively, the particle property

$$\eta^* = \frac{\Delta t^*}{\Delta t}, \tag{B.1}$$

can be defined. It can be understood as a dimensionless time step and is calculated via the above equation. In practice, we define a smooth  $\eta$ -field denoted by  $\eta(\mathbf{x}, t)$ . In the discrete case  $\eta$  is determined at each grid node  $(i, j)$ . First, the local time step sizes at each grid point are computed by the following three CFL conditions

$$\Delta t_{i,j}^x = \frac{C_u \Delta x_{i,j}}{|U|_{i,j}}, \quad (\text{B.2})$$

$$\Delta t_{i,j}^y = \frac{C_u \Delta y_{i,j}}{|V|_{i,j}}, \quad \text{and} \quad (\text{B.3})$$

$$\Delta t_{i,j}^\omega = \frac{C_\omega}{\Omega_{i,j}}. \quad (\text{B.4})$$

Here,  $x_{i,j}$  and  $y_{i,j}$  are the grid dimensions in  $x$ - and  $y$ -direction and are evaluated as

$$\Delta x_{i,j} = 0.5(x_{i+1,j} - x_{i-1,j}) \quad \text{and} \quad \Delta y_{i,j} = 0.5(y_{i,j+1} - y_{i,j-1}). \quad (\text{B.5})$$

The coefficients  $C_u$  and  $C_\omega$  are CFL numbers in physical and frequency space, respectively, and are chosen as  $C_u = 0.5$  and  $C_\omega = 0.2$ . Further,  $\Omega_{i,j}$  is the mean conditional turbulence frequency (see Eq. (4.36), on page 26) and  $|U|_{i,j}$  and  $|V|_{i,j}$  are representative absolute particle velocities in the two spacial directions, which are specified by the mean fluid velocity and an extracted fluctuating velocity measure, i.e.

$$|U|_{i,j} = |\tilde{U}_{i,j}| + 2(\widetilde{uu})_{i,j}^{1/2} \quad \text{and} \quad (\text{B.6})$$

$$|V|_{i,j} = |\tilde{V}_{i,j}| + 2(\widetilde{vv})_{i,j}^{1/2}. \quad (\text{B.7})$$

Then the local particle time step  $\Delta t_{i,j}$  at a grid node is determined as follows

$$\Delta t_{i,j} = \min[\Delta t_{i,j}^x, \Delta t_{i,j}^y, \Delta t_{i,j}^\omega], \quad (\text{B.8})$$

and the  $\eta$ -field can be calculated as

$$\eta_{i,j} = \frac{\Delta t}{\min_{\forall i,j}(\Delta t_{i,j})}, \quad (\text{B.9})$$

where the denominator specifies the global time step  $\Delta t$ . Note that the choice of the global time step is somewhat arbitrary, here, it is taken as the smallest occurring time step. Moreover, an upper limit  $\eta_{\max}$  is defined and the whole field is linearly scaled

$$\eta_{i,j} = \left( \frac{\max_{\forall i,j}(\eta_{i,j}) - 1}{\eta_{\max} - 1} \right) (\eta_{i,j} - 1) + 1, \quad (\text{B.10})$$

such that all  $\eta$ -values lie in the interval  $[1, \eta_{\max}]$ . Finally, one obtains the local dimensionless particle time step  $\eta^*$  by linear interpolation of the node values  $\eta_{i,j}$  to the particle position  $\mathbf{x}^*$ . This value is then stored as a particle property.

As soon as statistical quantities are extracted from the particle ensemble the local time step has to be taken into account. The statistical weight of a particle is modified by a

factor, which corresponds to the value of  $\eta^*$ . As a consequence, to extract the mean of an arbitrary particle quantity  $q^*$  at grid node  $(i, j)$ , the scheme

$$\tilde{q}_{i,j} = \frac{\sum_{k=1}^{N_p} \hat{g}_{i,j}(\mathbf{x}^{(k)}) m^{(k)} \eta^{(k)} q^{(k)}}{\sum_{k=1}^{N_p} \hat{g}_{i,j}(\mathbf{x}^{(k)}) m^{(k)} \eta^{(k)}} \quad (\text{B.11})$$

must be applied, where  $N_p$  is the number of particles in the ensemble,  $m^{(k)}$  the mass (original weight) of particle  $k$  and  $\hat{g}_{i,j}(\mathbf{x})$  a kernel function around node  $(i, j)$ . Note that for  $\eta^* = 1$  expression (B.11) is identical to the one used to extract stochastic moments in a synchronous particle time stepping scheme.

More care is required for a conservative formulation of the IEM mixing model, where

$$\frac{d\phi_\alpha^*}{dt} = -\frac{C_\phi}{2} \Omega \left( \phi_\alpha^* - \tilde{\phi}_\alpha^{\text{IEM}} \right) \quad (\text{B.12})$$

describes the evolution of a scalar  $\phi_\alpha^*$  due to molecular mixing. In the discrete case and with the local particle time step considered, the change of the particle scalar value is

$$\Delta\phi_\alpha^* = -\frac{C_\phi}{2} \Omega \eta^* \Delta t \left( \phi_\alpha^* - \tilde{\phi}_\alpha^{\text{IEM}} \right). \quad (\text{B.13})$$

For conservation reasons the mean change in one grid cell has to be zero, therefore it is required that

$$\widetilde{\Delta\phi_\alpha^*} = \frac{\sum_{k=1}^{N_p} \hat{g}(\mathbf{x}^{(k)}) m^{(k)} \eta^{(k)} \Delta\phi_\alpha^{(k)}}{\sum_{k=1}^{N_p} \hat{g}(\mathbf{x}^{(k)}) m^{(k)} \eta^{(k)}} \stackrel{!}{=} 0. \quad (\text{B.14})$$

Substituting Eq. (B.13) and setting  $\hat{g}(\mathbf{x}) = 1$  (cell averaged extraction), we can solve Eq. (B.14) for the drift target to obtain

$$\tilde{\phi}_\alpha^{\text{IEM}} = \frac{\sum_{k=1}^{N_p} m^{(k)} \eta^{(k)} \eta^{(k)} \phi_\alpha^{(k)}}{\sum_{k=1}^{N_p} m^{(k)} \eta^{(k)} \eta^{(k)}}. \quad (\text{B.15})$$

Note that the dimensionless particle time step  $\eta^*$  enters quadratically into the above relation.

Further analysis of the local time stepping scheme, particularly the prove that the scheme converges to the correct steady state solution, can be found in the original paper by Muradoglu and Pope [50] and in appendix A of Merci et al. [44].



## References

- [1] R. Abdel-Gayed, D. Bradley & F.-K. Lung. “Combustion regimes and the straining of turbulent premixed flames”. *Combustion and Flame*, **76**(2) [1989]: pp. 213 – 218.
- [2] M. S. Anand & S. B. Pope. “Calculations of premixed turbulent flames by PDF methods”. *Combustion and Flame*, **67**(2) [1987]: pp. 127 – 142.
- [3] R. Barlow. “<http://www.ca.sandia.gov/TNF>”. TNF Workshop; Sandia National Laboratories.
- [4] R. Bilger. “The structure of turbulent nonpremixed flames.” *Twenty-Second Symposium on Combustion* [1988]: pp. 475–488.
- [5] R. W. Bilger. “Turbulent flows with nonpremixed reactants”. P. A. Libby & F. A. Williams (Eds.) “Turbulent Reacting Flows”, Springer Verlag, Berlin / Heidelberg [1980], pp. 65 – 113.
- [6] R. Borghi. “On the structure and morphology of turbulent premixed flames”. *Recent Advances in Aerospace Sciences* [1985]: pp. 117 – 138. Plenum, New York.
- [7] D. Bradley, P. Gaskell & X. Gu. “Application of a reynolds stress, stretched flamelet, mathematical model to computations of turbulent burning velocities and comparison with experiments”. *Combustion and Flame*, **96**(3) [1994]: pp. 221 – 248.
- [8] D. Bradley, P. Gaskell & X. Gu. “The mathematical modeling of liftoff and blowoff of turbulent non-premixed methane jet flames at high strain rates”. *Symposium (International) on Combustion*, **27**(1) [1998]: pp. 1199 – 1206. Twenty-Seventh Symposium (International) on Combustion Volume One.
- [9] D. Bradley, P. Gaskell & X. Gu. “The modeling of aerodynamic strain rate and flame curvature effects in premixed turbulent combustion”. *Symposium (International) on Combustion*, **27**(1) [1998]: pp. 849 – 856. Twenty-Seventh Symposium (International) on Combustion Volume One.
- [10] D. Bradley, P. Gaskell & A. Lau. “A mixedness-reactedness flamelet model for turbulent diffusion flames”. *Symposium (International) on Combustion*, **23**(1) [1991]: pp. 685 – 692. Twenty-Third Symposium (International) on Combustion.
- [11] K. Bray, P. A. Libby & J. Moss. “Unified modeling approach for premixed turbulent combustion—Part I: General formulation.” *Combustion and Flame*, **61**(1) [1985]: pp. 87 – 102.
- [12] K. N. C. Bray & P. A. Libby. “Passage Times and Flamelet Crossing Frequencies in Premixed Turbulent Combustion”. *Combustion Science and Technology*, **47**(5 & 6) [1986]: pp. 253 – 274.
- [13] K. N. C. Bray & J. B. Moss. “A unified statistical model of the premixed turbulent flame.” *Acta Astronautica*, **4**(3-4) [1977]: pp. 291 – 319.

- [14] S. P. Burke & T. E. W. Schumann. “Diffusion flames”. *First Symposium (International) on Combustion* [1928]: pp. 2 – 11.
- [15] G. C. Chang. *A Monte Carlo PDF/finite volume study of turbulent flames*. Ph.D. thesis, Cornell University [1996].
- [16] M. Chen, M. Herrmann & N. Peters. “Flamelet modeling of lifted turbulent methane/air and propane/air jet diffusion flames”. *Proceedings of the Combustion Institute*, **28**(1) [2000]: pp. 167 – 174.
- [17] M. K. Chung & S. K. Kim. “A nonlinear return-to-isotropy model with Reynolds number and anisotropy dependency”. *Physics of Fluids*, **7**(6) [1995]: pp. 1425–1436.
- [18] S. Correa & S. Pope. “Comparison of a monte carlo pdf/finite-volume mean flow model with bluff-body raman data”. *Symposium (International) on Combustion*, **24**(1) [1992]: pp. 279 – 285. Twenty-Fourth Symposium on Combustion.
- [19] R. L. Curl. “Dispersed phase mixing: I. Theory and effects in simple reactors”. *AIChE Journal*, **9**(2) [1963]: pp. 175 – 181.
- [20] B. J. Delarue & S. B. Pope. “Application of PDF methods to compressible turbulent flows”. *Physics of Fluids*, **9**(9) [SEP 1997]: pp. 2704–2715.
- [21] P. Domingo & L. Vervisch. “Triple flames and partially premixed combustion in autoignition of non-premixed turbulent mixtures”. *Symposium (International) on Combustion*, **26**(1) [1996]: pp. 233 – 240.
- [22] P. Domingo, L. Vervisch & K. Bray. “Partially premixed flamelets in LES of non-premixed turbulent combustion”. *Combustion Theory and Modelling*, **6**(4) [2002]: pp. 529 – 551.
- [23] P. Domingo, L. Vervisch & J. Rveillon. “DNS analysis of partially premixed combustion in spray and gaseous turbulent flame-bases stabilized in hot air”. *Combustion and Flame*, **140**(3) [2005]: pp. 172 – 195.
- [24] T. D. Dreeben & S. B. Pope. “Probability density function/Monte Carlo simulation of near-wall turbulent flows”. *Journal of Fluid Mechanics*, **357** [1998]: pp. 141–166.
- [25] T. Echekki & J. H. Chen. “Structure and Propagation of Methanol-Air Triple Flames”. *Combustion and Flame*, **114**(1-2) [1998]: pp. 231 – 245.
- [26] A. Einstein & R. Fürth. *On the Movement of Small Particles Suspended in a Stationary Liquid Demanded by the Molecular-Kinetic Theory of Heat*. Dover Publications [1926 (reprinted 1956)].
- [27] R. O. Fox. *Computational Models for Turbulent Reacting Flows*. Cambridge University Press [2003].
- [28] T. C. Gard. *Introduction to Stochastic Differential Equations*. Dekker [1988].



- [29] C. W. Gardiner. *Handbook of Stochastic Methods*. Springer Verlag, 3rd ed. [2004].
- [30] D. Haworth. “Progress in probability density function methods for turbulent reacting flows”. *Progress in Energy and Combustion Science*, **36**(2) [2010]: pp. 168 – 259.
- [31] D. C. Haworth & S. B. Pope. “A generalized Langevin model for turbulent flows”. *Physics of Fluids*, **29**(2) [1986]: pp. 387–405.
- [32] S. Heinz. *Statistical Mechanics of turbulent flows*. Springer, Berlin, 1st ed. [2003].
- [33] M. Ihme & H. Pitsch. “Prediction of extinction and reignition in nonpremixed turbulent flames using a flamelet/progress variable model: 1. A priori study and presumed PDF closure”. *Combustion and Flame*, **155**(1-2) [2008]: pp. 70 – 89.
- [34] K. Itô & H. McKean. *Diffusion Processes and Their Sample Paths*. Springer Verlag [1965].
- [35] Jayesh & S. Pope. “Stochastic Model for Turbulent Frequency”. *FDA* [1995].
- [36] P. Jenny, S. B. Pope, M. Muradoglu & D. A. Caughey. “A Hybrid Algorithm for the Joint PDF Equation of Turbulent Reactive Flows”. *Journal of Computational Physics*, **166**(2) [2001]: pp. 218 – 252.
- [37] W. Jones & B. Launder. “The prediction of laminarization with a two-equation model of turbulence”. *Int. J. Heat Mass Transfer*, **15** [1972]: pp. 301–314.
- [38] A. Kronenburg & M. Cleary. “Multiple mapping conditioning for flames with partial premixing”. *Combustion and Flame*, **155**(1-2) [2008]: pp. 215 – 231.
- [39] V. R. Kuznetsov. “The effect of turbulence on the formation of large superequilibrium concentrations of atoms and free radicals in diffusion flames”. *Izvestiia, Mekhanika Zhidkosti i Gaza*, **6** [1982]: pp. 3 – 9. Akademiia Nauk SSSR.
- [40] B. E. Launder, G. J. Reece & W. Rodi. “Progress in the development of a Reynolds-stress turbulence closure”. *Journal of Fluid Mechanics Digital Archive*, **68**(03) [1975]: pp. 537–566.
- [41] R. J. LeVeque. *Numerical Methods for Conservation Laws*. Birkhäuser, second ed. [1992].
- [42] S. K. Liew, K. N. Bray & J. B. Moss. “A Flamelet Model of Turbulent Non-Premixed Combustion”. *Combustion Science and Technology*, **27**(1 & 2) [1981]: pp. 69 – 73.
- [43] J. L. Lumley & G. R. Newman. “The return to isotropy of homogeneous turbulence”. *Journal of Fluid Mechanics Digital Archive*, **82**(01) [1977]: pp. 161–178.
- [44] B. Merci, D. Roekaerts & B. Naud. “Study of the performance of three micromixing models in transported scalar PDF simulations of a piloted jet diffusion flame (‘Delft Flame III’)”. *Combustion and Flame*, **144**(3) [2006]: pp. 476 – 493.

- [45] D. W. Meyer & P. Jenny. “An improved mixing model providing joint statistics of scalar and scalar dissipation”. *Combustion and Flame*, **155**(3) [2008]: pp. 490 – 508.
- [46] D. W. Meyer & P. Jenny. “Micromixing models for turbulent flows.” *Journal of Computational Physics*, **228**(4) [2009]: pp. 1275 – 1293.
- [47] J.-P. Minier, E. Peirano & S. Chibbaro. “Weak first- and second-order numerical schemes for stochastic differential equations appearing in Lagrangian two-phase flow modeling”. *Monte Carlo Methods and Applications*, **9**(2) [2003]: pp. 93 – 133.
- [48] C. M. Mueller, H. Breitbach & N. Peters. “Partially premixed turbulent flame propagation in jet flames”. *Symposium (International) on Combustion*, **25**(1) [1994]: pp. 1099 – 1106. Twenty-Fifth Symposium (International) on Combustion.
- [49] M. Muradoglu, K. Liu & S. B. Pope. “PDF modeling of a bluff-body stabilized turbulent flame”. *Combustion and Flame*, **132**(1-2) [2003]: pp. 115 – 137.
- [50] M. Muradoglu & S. B. Pope. “Local Time-Stepping Algorithm for Solving Probability Density Function Turbulence Model Equations”. *AIAA Journal*, **40** [2002]: pp. 1755–1763.
- [51] M. Muradoglu, S. B. Pope & D. A. Caughey. “The Hybrid Method for the PDF Equations of Turbulent Reactive Flows: Consistency Conditions and Correction Algorithms”. *Journal of Computational Physics*, **172**(2) [2001]: pp. 841 – 878.
- [52] P. A. Nooren, H. A. Wouters, T. W. Peeters, D. Roekaerts, U. Maas & D. Schmidt. “Monte Carlo PDF modelling of a turbulent natural-gas diffusion flame”. *Combustion Theory and Modelling*, **1** [1997]: pp. 79 – 96.
- [53] B. Oksendal. *Stochastic Differential Equations: An Introduction with Applications (Universitext)*. Springer Verlag [December 2005].
- [54] S. Osher & J. A. Sethian. “Fronts propagating with curvature-dependent speed: Algorithms based on Hamilton-Jacobi formulations”. *Journal of Computational Physics*, **79**(1) [1988]: pp. 12 – 49.
- [55] N. Peters. “Local quenching of diffusion flamelets and non-premixed turbulent combustion”. *Western States Section of the Combustion Institute* [1980]. Paper WSS 80-4, Spring Meeting, Irvine, CA.
- [56] N. Peters. “Laminar diffusion flamelet models in non-premixed turbulent combustion”. *Progress in Energy and Combustion Science*, **10**(3) [1984]: pp. 319 – 339.
- [57] N. Peters. “Laminar flamelet concepts in turbulent combustion”. *Symposium (International) on Combustion*, **21**(1) [1988]: pp. 1231 – 1250. Twenty-First Symposium (International) on Combustion).
- [58] N. Peters. *Turbulent Combustion*. Cambridge University Press [2000].

- [59] C. D. Pierce & P. Moin. “Progress-variable approach for large-eddy simulation of non-premixed turbulent combustion”. *Journal of Fluid Mechanics*, **504** [2004]: pp. 73–97.
- [60] T. Poinsot & D. Veynante. *Theoretical and numerical combustion*. Edwards, Philadelphia, USA [2005].
- [61] T. Poinsot, D. Veynante & S. Candel. “Diagrams of premixed turbulent combustion based on direct simulation”. *Symposium (International) on Combustion*, **23**(1) [1991]: pp. 613 – 619. Twenty-Third Symposium (International) on Combustion.
- [62] S. B. Pope. “A Monte Carlo Method for the PDF Equations of Turbulent Reactive Flow”. *Combustion Science and Technology*, **25**(5&6) [1981]: pp. 159 – 174.
- [63] S. B. Pope. “PDF methods for turbulent reactive flows”. *Progress in Energy and Combustion Science*, **11**(2) [1985]: pp. 119 – 192.
- [64] S. B. Pope. “Mapping Closures for Turbulent Mixing and Reaction”. *Theoretical and Computational Fluid Dynamics*, **2** [1991]: pp. 255 – 270.
- [65] S. B. Pope. “Particle Method for Turbulent Flows: Integration of Stochastic Model Equations”. *Journal of Computational Physics*, **117**(2) [1995]: pp. 332 – 349.
- [66] S. B. Pope. *Turbulent Flows*. Cambridge University Press, Cambridge, United Kingdom [2000].
- [67] V. Raman, R. O. Fox & A. D. Harvey. “Hybrid finite-volume/transported PDF simulations of a partially premixed methane-air flame”. *Combustion and Flame*, **136**(3) [2004]: pp. 327 – 350.
- [68] J. Rotta. “Statistische Theorie nichthomogener Turbulenz.” *Z. Phys.*, **129** [1951]: pp. 547–572.
- [69] J. Sanders & A. Lamers. “Modeling and calculation of turbulent lifted diffusion flames”. *Combustion and Flame*, **96**(1-2) [1994]: pp. 22 – 33.
- [70] S. Sarkar & C. G. Speziale. “A simple nonlinear model for the return to isotropy in turbulence”. *Physics of Fluids*, **A**(2) [1990]: pp. 84–93.
- [71] V. Saxena & S. B. Pope. “PDF simulations of turbulent combustion incorporating detailed chemistry”. *Combustion and Flame*, **117**(1-2) [1999]: pp. 340 – 350.
- [72] R. Stratonovich. “A new representation for stochastic integrals and equations.” *J. Siam Control*, **4** [1966]: pp. 362–371.
- [73] S. Subramaniam & S. B. Pope. “A mixing model for turbulent reactive flows based on Euclidean minimum spanning trees”. *Combustion and Flame*, **115**(4) [1998]: pp. 487 – 514.

- [74] P. R. van Slooten & S. B. Pope. “Application of PDF Modeling to Swirling and Nonswirling Turbulent Jets”. *Flow, Turbulence and Combustion*, **62** [1999]: pp. 295 – 333.
- [75] L. Vervisch & P. Domingo. “Two recent developments in numerical simulation of premixed and partially premixed turbulent flames”. *Comptes Rendus Mecanique*, **334**(8-9) [2006]: pp. 523 – 530. Observation, analysis and modelling in complex fluid media - Special issue for the 60th birthday of Professor Roland Borghi.
- [76] J. Villiermaux & J. Devillon. “Representation de la coalescence et de la redispersion des domaines de segregation dans un fluide par un modele d’interaction phenomenologique”. “Second International Symposium on Chemical Reaction Engineering”, Elsevier, New York [1972], pp. 1–13.
- [77] J. Warnatz, U. Maas & R. W. Dibble. *Combustion*. Springer Verlag, Berlin, Heidelberg, New York, 3rd ed. [2001].
- [78] D. Wilcox. “Turbulence modeling for CFD” [1993].
- [79] F. A. Williams. “Recent advances in theoretical descriptions of turbulent diffusion flames”. S. N. B. Murphy (Ed.) “Turbulent mixing in nonreactive and reactive flows”, Plenum Press, New York [1975], pp. 189 – 208.
- [80] F. A. Williams. “Turbulent Combustion”. J. Buckmaster (Ed.) “The Mathematics of Combustion”, SIAM, Philadelphia [1985], pp. 97 – 131.
- [81] J. Xu & S. B. Pope. “Assessment of Numerical Accuracy of PDF/Monte Carlo Methods for Turbulent Reacting Flows”. *Journal of Computational Physics*, **152**(1) [1999]: pp. 192 – 230.

# CURRICULUM VITAE

## Personal details

Family name	Hegetschweiler
First Names	Michael Jakob
Citizen of	Ottenbach (ZH), Switzerland
Date of birth	25.05.1974
Place of birth	Sursee (LU)

## Education

2004 - present	Ph.D. student at the Institute of Fluid Dynamics, ETH Zurich, Switzerland
1994 - 2001	Diploma (M.Sc.) studies in mechanical engineering at ETH Zurich, Switzerland Major in power plant & nuclear engineering and lightweight construction. Diploma thesis title (in German): <i>"Optimierung Der Natürlichen Konvektion im Kühlkreislauf eines ESBWR"</i> .
1987 - 1994	State high school (Gymnasium, Typus C) at Kantonsschule Sursee (LU)
1981 - 1987	Primary school in Oberkirch (LU)

## Employment

2004 - present	Research and teaching assistant at the Institute of Fluid Dynamics, ETH Zurich, Switzerland
2001 - 2004	Gas turbine engineer (customer service) at ALSTOM AG, Baden, Switzerland
1997	Internship at Sulzer Turbo AG (now: MAN Turbo) in the department aerodynamic development.

# PUBLICATION LIST

## Reviewed Journal Papers

- [1] M. Hegetschweiler, C. Handwerk & P. Jenny. “Partially Premixed Turbulent Combustion Model Based on Joint Statistics of Progress Variable, Mixture Fraction, and Scalar Dissipation Rate”. *Combustion Science and Technology*, **182**(4) [2010]: pp. 480 – 490.
- [2] M. Hegetschweiler, B. Zoller & P. Jenny. “Reactive PSP Mixing Model for Partially Premixed Combustion” [2010]. Submitted/in revision ”Combustion and Flame”.

## Reviewed Conference Papers

- [3] M. Hegetschweiler & P. Jenny. “Time Accurate Numerical Integration Scheme for Stochastic Differential Equations with respect to Joint Statistics.” *Proceedings of the European Combustion Meeting, Vienna* [2009].
- [4] M. Hegetschweiler & P. Jenny. “Extended Flamelet Model and Improved Interaction of Chemistry and Turbulence for Modeling Partially Premixed Combustion with a Joint PDF Method”. *PAMM (GAMM Proceedings)*, **7**(1) [2007]: pp. 4090019–4090020.
- [5] M. Hegetschweiler & P. Jenny. “An Approach to Model Partially Premixed Turbulent Combustion with PDF Methods”. *PAMM (GAMM Proceedings)*, **6**(1) [2006]: pp. 521–522.

## Conference Talks

- [6] M. J. Hegetschweiler, C. Handwerk & P. Jenny. “Modeling of Partially Premixed Flames Using a Scale Separation Approach” [2009]. Conference Talk, Sixth Mediterranean Combustion Symposium, Corsica.
- [7] M. J. Hegetschweiler & P. Jenny. “An Approach to Model Partially Premixed Turbulent Combustion with Probability Density Function (PDF) Methods” [2007]. Conference talk, GAMM, Zurich.
- [8] M. Hegetschweiler & P. Jenny. “An Approach to Model Partially Premixed Turbulent Combustion with Probability Density Function Methods” [2006]. Conference talk, GAMM, Berlin.